

ABSTRACT

Title of Dissertation: ENHANCEMENT OF SPRAY COOLING
HEAT TRANSFER USING EXTENDED
SURFACES AND NANOFUIDS

Johnathan Stuart Coursey, Ph.D., 2007

Directed By: Associate Professor, Jungho Kim, Department of
Mechanical Engineering

Spray cooling is a powerful heat transfer technique in which an atomizing nozzle provides a flow of liquid droplets directed towards a hot surface. This dissertation explores two potentially powerful techniques capable of improving traditional spray cooling: nanofluids and extended surfaces.

Nanofluids were experimentally studied in a pool boiling system to elucidate the underlying mechanisms of critical heat flux (CHF) enhancement. Dilute suspensions of nanoparticles were found to have a degrading or no effect on boiling performance. Greater concentrations (≥ 0.5 g/L) lead to modest (up to $\sim 37\%$) increase in the CHF. The results were highly dependent on the working fluid/substrate combination, specifically wetting characteristics. Poorly wetting systems (e.g. water on copper) could be enhanced by nanofluids, whereas better wetting systems (e.g. ethanol on glass) showed no improvement. This conclusion was re-enforced when nanofouling caused by dryout of nanofluid was found to improve wetting as shown by a reduction in the advancing three-

phase contact angle. Interestingly, similar CHF enhancement was achieved without nanofluids using an oxidized surface, which is easily wetted with pure fluids. In fact, surface treatment alone resulted in similar CHF enhancement at $\sim 20^{\circ}\text{C}$ less wall superheat than required using nanofluids. Spray cooling was found to be adversely affected by the addition of nanoparticles due to changing thermophysical properties and/or nozzle clogging due to particle deposition.

The addition of high aspect ratio open microchannels to the sprayed surface resulted in significant enhancement at all wall superheats and over 200% enhancement in the low temperature single-phase regime. The two-phase regime began at lower temperatures with microchannels, which lead to heat transfer enhancements of up to 181%. The onset of two-phase effects was found to be a strong function of channel depth. However, the onset of two-phase effects was found to occur at a temperature that was independent of nozzle pressure/mass flow rate. Therefore, nucleation and two-phase effects are likely triggered by the unique liquid distribution caused by the extended structures. Using high aspect ratio open microchannels, these mechanisms resulted in spray efficiencies approaching one, indicating almost complete utilization of the spray's ability to absorb heat.

ENHANCEMENT OF SPRAY COOLING HEAT TRANSFER USING
EXTENDED SURFACES AND NANOFUIDS

By

Johnathan Stuart Coursey

Dissertation submitted to the Faculty of the Graduate School of the
University of Maryland, College Park, in partial fulfillment
of the requirements for the degree of
Doctor of Philosophy
2007

Advisory Committee:
Professor Jung-ho Kim, Chair
Professor Avram Bar-Cohen
Professor Kenneth Kiger
Professor James Quintiere
Professor Reinhard Radermacher

© Copyright by
Johnathan Stuart Coursey
2007

To my wife, Derya

ACKNOWLEDGEMENTS

First and foremost, I would like to acknowledge the guidance and support of my advisor, Dr. Jungho Kim. Without his valuable suggestions throughout, this dissertation would not have been possible. Furthermore, without the valuable experience I gained during my M.S. under Dr. Kim, I would likely have not considered returning to school to complete my Ph.D. I also appreciate the advice and guidance of my dissertation committee members: Dr. Avram Bar-Cohen, Dr. Kenneth Kiger, Dr. James Quintiere, and Dr. Reinhard Radermacher. In particular, I appreciate the guidance and assistance of Dr. Kiger, who has helped me for many years from undergraduate fluid mechanics and on to the present dissertation.

I have been very fortunate to work side by side with a number of distinguished current and former students (Chris Henry, Eric Silk, Greg Anderson, Payam Delgoshaei, Rishi Raj, Thierry Some, Kevin Moores, William Michie, Dennis Gordt, Eckhard Lehmann, Alexander Walzenbach, and Martin Karch) who are wonderful friends and invaluable colleagues. I owe a particular debt of gratitude to Chris and Greg for countless, and often spirited, discussions about heat transfer phenomena. Similarly, I am also indebted to Dr. Hitoshi Sakamoto, who is also a great friend and former colleague. His suggestions and daily consultation were dearly appreciated.

This dissertation also significantly benefited from the assistance of many people across the greater university community: Jack Touart (Physics); Lisa Lucas, Scott Horst, and Dan Hinkel (Laboratory of Physical Sciences); Al Aaron (ENME), and Howie Grossenbacher (ENAE). These talented professionals aided in construction of a number of parts used in this work and taught my many lessons around the lab and machine shop.

I would also not ever have been in a position to complete this dissertation without the support of my family. My parents and brothers have motivated me, listened to me, and encouraged me throughout my life, and I continue to be forever grateful. Finally, this endeavor would not have been possible without the support and encouragement of my wife, Derya. I appreciate the many sacrifices she has made from waking up early to make me sandwiches to listening to my dissertation ideas late into the evening.

TABLE OF CONTENTS

CHAPTER 1. INTRODUCTION	1
1.1. Motivation	1
1.2. Background	2
1.3. Research Objectives	7
CHAPTER 2. LITERATURE REVIEW	9
2.1. Boiling Heat Transfer	9
2.1.1. Nucleate Boiling	9
2.1.2. Critical Heat Flux	12
2.1.3. Surface Wettability	13
2.2. Spray Cooling	14
2.2.1. Droplet Features	14
2.2.2. Parameters Affecting Spray Cooling	16
2.2.3. Models of Spray Cooling	19
2.2.4. Spray Cooling Correlations	22
2.3. Nanofluids	24
2.3.1. Thermal Conductivity Enhancement	24
2.3.2. Boiling of Nanofluids	28
2.4. Extended Structures	34
CHAPTER 3. EXPERIMENTAL SETUP AND METHODOLOGY	37
3.1. Nanofluids Boiling and Spray Cooling Setups	37
3.1.1. Nanofluids Test Rig	37
3.1.2. Thick-film Resistive Heater	39
3.1.3. Copper Block Heater	42
3.1.4. Working Fluids and Nanofluid Preparation	46
3.1.5. Test Conditions	48
3.2. Contact Angle Measurements	50
3.2.1. Contact Angle Measurement Algorithm	52
3.3. High Aspect Ratio Open Microchannel Spray Cooling Experiments	53
3.3.1. Test Rig	54
3.3.2. Heater Assembly	55
3.3.3. Working Fluid and Spray Characteristics	57
3.3.4. Data Acquisition and Control	60
CHAPTER 4. UNCERTAINTY AND DATA ANALYSIS	63
4.1. Thick-film Resistive Heater	63
4.2. Copper Block Heaters	66
4.2.1. Boiling Heater	68
4.2.2. High Aspect Ratio Open Microchannel Spray Cooling Heater	70
4.3. Contact Angle Measurements	72
CHAPTER 5. NANOFUID POOL BOILING & SPRAY COOLING	73
5.1. Boiling Ethanol Based Nanofluids	73

5.1.1. Glass Surface	73
5.1.2. Gold Surface	75
5.1.3. Copper Surface	76
5.2. Boiling Water Based Nanofluids	82
5.2.1. Concentration Effects	83
5.2.2. Surface Wettability Effects	87
5.3. Nanofluid's Contact Angle Modification	93
5.3.1. Advancing Droplets on Copper	93
5.3.2. Advancing Droplets on Copper Oxide	97
5.4. Spray Cooling with Nanofluids	98
5.4.1. Spray Cooling Curves	99
5.4.2. Scaling Analysis	101
5.5. Summary of Nanofluid Research	104
CHAPTER 6. EXTENDED STRUCTURE SPRAY COOLING	107
6.1. Results of Spray Cooling High Aspect Ratio Open Microchannels	107
6.1.1. Single-Phase Results	109
6.1.2. Two-Phase Results	112
6.1.3. Critical Heat Flux Results	114
6.2. Spray Efficiency Improvement	115
6.3. One-Dimensional Model for Single-Phase Heat Transfer	120
6.3.1. Model Development	120
6.3.2. Results and Implications	121
CHAPTER 7. CONTRIBUTIONS AND CONCLUSIONS	124
7.1. Conclusions	124
7.2. Contributions to the State of the Art	126
7.3. Suggestions for Future Work	128
APPENDIX A: SURFACE WETTABILITY AND CONTACT ANGLE DEFINITIONS	130
APPENDIX B: LIBRARY OF COMPUTER PROGRAMS	132
APPENDIX C: MONTE CARLO UNCERTAINTY CALCULATIONS	133
APPENDIX D: CALCULATION OF PF-5060 VAPOR SPECIFIC HEAT	136
APPENDIX E: NUMERICAL MODEL OF FIN HEAT TRANSFER	141
E.1. Model Development	142
E.2. Model Results	145
E.3. Conclusions and Implications	149
REFERENCES	151

LIST OF TABLES

Table 1. Nondimensional parameters in the correlations of Stephan and Abdelsalam (1980).	11
Table 2. Various definitions of mean diameter.	15
Table 3. Important parameters affecting spray cooling.	16
Table 4. Summary of nanofluid boiling studies.	33
Table 5. Oxidation parameters used to increase the surface energy.	45
Table 6. Thermal properties at saturation (P=101325 Pa) (* Incropera & DeWitt, 1996; ** 3M, 2000; † Dillion & Penoncello, 2003; ‡ Yaws, 1999).	47
Table 7. Channel aspect ratio and surface areas of test surfaces.	56
Table 8. Fluid flow rate incident on top surface of heat sinks.	60
Table 9. Test matrix in the order in which it was run.	87
Table 10. Temperatures required for dominant two-phase effects.	114
Table 11. List of data acquisition and analysis programs.	132
Table 12. Steps in specific heat calculation for C ₆ F ₁₄ .	137

LIST OF FIGURES

Fig. 1. Swirl atomizer schematic.	3
Fig. 2. Illustration of spray cooling into a continuous liquid film.	4
Fig. 3. Typical boiling curve and associated boiling regimes.	5
Fig. 4. Simplified illustration of nucleate boiling heat transfer mechanisms.	10
Fig. 5. Thermal conductivity enhancements for various nanofluids (based on Eastman et al., 1997).	26
Fig. 6. CHF enhancement for alumina/water nanofluids (based on Moreno et al., 2005).	30
Fig. 7. Test rig.	38
Fig. 8. Thick-film resistor assembly (Courtesy of Alexander Walzenbach).	39
Fig. 9. Data acquisition and control diagram for thick-film resistor heater.	41
Fig. 10. Wheatstone bridge circuit to prevent burnout of the thick-film resistor.	42
Fig. 11. Wheatstone bridge circuit schematic.	42
Fig. 12. Copper heating block and stainless steel sealing plate.	43
Fig. 13. Typical temperature history of the copper block during the oxidation process.	44
Fig. 14. Data acquisition and control diagram for copper block boiling heater.	46
Fig. 15. Alumina-in-ethanol nanofluid samples (from left to right: 200 proof ethanol, 0.005 g/L, 0.01 g/L, 0.05 g/L, 0.1 g/L, 0.5 g/L, and 30.84 wt.%).	48
Fig. 16. Experimental test matrix for nanofluid boiling studies.	49
Fig. 17. Infusion pump setup.	51
Fig. 18. Advancing water droplet on a copper surface.	51
Fig. 19. Results of edge detection on the image of an advancing water droplet.	53
Fig. 20. Curve fitting results (the two other points on the interface are on the other side of the droplet).	53

Fig. 21. Experimental setup for microchannel spray cooling.	54
Fig. 22. Heating block assembly (Courtesy of William Michie).	56
Fig. 23. Heater necks with 5 mm (left) and 1 mm (right) long fins.	57
Fig. 24. Illustration of overspray and incident flux increasing with fin length.	59
Fig. 25. Incident flow measurement system.	60
Fig. 26. Data acquisition and control diagram for microchannel spray cooling.	62
Fig. 27. Histogram of Monte Carlo results with input from an RTD measurement that corresponds to a nominal temperature prediction of 50 °C.	65
Fig. 28. Finite element model of a quarter section of thick-film heater.	66
Fig. 29. Typical temperature profiles in the neck of the copper heater block (data from 0.05 g/L alumina-in-water nanofluid boiling on well oxidized copper).	68
Fig. 30. Finite element model results for copper block with boiling at the top of the neck and free convection heat losses.	70
Fig. 31. Finite element model of a quarter section of the heater, silicone adhesive, and ceramic insulation showing the temperature distribution.	71
Fig. 32. Steady-state boiling curves for subcooled ($T_{sat} = 51.7\text{ °C}$, $T_{bulk} = 30.6\text{ °C}$) alumina/ethanol nanofluid over a range of concentrations on glass.	74
Fig. 33. Photographs of static droplets on a glass substrate (water on the left, ethanol on the right).	75
Fig. 34. Steady-state boiling curves for subcooled ($T_{sat} = 51.7\text{ °C}$, $T_{bulk} = 30.6\text{ °C}$) alumina/ethanol nanofluid on gold.	76
Fig. 35. Steady-state boiling curves for near saturated ($T_{sat} = 28.9\text{ °C}$, $T_{bulk} = 28.8\text{ °C}$) alumina/ethanol nanofluid on copper.	77
Fig. 36. Superheat required for a given heat flux for various alumina-in-ethanol nanofluids on copper.	79
Fig. 37. CHF enhancement as a function of nanoparticle concentration for near saturated ethanol suspensions on copper.	80

Fig. 38. Thermal conductivity enhancement of alumina nanofluids at room temperature.	81
Fig. 39. Steady-state boiling curves for near saturated ($T_{sat} = 29.8\text{ }^{\circ}\text{C}$, $T_{bulk} = 29.3\text{ }^{\circ}\text{C}$) alumina/water nanofluid on copper.	84
Fig. 40. CHF enhancement as a function of nanoparticle concentration for near saturated water suspensions on copper.	84
Fig. 41. Surface tension of water/ethylene glycol mixtures at $20\text{ }^{\circ}\text{C}$ (after Horibe et al., 1996).	86
Fig. 42. Photographs of the advancing contact angle on polished copper (left) and copper oxide (right).	88
Fig. 43. Steady-state boiling curves ($T_{sat} = 29.8\text{ }^{\circ}\text{C}$, $T_{bulk} = 29.3\text{ }^{\circ}\text{C}$) illustrating the effect of surface oxidation.	90
Fig. 44. CHF as a function of advancing contact angle for pure water on copper and copper oxide.	90
Fig. 45. Boiling curves ($T_{sat} = 29.8\text{ }^{\circ}\text{C}$, $T_{bulk} = 29.3\text{ }^{\circ}\text{C}$) illustrating the CHF degradation caused by the addition of nanofluid.	92
Fig. 46. Comparison of nanofluid and oxidation enhancement techniques.	93
Fig. 47. Advancing contact angle of 1.02 g/L alumina-in-water nanofluid on copper.	95
Fig. 48. Second trial for advancing contact angle of 1.02 g/L alumina-in-water nanofluid on copper.	96
Fig. 49. Bubble growth leaving nanoparticles on the surface (left) and bubble detachment when liquid advances to cover the nanofouled dry patch (right).	97
Fig. 50. Advancing contact angle of 1.02 g/L alumina-in-water nanofluid on copper oxide.	98
Fig. 51. Spray cooling curves for subcooled ($T_{sat} = 51.7\text{ }^{\circ}\text{C}$, $T_{spray} = 30.5\text{ }^{\circ}\text{C}$) ethanol sprays ($\Delta P=69\text{ kPa}$) at various alumina nanoparticle concentrations.	99
Fig. 52. Spray cooling curves for subcooled ($T_{sat} = 51.7\text{ }^{\circ}\text{C}$, $T_{spray} = 30.5\text{ }^{\circ}\text{C}$) ethanol sprays ($\Delta P=345\text{ kPa}$) at various alumina nanoparticle concentrations.	101
Fig. 53. Relative viscosity increase for alumina nanofluids with linear fit that excludes the Pak & Cho data. [†] These authors report viscosity varying as a function	

of shear rate. Their results at the highest shear rates were used. Note that the viscosity increases are greater at lower shear rates.	102
Fig. 54. Relative heat transfer coefficient for jet impingement determined through scaling analysis as a function of nanoparticle volume fraction.	104
Fig. 55. Spray cooling curves for open microchannel surfaces at nozzle pressure of 138 kPa (20 psig).	108
Fig. 56. Spray cooling curves for open microchannel surfaces at nozzle pressure of 276 kPa (40 psig).	108
Fig. 57. Spray cooling curves for open microchannel surfaces at nozzle pressure of 413 kPa (60 psig).	109
Fig. 58. Heat flux as a function of nozzle pressure difference for $T_{wall} = 60^{\circ}\text{C}$ (similar results are obtained at other wall temperatures). Heat fluxes are based on the 2 cm ² projected area.	111
Fig. 59. Area and heat flux enhancement as a function of fin length for $T_{wall} = 60^{\circ}\text{C}$ (similar results are obtained at other wall temperatures). Heat fluxes are based on the 2 cm ² projected area.	112
Fig. 60. Spray efficiency as a function of fin length in the “single-phase” regime.	116
Fig. 61. Spray efficiency as a function of wall temperature for 138 kPa (20 psig) nozzle pressure difference.	118
Fig. 62. Spray efficiency as a function of wall temperature for 276 kPa (40 psig) nozzle pressure difference.	118
Fig. 63. Spray efficiency as a function of wall temperature for 413 kPa (60 psig) nozzle pressure difference.	119
Fig. 64. One-dimensional model results as a function of fin length for $T_{wall} = 60^{\circ}\text{C}$, $\Delta P = 4.08$ atm (60 psig) normalized by $h_{flat} = 9784$ W/(m ² ·K).	122
Fig. 65. Predicted temperature profile on 5 mm fins using 1-D model for $T_{wall} = 60^{\circ}\text{C}$, $\Delta P = 4.08$ atm (60 psig).	123
Fig. 66. Nonwetting (left) and wetting (right) liquid droplets.	130
Fig. 67. Schematic of advancing and receding contact angles.	131
Fig. 68. Monte Carlo error estimation technique.	134

Fig. 69. Finite difference model of the fin tip region. The solid fin and liquid are shown as shaded and unshaded, respectively. Heat is conducted within the fin and convected to the local liquid, which moves down the fin. 142

Fig. 70. Finite difference model showing liquid temperature increase due to local convection between rows $n+1$ and n . The solid fin and liquid are shown as shaded and unshaded, respectively. 143

Fig. 71. Finite difference model showing liquid temperature increase due to convection at the tip. The solid fin and liquid are shown as shaded and unshaded, respectively. 144

Fig. 72. Temperature profiles for various mass flow rates. Plots a) – d) show mass flow rates of $1000\bar{m}$, $10\bar{m}$, $2\bar{m}$, and \bar{m} , respectively, where \bar{m} is the average per fin mass flow rate used in the experiment. $h = 10,000 \text{ W/m}^2\cdot\text{K}$. 146

Fig. 73. Local heat flux as a function of position on fin. Solid symbols show heat flux off the top surface of the fin (rather than the top node in the model). $h = 10,000 \text{ W/m}^2\cdot\text{K}$. 147

Fig. 74. Single fin heat transfer as a function of heat transfer coefficient. 149

NOMENCLATURE

A	Area [m ²]
A_c	Cross-sectional area of the fin [m ²]
A_{flat}	Area of the flat (unenhanced) surface [m ²]
b	Laplace constant = $\sqrt{\frac{2\sigma}{g(\rho_l - \rho_v)}}$ [m]
$c_{Al_2O_3}$	Concentration of alumina [g/L]
c_{gas}	Concentration of gas [mol/mol]
c_p	Constant pressure specific heat [J/kg·K]
$c_{p,l}$	Constant pressure specific heat of the liquid [J/kg·K]
$c_{p,v}$	Constant pressure specific heat of the vapor [J/kg·K]
C	Constant in boiling correlations Channel width [m]
$C_{s,f}$	Constant in Rohsenow's (1952) correlation
CHF	Critical heat flux [W/m ²]
CHF _{nanofluid}	Critical heat flux with nanofluid [W/m ²]
CHF _{Zuber}	Critical heat flux predicted by Zuber's correlation [W/m ²]
CNT	Carbon nanotube
d	Diameter [m] Equilibrium break-off diameter in the correlation of Stephan & Abdelsalam (1980) = $0.146\theta b$ [m]
d_{10}	Arithmetic mean diameter [m]
d_{20}	Surface area mean diameter [m]
d_{30}	Volume mean diameter [m]

d_{32}	Volume-to-surface area (Sauter) mean diameter [m]
d_{max}	Maximum diameter in distribution [m]
d_{min}	Minimum diameter in distribution [m]
d_n	Orifice diameter [m]
d_o	Orifice diameter [m]
d_p	Mass median diameter [m]
d_{pq}	Mean diameter based on arbitrary orders p and q [m]
D_{eq}	Equivalent diameter based on area affected by a single impinging jet [m]
g	Acceleration due to gravity [m/s^2]
h	Heat transfer coefficient [$W/m^2 \cdot K$]
$h_{basefluid}$	Heat transfer coefficient when using base fluid [$W/m^2 \cdot K$]
h_{fg}	Latent heat of vaporization [J/kg]
h_{flat}	Heat transfer coefficient of the flat (unenhanced) surface [$W/m^2 \cdot K$]
$h_{nanofluid}$	Heat transfer coefficient when using nanofluids [$W/m^2 \cdot K$]
H	Henry's constant [atm^{-1}]
HX	Heat exchanger
k	Thermal conductivity [$W/m \cdot K$]
$k_{basefluid}$	Thermal conductivity of the base fluid [$W/m \cdot K$]
k_l	Thermal conductivity of the liquid [$W/m \cdot K$]
$k_{nanofluid}$	Thermal conductivity of the nanofluid [$W/m \cdot K$]
$k_{particle}$	Thermal conductivity of the particle [$W/m \cdot K$]
$k_{suspension}$	Thermal conductivity of the suspension [$W/m \cdot K$]

l	Liquid
L	Fin length [m]
m	Fin constant = $\sqrt{\frac{hP_f}{kA_c}}$ [m^{-1}]
\dot{m}	Mass flow rate [kg/s]
\bar{m}	Average per fin mass flow rate [kg/s]
n	Constant in Rohsenow's (1952) correlation
	Probability density function
	Number of measurements taken
	Number of fins on the microstructured surface
Nu	Nusselt number
Nu_{d32}	Nusselt number based on Sauter mean diameter
OD	Outer diameter
P	Pressure [Pa]
P_a	Ambient pressure [Pa]
P_f	Perimeter of the fin [m]
P_s	Stagnation pressure [Pa]
P_{sat}	Saturation pressure [atm]
P_T	Total pressure [atm]
Pr	Prandtl number
Pr_l	Prandtl number of the liquid
q	Heat transfer [W]
$q_{CHF,nanofluid}$	Heat transfer at CHF with nanofluid [W]

$q_{CHF,basefluid}$	Heat transfer at CHF with base fluid [W]
q_{flat}	Heat transfer from the flat (unenhanced) surface [W]
$q_{heatsink}$	Heat transfer from the entire microstructured surface [W]
$q_{sides+tip}$	Heat transfer from the sides and tip of a single fin [W]
q''	Heat flux [W/m ²]
q''_{CHF}	Critical heat flux [W/m ²]
q''_{flat}	Heat flux of a flat (unenhanced) surface [W/m ²]
\bar{Q}''	Mean volumetric flow flux [m/s]
R	Resistance [Ω]
R_0	Resistance at reference temperature [Ω]
R_{heater}	Heater resistance [Ω]
Ra_L	Rayleigh number based on plate length
$Re_{d_{32}}$	Reynolds number based on Sauter mean diameter
Re_{d_n}	Reynolds number based on nozzle diameter and velocity of the jet at the nozzle
Re_{d_o}	Reynolds number based on orifice diameter
s	Solid
t_{dwell}	Dwell time at peak temperature [min]
T	Temperature [K]
T_{bulk}	Bulk fluid temperature [K]
T_{inlet}	Temperature immediately upstream of the nozzle [K]
T_l	Local liquid temperature [K]
$T_{l,n}$	Nodal temperature of the liquid [K]

T_n	Nodal temperature of the fin [K]
T_{peak}	Peak temperature reached during oxidation [°C]
T_{tip}	Fin tip temperature [K]
T_{sat}	Saturation temperature [K]
T_{spray}	Spray temperature [K]
T_{wall}	Wall temperature [K]
TC	Thermocouple
v	Vapor
$v_{breakup}$	Droplet breakup velocity [m/s]
$v_{upstream}$	Velocity of flow upstream of the nozzle [m/s]
V	Voltage [V]
V_i	Supply voltage [V]
W	Fin width [m]
We_{d_o}	Weber number based on orifice diameter
x	Position [m]
	Arbitrary variable
X_1	Non-dimensional parameter in Stephan & Abdelsalam's (1980) correlation defined in Table 1
X_3	Non-dimensional parameter in Stephan & Abdelsalam's (1980) correlation defined in Table 1
X_4	Non-dimensional parameter in Stephan & Abdelsalam's (1980) correlation defined in Table 1
X_5	Non-dimensional parameter in Stephan & Abdelsalam's (1980) correlation defined in Table 1
X_{13}	Non-dimensional parameter in Stephan & Abdelsalam's (1980) correlation defined in Table 1

y	Arbitrary function
$y_{Al_2O_3}$	Mass fraction of alumina
α	Linear temperature coefficient of resistance [K ⁻¹]
α_l	Thermal diffusivity of the liquid [m ² /s]
Δa	Constant group contribution [J/mol·K]
Δb	Linear group contribution [J/mol·K ²]
Δc	Quadratic group contribution [J/mol·K ³]
ΔP	Nozzle pressure difference [Pa]
ΔT	Temperature difference [K]
ΔT_{sat}	$T_{wall} - T_{sat}$ [K]
ΔT_{sub}	$T_{sat} - T_{spray}$ [K]
ϕ	Volume fraction
$\phi_{Al_2O_3}$	Volume fraction of alumina
$\phi_{ethylene\ glycol}$	Volume fraction of ethylene glycol
$\phi_{particle}$	Volume fraction of the solid particles
η	Spray efficiency as typically defined
η'	Spray efficiency including all thermodynamic potential for heat transfer
μ	Dynamic viscosity [Pa·s]
$\mu_{basefluid}$	Dynamic viscosity of the base fluid [Pa·s]
μ_l	Dynamic viscosity of the liquid [Pa·s]
$\mu_{nanofluid}$	Dynamic viscosity of the nanofluid [Pa·s]

θ	Full-cone spray angle [degrees]
	Liquid/solid contact angle [degrees]
	Temperature difference ($T - T_{spray}$) [K]
θ_a	Advancing contact angle [degrees]
θ_{post}	Advancing contact angle after the experiment [degrees]
θ_{prior}	Advancing contact angle prior to the experiment [degrees]
θ_r	Receding contact angle [degrees]
θ_{wall}	$T_{wall} - T_{spray}$ [K]
$\rho_{Al_2O_3}$	Density of solid alumina [kg/m ³]
ρ_l	Liquid density [kg/m ³]
ρ_{mix}	Density of the mixture
$\rho_{pure\ liquid}$	Density of the base fluid
ρ_v	Vapor density [kg/m ³]
σ	Surface tension [N/m]
	Standard deviation [varies]
σ_A	Standard deviation of the area [m ²]
$\sigma_{dT/dx}$	Standard deviation of the temperature gradient [K/m]
$\sigma_{ellipse\ fit}$	Standard deviation of ellipse fit [degrees]
σ_k	Standard deviation of the thermal conductivity [W/m·K]
σ_{lv}	Liquid-vapor surface tension [N/m]
σ_{q^*}	Standard deviation of the heat flux [W/m ²]
σ_R	Standard deviation of the resistance [Ω]

σ_{sl}	Solid-liquid surface tension [N/m]
σ_{sv}	Solid-vapor surface tension [N/m]
σ_V	Standard deviation of the voltage [V]
$\sigma_{\bar{\theta}}$	Standard deviation of the average contact angle [degrees]

CHAPTER 1. INTRODUCTION

This dissertation was developed to improve the state of knowledge of spray cooling and advanced multi-phase heat transfer technologies. To begin, the specific motivation for this work, a brief review of background material, and the objectives of the research are discussed. A detailed review of the literature follows in Chapter 2.

1.1. Motivation

Modern technology demands power and in an ever decreasing package size. As functions are increased and devices shrink, heat density increases. For example, the high heat fluxes created by high performance electronics offer great challenges to the engineering community. Advanced liquid immersion cooling techniques such as boiling and spray cooling are particularly effective for addressing these types of high heat density problems.

Two-phase systems utilizing boiling or liquid evaporation have long been recognized as having the potential to remove large amounts of heat at low temperature difference. One such system is spray cooling, in which an atomizing nozzle provides a flow of liquid droplets directed at a hot surface. The primary disadvantages of spray cooling systems include large weight, cost, and complexity. However, exceptionally high heat transfer rates can be achieved because vapor removal from the surface is much easier than with other two-phase systems.

Spray cooling technology has been applied in a variety of applications including: metal quenching, reducing scarring during medical procedures (e.g., port-wine scar removal), cooling multichip modules within supercomputers, and cooling Commercial Off-The-Shelf (COTS) based military electronics. It is also being considered for

application to advanced defense systems, computer processor test and evaluation, and automotive systems.

Given the many applications of high heat flux technology, there is always a desire to increase the thermal performance of existing technologies. This thesis explores two potentially powerful techniques that may be capable of improving traditional spray cooling: nanofluids and extended surfaces. These techniques are reviewed, tested, analyzed, and modeled.

1.2. Background

Sprays in general find wide use in applications including agriculture, food processing, painting, combustion, fire suppression, and metal quenching as well as high heat flux electronics. The methods of atomization and resulting spray profiles are equally diverse. Pressure atomization can be achieved by forcing a liquid at high velocity through a small orifice. This can be a simple orifice or a more complex design. Many designs exist including those that cause the liquid to impact specially designed structures as well as those utilizing complex liquid injection and diverging liquid streamlines. The most common design is the pressure swirl atomizer, which works by tangentially injecting liquid to generate a vortex in the swirl chamber that draws ambient air into the nozzle (Nasr et al., 2002) (see Fig. 1). This causes the liquid to emerge from the nozzle as an unstable cylindrical sheet with axial and tangential velocity. A pressure atomizing nozzle was used in the present work, although many other types of atomizers exist such as gas-assisted and ultrasonic. Nozzles can be designed to create many different spray profiles including circular, square, or flat. In spray cooling, the nozzles are typically

manufactured to create: 1) a hollow cone in which the majority of the droplets land along the perimeter or 2) a full cone with nominally uniform droplet distribution.

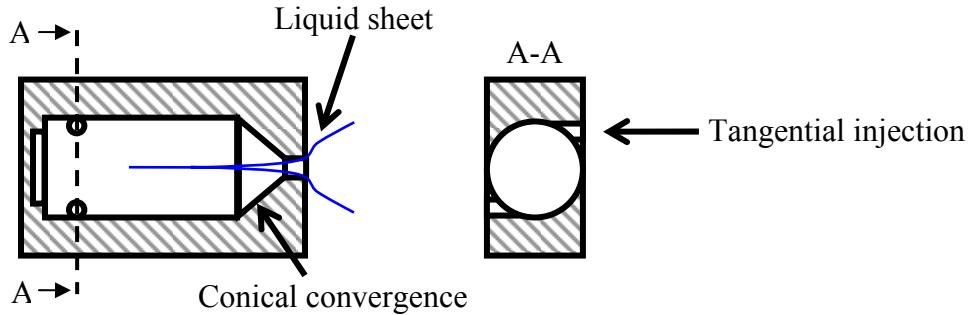


Fig. 1. Swirl atomizer schematic.

The basic mechanisms by which heat is removed during spray cooling are poorly understood because it is a technology that combines a number of fundamentally complex thermo/fluid dynamics processes. Furthermore, the heat transfer is highly dependent on the amount of liquid on the surface. At one extreme, the liquid flow rate is sufficient to create a continuous liquid film. This film is subject to mixing caused by incoming droplets, gas entrainment, boiling, and evaporation (see Fig. 2). At the opposite extreme, a relatively dry surface can result from a sparse spray (low volume flow rate) and/or high surface temperature. With a dry surface, boiling in a traditional sense may be of less importance than dropwise evaporation and droplet impact effects (see di Marzo (1996) for a detailed discussion of heat transfer in this regime). In this case, the distribution of droplet sizes and velocities due to the atomization method strongly affect the heat transfer rate. These droplets may splash, rebound, and coalesce on the surface. Individual droplets and droplet pools are then free to evaporate as they are pushed off the heated surface by the liquid's radial momentum.

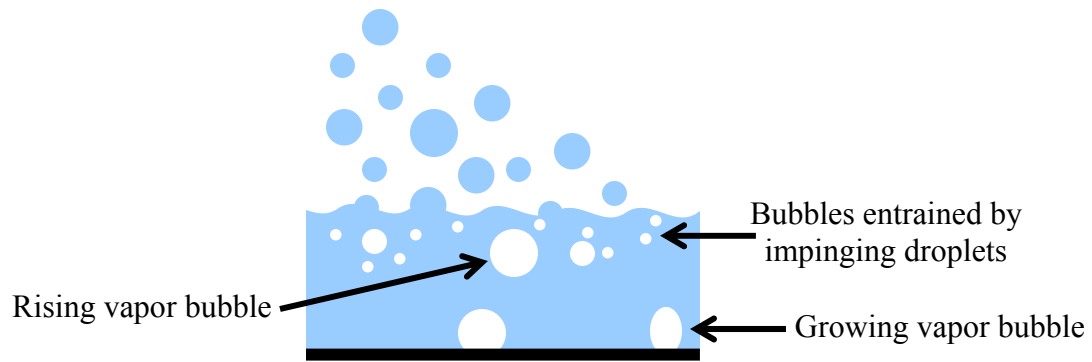


Fig. 2. Illustration of spray cooling into a continuous liquid film.

One aspect of spray cooling is basic boiling phenomena, which should be considered as a prerequisite to the more complex process of spray cooling. Therefore, consider boiling in the absence of an incoming spray. Boiling is a highly efficient means of heat transport in which liquid is vaporized due to the temperature of the liquid exceeding the saturation vapor pressure. Many people might also add the requirement that bubbles be present to make a distinction with non-boiling evaporation (but no such distinction will be made here). In boiling, heat can be removed by increasing the temperature of the liquid (sensible heating) as well as the vaporization process (latent heating). Typically, a large amount of heat can be removed at relatively low temperature difference. Boiling heat transfer is usually characterized by a boiling curve (Fig. 3) with various boiling regimes.

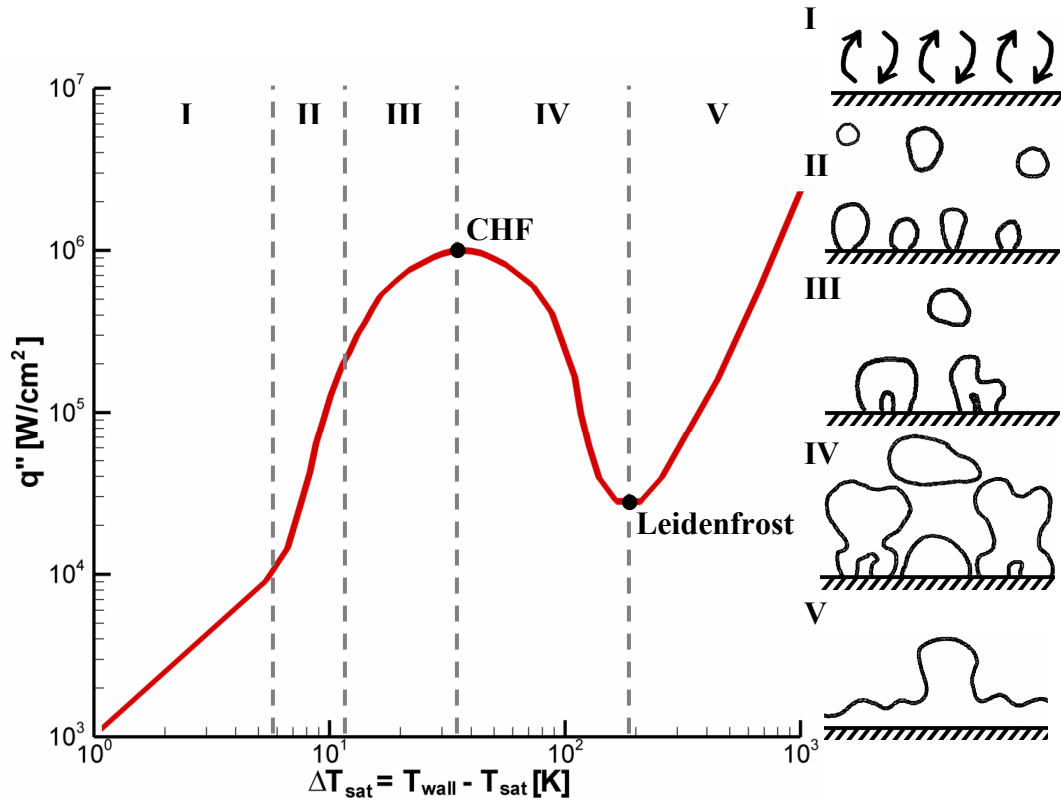


Fig. 3. Typical boiling curve and associated boiling regimes.

In the first regime (Fig. 3, I), free convection occurs when no vapor can be generated due to low wall superheat and insufficient nucleation sites. This single-phase regime can be treated analytically or with correlations such as Churchill and Chu (1975). This regime ends when bubble generation begins. Even this simple regime will be quite complicated in spray cooling because of the motion of the liquid film and the mixing caused by impinging droplets.

The nucleate boiling regime (Fig. 3, II - III) begins once bubbles are generated and is characterized by two sub-regimes. The first is the isolated bubble regime (Fig. 3, II), where bubbles form at their own nucleation sites and depart distinctly. Following this sub-regime, at higher wall superheat, the departure frequency is so great that bubbles

immediately begin to coalesce both horizontally and vertically. This is the regime of slugs and columns (Fig. 3, III).

Following the nucleate boiling regime, the boiling curve continues to the local maximum heat flux termed critical heat flux (CHF) or the burnout heat flux. This occurs due to vapor generation that is so great that liquid can no longer come into contact with the heater surface. With insufficient supply of cold liquid to cool the surface, heat must be transported through the vapor. Heat transfer through the vapor is less efficient (due to its lower thermal conductivity) and results in a decrease in the heat flux. It represents a thermal design limit for many applications since at this point the heat flux declines as the temperature rises, which ultimately causes device failure.

The transition boiling regime (Fig. 3, IV) follows CHF and is characterized by increasing wall temperature and decreasing heat flux. This is due to an increase in the dry area covering the heater. This regime is of little practical interest because it is unstable and quickly results in the film boiling regime. However, it is important to note that any constant heat flux experiment that drives the heater to CHF will inevitably drive the heater into the transition boiling regime. The higher temperatures and exposure to dissolved gases may cause changes to the surface microstructure.

Eventually, a local minimum in the boiling curve is reached, the Leidenfrost point. At this point, the surface enters the film boiling regime (Fig. 3, V). In the film boiling regime, heat must be conducted across a continuous vapor film before it can be transferred to the liquid. This inefficient process can result in large heat fluxes, but the temperatures required are very high. The film boiling regime is therefore unpractical as a means of cooling many practical devices, but it is important in spray quenching of metals.

Boiling, like spray cooling, is also incompletely understood by the research community. While this dissertation has focused on enhancing spray cooling, this goal can only be achieved given thorough understanding of basic boiling phenomena. The preceding background will be extended in the next chapter when the relevant literature concerning boiling, spray cooling, nanofluids, and extended structure are reviewed in detail.

1.3. Research Objectives

This thesis sheds light on the fundamental mechanisms responsible for two powerful heat transfer enhancement techniques: nanofluids and extended surfaces. The primary objectives of this research were as follows:

1. Determine the mechanisms by which heat transfer is enhanced during spray cooling of extended surfaces.
2. Determine whether nanofluids improve or degrade boiling heat transfer.
3. Determine the suitability of nanofluids for spray cooling.
4. Determine the mechanisms by which nanofluids improve/degrade heat transfer.

These objectives were met through a systematic experimental approach that investigated the fundamental mechanisms underlying the boiling and spray cooling processes.

First, the mechanisms behind the performance enhancement provided by spray cooling heat sinks with straight fins were studied. Straight fins are known to improve spray cooling heat transfer (Silk et al., 2004, 2005, 2006), but the precise mechanisms underlying the enhancement remained elusive. The heat sinks used in this study were

electric discharge machined (EDM) to have a channel width of 0.36 mm, fin width of 0.50 mm, and lengths of 0.25 mm, 0.50 mm, 1.0 mm, 3.0 mm, and 5.0 mm. The high aspect ratio of these channels provided an increase in surface area of up to 13 times the baseline. With such a large increase in area, the spray was utilized more effectively. In fact, one goal of this study was to add enough fin area that the entire spray could be evaporated as droplets flowed down the long channels. Furthermore, varying only the fin length provided an opportunity to study the relative spray utilization provided by the increased area. The effect of increased fin length is discussed in detail along with its pronounced effect of the spray efficiency.

Second, experiments were designed to test whether nanofluids are truly capable of enhancing boiling heat transfer. The literature contains a diverse range of conclusions, and as of yet, no consensus has emerged. This thesis has specifically investigated the role of surface wetting on the nanofluid boiling system. A water-based nanofluid was tested on copper and copper oxide surfaces. Surface wetting was systematically improved by increasing the thermal oxide layer on the copper surface. Ethanol-based nanofluids with better wetting characteristics were also used over a concentration range of 0.001 g/L to 10 g/L on glass, gold coated, and copper surfaces. These experimental results were compared to the literature and the effect of surface wettability is discussed in detail.

Finally, spray cooling of nanofluid was considered. A scaling analysis was developed to illustrate the challenges of nanofluid spray cooling and experimental results are presented.

CHAPTER 2. LITERATURE REVIEW

The literature review for this dissertation is divided into four sections. The first two sections concern the general features of boiling and spray cooling, respectively. These sections provide the necessary background information as well as describing the state of the art in spray cooling technology. The third section reviews the literature regarding nanofluids, including their synthesis, properties, and application to evaporative heat transfer systems. The final section reviews enhanced and extended surfaces in both boiling and spray cooling systems.

2.1. Boiling Heat Transfer

Boiling provides very high heat transfer rates and has been studied for many years in both stagnant pool and flow boiling configurations, yet it remains poorly understood. Much of the confusion is directly related to the stochastic nature of the nucleation process.

2.1.1. Nucleate Boiling

Nucleate boiling is affected by many parameters, the most important being heat flux, saturation pressure, and thermophysical properties (Pioro et al., 2004). Other properties such as surface material, finish, and microstructure are also known to affect pool boiling but the precise functional form of these effects remains unknown (Pioro et al., 2004). These surface properties and the ability of the liquid to wet the surface are key to determining the number of active nucleation sites (micro sized gaps in the surface that trap gas/vapor to serve as bubble embryos). The nucleation site density then largely

determines the amount of latent heat transport and the degree of mixing caused by bubble departure.

Some of the dominant heat transport mechanisms occurring during the nucleate boiling regime are shown in Fig. 4. Conduction from the heated surface into the bulk fluid creates a superheated liquid layer (Fig. 4, left), which in turn drives evaporation near the base of the bubble (Fig. 4, middle). In a saturated pool, there would be evaporation around the entire bubble. In a subcooled pool, the colder bubble cap would serve as a condensation region, which would allow the bubble to serve as a kind of heat pump. Bubble detachment will occur when the buoyancy force (in combination with external body forces) exceeds the surface tension force holding the bubble on the surface. Then, the heated surface will be rewetted by fresh cold liquid (Fig. 4, right). Following rewetting, the superheated liquid layer must be regrown, which begins the heat transfer cycle anew. The specifics of each of these mechanisms and the relative contribution of each remains a topic of debate (Henry, 2005; Moghaddam, 2006) and are beyond the scope of the present work.

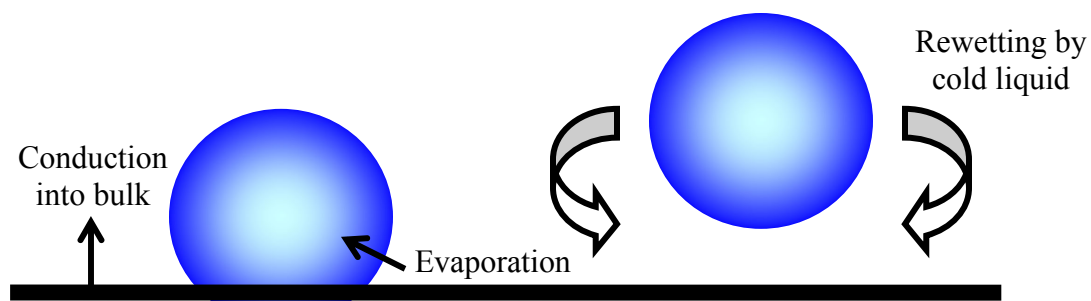


Fig. 4. Simplified illustration of nucleate boiling heat transfer mechanisms.

Despite incomplete understanding and much disagreement, pool boiling heat transfer is often estimated using the Rohsenow (1952) correlation:

$$q'' = \mu_l h_{fg} \left[\frac{g(\rho_l - \rho_v)}{\sigma} \right]^{1/2} \left(\frac{c_{p,l} \Delta T_{sat}}{C_{s,f} h_{fg} Pr_l^n} \right)^3 \quad (1)$$

In addition to the numerous thermophysical properties that appear in Eq. 1, two parameters, $C_{s,f}$ and n , account for surface-liquid combination. While errors as large as $\pm 100\%$ are not uncommon (Incropera & Dewitt, 1996), it is a useful estimate of magnitude and captures the important dependence of wall superheat.

Another set of nucleate boiling correlations were developed by Stephan and Abdelsalam (1980). They used nearly 5000 data points available from the literature in a regression analysis that determined Nusselt number as a function of various non-dimensional parameters that varied depending on the working fluid. For water they suggested:

$$Nu = 0.246 \cdot 10^7 X_1^{0.673} X_4^{-1.58} X_3^{1.26} X_{13}^{5.22} \quad , \quad (2)$$

where the non-dimensional parameters are defined in Table 1. For hydrocarbons such as ethanol, they suggested:

$$Nu = 0.0546 (X_5^{0.5} X_1)^{0.67} X_{13}^{-4.33} X_4^{0.248} \quad (3)$$

Since these correlations were developed based on a large experimental dataset, the expected errors are much smaller: The authors quoted mean absolute errors of 11.3% and 12.2% for water and hydrocarbons, respectively.

Table 1. Nondimensional parameters in the correlations of Stephan and Abdelsalam (1980).

Non-dimensional Parameter	Definition
X_1	$q'' d / (k_l T_{sat})$ (4)
X_3	$c_{p,l} T_{sat} d^2 / \alpha_l^2$ (5)
X_4	$h_{fg} d^2 / \alpha_l^2$ (6)
X_5	ρ_v / ρ_l (7)
X_{13}	$(\rho_l - \rho_v) / \rho_l$ (8)

2.1.2. Critical Heat Flux

CHF marks the turning point when heat transfer starts to decline due to high wall superheat. It also remains a poorly understood phenomena, in part due to difficulties in observing the near wall region which likely controls the dry-out mechanism. Suggested CHF mechanisms include the hydrodynamic instability model (Zuber, 1959), the bubble-packing model (Rohsenow & Griffith, 1956), and the macrolayer model (Haramura & Katto, 1983). However, these models neglect many factors that have been shown to affect CHF such as gravity, surface finish and wettability, heater dimensions, and heater thermal properties among others.

Despite these shortcomings, a need to predict CHF has resulted in a number of correlations. Based on dimensional analysis and hydrodynamic instability analysis, Kutateladze (1952) and Zuber (1959) respectively developed correlations of the following form:

$$q''_{CHF} = Ch_{fg}\rho_v \left[\frac{\sigma g(\rho_l - \rho_v)}{\rho_v^2} \right]^{1/4} \left(\frac{\rho_l + \rho_v}{\rho_l} \right)^{1/2} \quad (9)$$

The constant C varies depending on the model. Kutateladze (1952) showed that values of 0.13 – 0.19 could correlate the data from various studies available at the time. In the most widely used form, the Zuber (1959) correlation, the constant is equal to $\pi/24$. The Zuber correlation is of particular importance in the present research because so much of the nanofluid research reported in the literature has been analyzed in light of this correlation. However, it is important to note that Zuber neglected surface wettability effects, which will be shown to be of great importance in nanofluid boiling.

2.1.3. Surface Wettability

The importance of the surface microstructure mentioned above is in part a result of surface wettability effects (note: Appendix A gives some background information on wettability and defines the various contact angles of interest). Both the advancing and receding contact angles are important throughout much of the boiling curve. The initial nucleation site density is determined in part by the liquid's ability to trap vapor/gas nuclei in the microstructure of the boiling surface. Highly wetting fluids like R-113 and FC-72 can result in fewer nucleation sites and large superheat excursions at boiling incipience (You et al., 1990). This effect is governed by the advancing contact angle. The advancing angle is again important during rewetting of dry surfaces as bubbles lift off the boiling surface (Demiray & Kim, 2004).

The receding contact angle is important during the bubble growth period as the vapor pushes liquid away to create a larger dry patch. With a smaller contact angle, a thinner wedge of liquid is created between the heater and the liquid-vapor bubble interface, which promotes evaporation. The receding contact angle may also be important in determining when CHF occurs since CHF may occur when vapor blankets the surface due to a pushing back of the liquid (Kandlikar, 2001).

Metallic oxides in particular are known to improve CHF by increasing the wettability of the surface (Tachibana et al., 1967; Liaw & Dhir, 1989; Takata et al., 2005). Tachibana et al. (1967) tested over 400 metallic plates in saturated water pool boiling at atmospheric pressure. They heated the plates to physical destruction and found aluminum to have a much higher CHF due to a native oxide film that developed soon after the initiation of boiling and spread throughout the experiment. Furthermore,

stainless steel that was coated with aluminum was found to have a similar enhancement. They believed this higher CHF was due to the oxide's "good affinity" for water. Liaw and Dhir (1989) measured CHF on a vertical copper surface in a saturated water pool at 1 atm. They systematically decreased the static contact angle by heating the copper surface in air to create a thermal oxide. By varying the peak temperature and the amount of time the surface was subjected to heating, the contact angle was decreased from 90° to 14°. CHF was observed to increase by ~90% as the contact angle was decreased.

2.2. Spray Cooling

As previously mentioned spray cooling is comprised of many complex thermo/fluid dynamics processes. It begins when flow instabilities shatter the liquid into many fine droplets of varying size.

2.2.1. Droplet Features

Atomization creates an array of droplet sizes, which can be measured with laser diffraction or phase Doppler anemometry (PDA). However, it is often more convenient to use an average droplet size to characterize the spray. A general expression for mean diameter is given by Nasr et al. (2002):

$$\bar{d}_{pq} = \left[\frac{\int_{d_{\min}}^{d_{\max}} d^p n(d) \delta d}{\int_{d_{\min}}^{d_{\max}} d^q n(d) \delta d} \right]^{1/(p-q)}, \quad (10)$$

where $n(d)$ is the probability density function and p and q are orders (e.g. 1, 2, or 3). Using this framework various definitions of mean diameter can be used as different applications dictate (see Table 2).

Table 2. Various definitions of mean diameter.

Description	Equation
Arithmetic mean diameter	$\bar{d}_{10} = \int_{d_{\min}}^{d_{\max}} dn(d) \delta d \quad (11)$
Surface area mean diameter	$\bar{d}_{20} = \left[\int_{d_{\min}}^{d_{\max}} d^2 n(d) \delta d \right]^{1/2} \quad (12)$
Volume mean diameter	$\bar{d}_{30} = \left[\int_{d_{\min}}^{d_{\max}} d^3 n(d) \delta d \right]^{1/3} \quad (13)$
Volume-to-surface area mean diameter (Sauter mean diameter)	$\bar{d}_{32} = \frac{\int_{d_{\min}}^{d_{\max}} d^3 n(d) \delta d}{\int_{d_{\min}}^{d_{\max}} d^2 n(d) \delta d} \quad (14)$

In spray cooling, it has been common to use the Sauter mean diameter (SMD), perhaps because it captures both the volume and surface area characteristics of the spray. Estes and Mudawar (1995) developed a SMD correlation for FC-72, FC-87, and water:

$$\frac{d_{32}}{d_o} = 3.67 \left(We_{d_o}^{1/2} Re_{d_o} \right)^{-0.259}, \quad (15)$$

where the Weber and Reynolds numbers are defined as:

$$We_{d_o} = \frac{\rho_v \left(\frac{2\Delta P}{\rho_l} \right) d_o}{\sigma} \quad (16)$$

$$Re_{d_o} = \frac{\rho_l \left(\frac{2\Delta P}{\rho_l} \right)^{1/2} d_o}{\mu_l} \quad (17)$$

Eq. 15 was used in the present work because it was developed with similar working fluids, although many more SMD correlations are available (see Liu, 2000).

Another key feature of droplets is velocity. The distribution of droplet velocities obviously depends on the method and degree of atomization. Ghodbane and Holman (1991) used an energy balance to determine the break-up velocity, Eq. 18.

$$v_{breakup} = \left(v_{upstream}^2 + \frac{2\Delta P}{\rho_l} - \frac{12\sigma}{\rho_l d_p} \right)^{1/2} \quad (18)$$

However, the differential pressure term usually dominates. Therefore, in the present work, the droplet velocity has been estimated while neglecting the other two terms.

2.2.2. Parameters Affecting Spray Cooling

There are many important parameters that control spray cooling heat transfer (Table 3). One of the greatest challenges in the study of spray cooling is the inability to independently and precisely control these parameters. For example, mass flux can be increased by increasing the differential pressure in a pressure atomizing spray. However, this increase in pressure strongly affects droplet breakup; completely altering droplet size, number, and velocity.

Table 3. Important parameters affecting spray cooling.

Spray properties	Droplet size & distribution
	Droplet number flux
	Droplet velocity & distribution
	Mass flux & distribution
	Spray angle
Fluid properties	Thermal conductivity of liquid
	Surface tension of liquid
	Specific heat of liquid
	Latent heat of vaporization
Substrate properties	Superheat
	Thermal conductivity of substrate
	Substrate finish
Environmental properties	Subcooling
	Foreign nuclei
	Gravity
	Ambient gas density
	Ambient gas viscosity

Of these parameters, spray properties have received the most attention. Chen et al. (2002) studied the relative importance of mean droplet size, droplet flux, and droplet velocity on CHF. They used more than 20 full cone nozzles at a variety of nozzle pressures and standoff distances to systematically vary one of the above parameters while holding the other two constant. Over 3000 combinations of the three spray parameters were generated, although only a small subset of these satisfied the criteria of two parameters being constant. They found that the mean droplet velocity had the greatest effect on CHF, followed by the droplet number flux. Both the CHF and heat transfer coefficient increased as these parameters were increased. The Sauter mean diameter was found to be of little importance.

The effect of mass flow rate appears to be completely dependent on the total amount of liquid supplied. Thermodynamically, heat transfer is limited to:

$$\dot{m}(c_p \Delta T + h_{fg}) \quad (19)$$

In a sufficiently dilute spray, most of the mass supplied can be heated and vaporized. In these cases, heat transfer increases as the mass flow rate increases. With a dense spray, much of the liquid flows off the surface and heat transfer may be insensitive to increases in the mass flow rate (Sehmbey et al., 1994). Yang et al. (1996) found that in the nucleate boiling regime the heat transfer increased with increasing flow rate until a limit of 3 L/hr, when the improvement ceased. Tilton et al. (1992) found that heat transfer increased as the coolant flow rate was increased, provided the module was not flooded. Many others have also found that heat transfer increased as mass flow increases (e.g., Pais et al., 1992; Mudawar & Estes, 1996; Lin & Ponnappan, 2004; Pautsch & Shedd, 2005; Rybicki & Mudawar, 2006; Sakamoto et al., 2006).

Subcooling also has been found to increase CHF because more sensible heat is required to heat the liquid to the saturation temperature (Estes & Mudawar, 1995a; Horacek et al., 2005; Rybicki & Mudawar, 2006). However, the increase in CHF comes at the expense of a lower heat transfer coefficient (Tilton et al., 1992; Horacek et al., 2005).

Surface finish is an important parameter affecting spray cooling and of particular importance in the present work. It has been argued that increasing the surface roughness decreases the heat transfer by increasing the thickness of the liquid film on the surface (Pais et al., 1992). Pais et al. note that a roughened surface will have regions that are too deep and those which are too high. In the deep troughs of the surface, impinging drops will have to penetrate further to disturb growing bubbles and mix the fluid. Additionally, troughs suffer from a larger conduction resistance through the thick film to the free surface where evaporation is occurring. Peaks in the surface may suffer from having too thin a liquid film causing these regions to prematurely dry out. In their experimental investigation of spray cooling a copper block with water, they showed that a 0.3 μm grit roughened surface greatly outperformed 14 μm or 22 μm grit roughened surfaces. However, their conclusions may only be applicable in systems that are primarily governed by thin film evaporation; and depending on the spray parameters, this may not be the most important mechanism governing heat transfer.

For example, Kim et al. (2004b) investigated air-assisted spray cooling of a microporous surface with water. They found performance enhancements $\sim 50\%$ at CHF for the microporous surface, which the authors attribute to capillary pumping of liquid on top and within the surface. However, they used very modest flow rates of 1.25 mL/min -

3 mL/min, and it is not clear whether this enhancement would transfer to the higher flow rates that are of greater industrial significance.

2.2.3. Models of Spray Cooling

The simplest (and often quite accurate) model of spray cooling is that of single-phase convection. Numerous researchers have observed that spray cooling heat transfer can be linear with respect to wall-to-spray temperature difference (particularly when the superheat is modest) (e.g. Pautsch & Shedd, 2005; Estes & Mudawar, 1995a). This indicates negligible two-phase effects. Heat transfer is enhanced by maximizing the sensible heating of the spray and preventing vaporization, which leads to CHF (Pautsch & Shedd, 2005). In these studies the flow rate is often very large and as the flow rate is increased, the heat transfer improves and the model becomes more accurate. However, this results in an inefficient system that requires large pumps and fluid inventory. Indeed, these systems are very similar in performance to impinging jets. For example, Fabbri et al. (2003) compared sprays to microjets and found that sprays outperformed jets only at low flow rates and were inferior when considering both systems at constant pumping power. However, Estes and Mudawar (1995a) found that sprays usually outperformed jets given a constant flow rate, but the performance enhancement at larger subcooling was modest. They attributed the spray cooling performance to a more secure liquid film.

In many cases, better heat transfer can be achieved by utilizing multiphase effects. The simplest two-phase model of spray cooling heat transfer is that the spray creates a thin-film on the surface of the heater. Heat is then conducted through the film and evaporation occurs at the free surface. The impinging droplets are thought to increase the

conductance of this layer through improved mixing (Sehmbey et al., 1994). To maximize heat transfer, the liquid film must be made as thin as possible. Pautsch and Shedd (2006) used a four nozzle array and found that the regions with the poorest thermal performance had the thickest films. Pais et al. (1992) illustrated the effect clearly by studying surfaces with different surface roughness. They found that with a roughness greater than 1 μm , nucleation is primarily responsible for performance. However, when the liquid film was of order 0.1 μm , heat was primarily transferred through film evaporation. They observed up to 1200 W/cm^2 with a water spray that created such a thin film.

The thicker films mentioned above leads to the second basic model, which is nucleation dominated flow boiling. If the spray creates a thick enough liquid film, then the performance may be similar to that of typical boiling systems. In these systems, the heat transfer may be dominated by the nucleation site density on the solid surface. However, there is evidence to suggest that the impinging drops make the nucleation process very different.

In the secondary nucleation model, the large nucleate and convective heat transfers observed are attributed to so called “secondary nuclei” (Yang et al., 1996; Rini et al., 2002). When droplets enter the liquid film they are thought to entrain vapor, which serves as an additional nucleation site. Also, if a droplet breaks up a growing bubble, the nucleation site density is further increased. Rini et al. (2002) found that the heat transfer increases as the droplet number flux increases, which they attribute to a corresponding increase in the number of secondary nuclei. Furthermore, the ratio of nucleate to convective heat transfer was unaffected by the droplet number flux, which suggests that

secondary nuclei and turbulent mixing of the droplets enhances nucleate boiling and convection similarly.

Horacek et al. (2004, 2005) proposed another mechanism for two-phase spray cooling heat transfer: contact line heat transfer. They used the total internal reflectance (TIR) technique to determine the wet and dry portions of the heated surface. They then calculated the wetted area fraction and the contact line length. The heat flux (once corrected for sensible heat) was found to be well correlated with the contact line length, which also increased to a local maximum like CHF. Interestingly, wetted area fraction was found to decrease monotonically as superheat increased and could not be correlated with heat flux. This suggests that contact line heat transfer and not wetted area is responsible for two-phase portion of the heat transfer.

Critical heat flux mechanisms in spray cooling may be slightly different than in typical boiling systems. It is generally agreed that CHF begins with dryout around the perimeter of the heater (Sehmbey et al., 1994; Kim, 2006). However, Pautsch and Shedd (2006) noticed that CHF occurred first at the center of their heater due to it having the largest local film thickness.

No validated model of CHF for spray cooling exists, but there are some possible mechanisms. With a sufficiently sparse spray, CHF will occur when the liquid supply is exhausted due to evaporation. Droplets hitting dry surface will quickly evaporate. Those droplets forming pools will boil like a typical pool. This is consistent with the visual observations of Hsieh et al. (2004).

If liquid is in sufficient supply, then CHF may be caused by a “choking” of the liquid supply by bubbles generated in the liquid film as suggested by Sehmbey et al.

(1994). This could be due to escaping vapor preventing drops from hitting the surface or the ejection of liquid from the surface caused by the bursting of bubbles. Chow et al. (1995) developed a CHF model of spray cooling based in part on the macrolayer dry-out model of Haramura and Katto (1983). In this spray cooling model, increasing bubble production in the liquid film leads to a larger vapor bubble. This large bubble is then broken by an impinging drop (or due to its own internal pressure) causing the liquid above the bubble to be ejected from the surface. If fresh droplets cannot replenish the surface before the remaining macrolayer evaporates, then CHF will be triggered.

With all of these models in mind it is important to note that the applicability of the model may vary significantly with mass flux. Dilute sprays may appropriately be considered mere extensions of discrete droplets. In these cases, evaporative effects may dominate. The opposite extreme, with large mass flow, may create such a thick liquid film that the process more closely resembles single-phase impinging jet flow. Between these two extremes lies the complex mechanisms of spray boiling.

2.2.4. Spray Cooling Correlations

A number of correlations have been developed to predict the heat transfer of sprays. Rybicki and Mudawar (2006) developed the following single-phase correlation based on their own PF-5052 data and the water spray data of Mudawar and Valentine (1989):

$$Nu_{d_{32}} = 4.70 Re_{d_{32}}^{0.61} Pr_l^{0.32} \quad , \quad (20)$$

where the Nusselt and Reynolds numbers are defined in Eq. 21 and 22, respectively.

$$Nu_{d_{32}} = \frac{q'' d_{32}}{(T_{wall} - T_{inlet}) k_l} \quad (21)$$

$$Re_{d_{32}} = \frac{\rho_l \bar{Q}'' d_{32}}{\mu_l} \quad (22)$$

They found that the correlation fit the data with an overall mean absolute error of 13.1%.

Shedd and Pautsch (2005) developed a correlation for the heat transfer coefficient based on energy transfer. For a single nozzle they gave the following equation:

$$h = 0.4627 \rho_l c_{p,l} \bar{Q}'' + 0.01612 \bar{Q}'' \Delta T_{sat} \quad , \quad (23)$$

where the units are h (W/cm²·K), ρ_l (kg/m³), $c_{p,l}$ (kJ/kg·K), \bar{Q}'' (mL/s·cm²), and ΔT_{sat} (K).

Their correlation is based on summing a sensible heat contribution with a two-phase contribution that is linearly proportional to the superheat. This is in part based on the thermodynamic limits to heat transfer given in Eq. 19. This obviously simplified relation captures two important effects: flow rate dependence and the linear effect of wall temperature. However, most thermophysical properties are not included in Eq. 23, with their effect being included in the constants. This correlation is probably only appropriate over a limited range of flow rates, subcoolings, heater sizes. In fact, the authors had to develop another correlation with an additional constant to fit their multiple-nozzle data.

A general CHF correlation for pressure and air-atomizing sprays was developed by Chow et al. (1995). The maximum deviation of the seven datasets they used from the correlation was ~30%.

$$\frac{q''_{CHF}}{\rho_l \bar{Q}'' h_{fg}} = 0.38 \left(\frac{\sigma}{\rho_l \bar{Q}''^2 d_{32}} \right)^{1/3} \left(\frac{\rho_v}{\rho_l} \right)^{1/2} \left(\frac{P_s}{P_a} \right)^{1/4} \quad (24)$$

Another CHF correlation was proposed by Mudawar and Estes (1996). They varied the nozzle-to-surface distance and found that CHF was maximized when the spray impact cone just inscribed the heater surface. With too short a nozzle spacing, droplet impingement was limited to a small portion of the heater and CHF was lower.

Conversely, when the spacing was too large, much of the liquid was wasted due to overspray. Based on these observations, they developed a correlation based on the average volumetric flux over the spray impact area:

$$\frac{q_{CHF}''}{\rho_v h_{fg} \bar{Q}''} = 1.467 [(1 + \cos(\theta/2)) \cos(\theta/2)]^{0.3} \left(\frac{\rho_l}{\rho_v} \right)^{0.3} \left(\frac{\rho_l \bar{Q}''^2 d_{32}}{\sigma} \right)^{-0.35} \left(1 + 0.0019 \frac{\rho_l c_{p,l} \Delta T_{sub}}{\rho_v h_{fg}} \right) \quad (25)$$

2.3. Nanofluids

The term nanofluid refers to heat transfer fluids developed by suspending nanocrystalline particles in conventional liquids (Eastman et al., 1997). Two common procedures for producing nanofluid include the dispersion of nanocrystalline powders and evaporation of a precursor material that condenses directly into the base liquid. The dispersion technique is particularly common since nanoparticle powders have for many years been routinely created for traditional applications such as cosmetics, abrasives, and coatings. However, nanoparticles are naturally unstable due to the reduction in Gibbs free energy associated with coalescence and the loss of surface area (Friedlander, 2000). Therefore, complicated and often proprietary additions to the base fluid are required to maintain suspension. Even with these additives the suspensions are prone to settle due to gravity, in the absence of other dispersive forces. Furthermore, particles will coagulate if the suspension is vaporized or the dispersant is thermally degraded.

2.3.1. Thermal Conductivity Enhancement

Nanofluids have attracted much recent attention because of what many researchers have called “anomalously high” thermal conductivity. Traditionally, the

Hamilton-Crosser (1962) equation[†] has been used to predict the thermal conductivity of suspensions:

$$\frac{k_{suspension}}{k_{basefluid}} = 1 + \frac{3\phi}{\frac{k_{particle} + 2k_{basefluid}}{k_{particle} - k_{basefluid}} - \phi} \quad (26)$$

Equation 26 can be greatly simplified by making two assumptions. First, assume that the particle has a much larger thermal conductivity than the base fluid ($k_{particle} \gg k_{basefluid}$).

Then, Eq. 26 simplifies to:

$$\frac{k_{suspension}}{k_{basefluid}} = \frac{1 + 2\phi}{1 - \phi} \quad (27)$$

Then, making the dilute suspension assumption ($\phi \ll 1$), the enhancement reduces to a simple linear relation:

$$\frac{k_{suspension}}{k_{basefluid}} = 1 + 3\phi \quad (28)$$

The Hamilton-Crosser equation was verified for microscale particles but clearly includes no dependence on particle size. Therefore, it could theoretically be applied to nanoparticle suspensions. However, recent experimental work has shown that it often underpredicts the thermal conductivity of nanofluids (Gandhi, 2007).

A number of investigators have used the transient hot-wire technique to determine the thermal conductivity enhancement of nanofluid. In one such study, Eastman et al. (1997) determined the thermal conductivity enhancement of the following nanofluids: Al₂O₃/water, CuO/water, Cu/HE-200 oil, and Cu/Duo-seal oil (see Fig. 5). The water based suspensions were found to have linear enhancements, but the enhancements were

[†] Note that the often cited Eq. 26 is based on Maxwell's (1873) work on electricity and magnetism and is only valid for spherical particles, or non-spherical particles when the conductivity ratio is not too large ($k_{particle}/k_{basefluid} < 100$). In fact, the majority of Hamilton and Crosser's 1962 paper is about predicting the thermal conductivity of a mixture with non-spherical particles. In that case, the 3 and 2 in Eq. 26 should be replaced by n and $n-1$, respectively, where n is equal to 3 divided by the sphericity of the particle.

greater than would be predicted by Hamilton-Crosser. The alumina and copper oxide, respectively, enhanced the thermal conductivity by 2 times and 4 times as much as predicted by the Hamilton-Crosser equation. The copper in oil enhancements were similar in magnitude but were achieved with approximately 1/100th the volume fraction. 43% enhancement with 0.053 vol.% copper was reported. These results generated much interest within the research community given the large enhancements at low volume fractions.

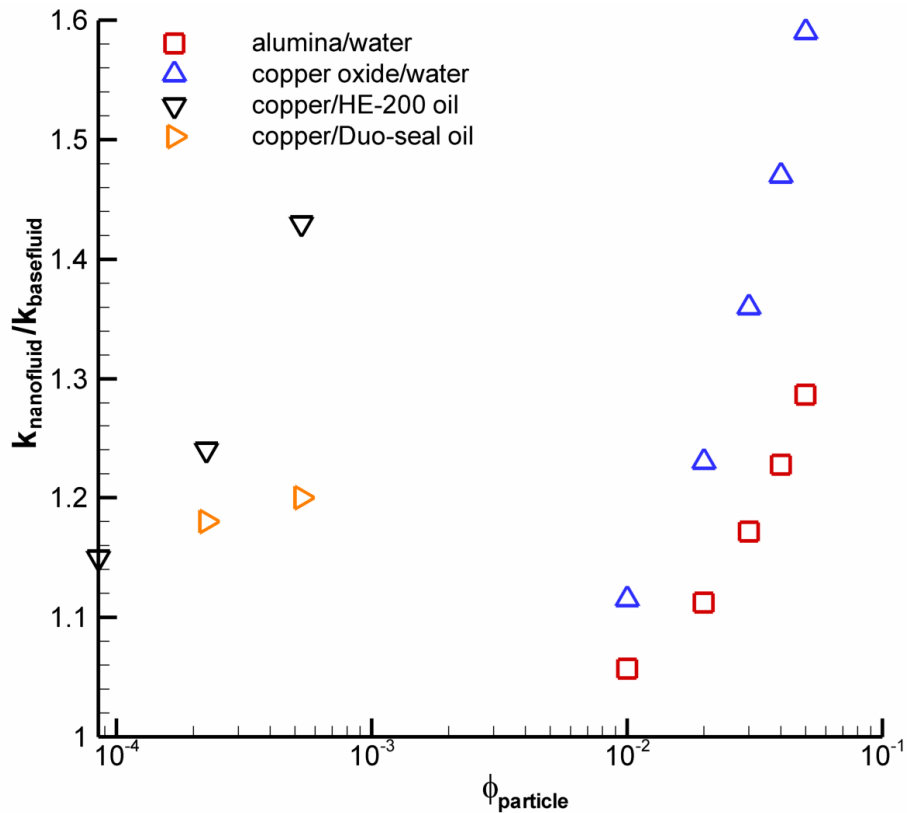


Fig. 5. Thermal conductivity enhancements for various nanofluids (based on Eastman et al., 1997).

Eastman et al. (2001) measured the enhancement provided by copper nanoparticles in ethylene glycol, which improved the thermal conductivity by up to 40% with as little as 0.3 vol.%. This improvement was also larger than observed with CuO or

Al₂O₃ nanoparticles. They also found a slight sensitivity to sample age and were able to significantly improve performance by adding thioglycolic acid as a stabilizing agent. In another impressive study, Choi et al. (2001) investigated oil with suspended carbon nanotubes, which had very high aspect ratios (~2000) and thermal conductivity (~2000 W/m·K). They found 160% enhancement with 1 vol.% of nanoparticles. They attributed the anomalous improvement to layering or some other form of organization at the solid/liquid interface.

Considering only the effect of the particle's thermal conductivity one would be driven toward high thermal conductivity materials such as diamond ($k=2000$ W/m·K). Wang et al. (2002) tested the following nanofluids: diamond, Al₂O₃, and ZnO in oils and ethylene glycol. Diamond suffered from poor suspendability and would not form a stable suspension in transformer oil. They observed ~9% enhancement with diamond in typical transformer oil, ~2% in ethylene glycol, but ~48% with a soy-based transformer oil. Clearly, surface chemistry and suspension properties determine the enhancement more than particle thermal conductivity. Wang et al. also reported enhancements ~12-20% for metal oxides (Al₂O₃, CeO₂, TiO₂, CuO, Fe₂O₃, and ZnO) in ethylene glycol for volume fractions of 4%. They attributed part of the enhancement to the Brownian motion of the nanoparticles.

While there have been many other studies reporting thermal conductivity enhancement (Wang et al., 1999; Chon et al. 2005; Yang et al. 2005; Ding et al., 2006; Murshed et al., 2005; Murshed et al., 2006; Putnam et al., 2006; Han et al., 2007), there exists no accepted theory to explain the experimental results. Uncovering the details behind the thermal conductivity enhancement is beyond the scope of this thesis. This

work instead has focused on two-phase heat transfer and the unique properties of two-phase systems using nanofluids.

2.3.2. Boiling of Nanofluids

Given the enhancement in thermal conductivity that has been observed, it was natural to consider using nanofluid in a boiling heat transfer system. Boiling has been studied for many years because of the high heat transfer rates that can be achieved at low temperature difference. However, it remains poorly understood due to the many parameters that affect the thermal performance. In particular, there is still no accepted and verified model of the CHF phenomena. This lack of understanding of the mechanisms responsible presents a significant challenge to modern research efforts aimed at enhancing CHF. Furthermore, the lack of verified boiling models presents a specific challenge to the interpretation of the numerous conflicting nanofluid boiling studies reported to date.

While the term “nanofluid” is new, nucleate boiling of nanoparticle suspensions is not. Over 20 years ago, Yang and Maa (1984) studied nucleate pool boiling with suspensions of alumina micro or nanoparticles. It is interesting to note that they did not call their suspension a “nanofluid” or even measure their particles in nanometers. They studied “0.05, 0.3, and 1.0 μm ” powders. They observed that the heat transfer coefficient increased with the addition of particles, both micro and nano. The only possible mechanism for enhancement cited though was a disturbance of the thermal boundary layer by the motion of the particles.

More recent studies regarding nanofluid boiling has yielded contradictory results. Das et al. (2003) studied boiling of alumina-water nanofluids on a 20 mm diameter

cartridge heater. They studied suspensions with alumina volume concentrations from 0.1% – 4%. The boiling curve was found to shift to the right as the nanoparticle concentration was increased, meaning higher wall temperature for the same heat flux. They showed that the nanofluid exhibited a significant viscosity increase along with its thermal conductivity increase. However, they suggested that the deterioration in heat transfer coefficient was due to a change in surface characteristics due to particles trapped on the surface.

A group at the University of Texas, Arlington (You et al., 2003; Kim et al., 2004a; Moreno et al., 2005) used water with various Al_2O_3 particle loadings in a flat plate nucleate pool boiling system. They found little to no change in the heat transfer coefficient but found dramatic improvement in CHF (see Fig. 6). You et al. (2003) followed up their flat plate measurements with photographs of the same nanofluid but this time boiling off a 390 μm diameter platinum wire. CHF was enhanced by 160% for 0.025 g/L particle loading. Surprisingly, bubbles grew much larger in the nanofluid system and had a lower departure frequency. Moreno et al. (2005) increased the types of nanofluids studied by including ZnO/water and Al_2O_3 /water+ethylene glycol. All were found to increase CHF, but high concentrations were also sometimes responsible for nucleate boiling degradation. Additionally, they found no significant dependence on particle size in the alumina/water data. Furthermore, the water/ethylene glycol based nanofluid showed linearly decreasing enhancement as the volume fraction of ethylene glycol was increased.

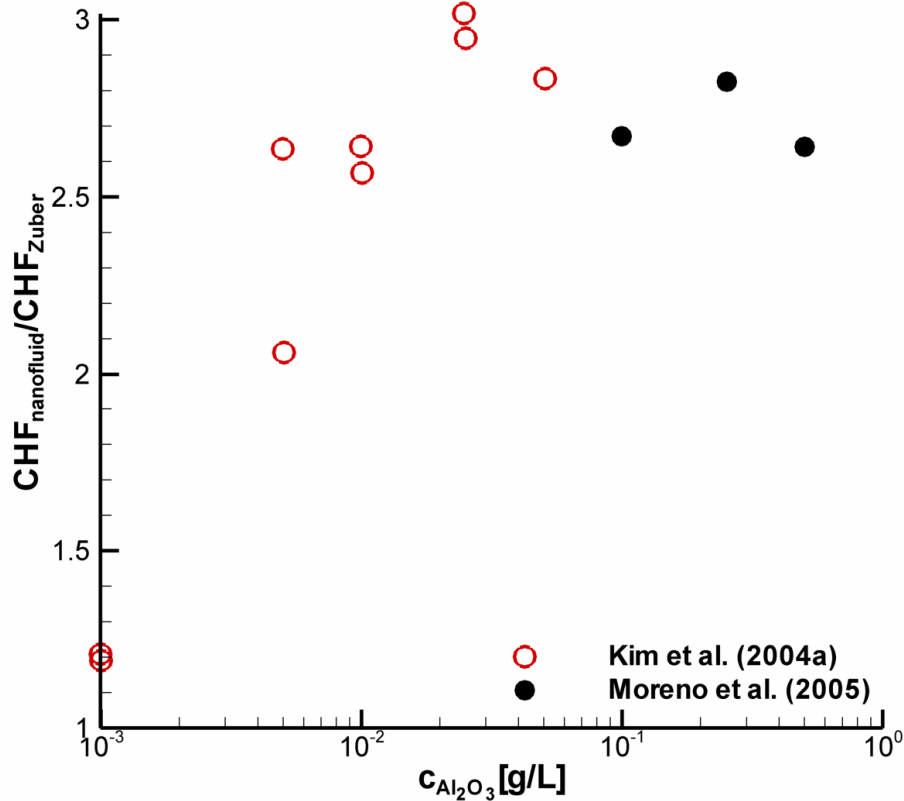


Fig. 6. CHF enhancement for alumina/water nanofluids (based on Moreno et al., 2005).

Vassalo et al. (2004) also studied pool boiling with 0.5 vol.% micro and nano-solutions. They used 15 nm, 50 nm, and 3 μ m silica particles in water on a 0.4 mm diameter NiCr wire. All suspensions were observed to increase CHF by ~60%, but the nucleate boiling regime was unaffected. However, the nanofluids had another interesting effect in that they allowed the wire to continue into the transition and film boiling modes. The pure fluid and micro-suspension resulted in wire failure immediately following CHF, while the nanofluids resulted in heat fluxes almost 3 times that of pure water, albeit at 1000 °C. The authors observed that this may be due to silica coating the wire.

Bang and Chang (2005) investigated boiling of alumina-water nanofluids on smooth, horizontal flat heaters. They observed a degradation in the heat transfer coefficient in the natural convection and nucleate boiling regimes. CHF was enhanced by

51% with the heater in the horizontal configuration (1 vol.%), and 13% in the vertical configuration (0.5 vol.% - 4 vol.%). They attributed the change in CHF to deposition of the nanoparticles onto the surface and the following two effects. First, nucleation site density is changed as the surface is smoothed (at least locally). Second, the particle deposition causes a fouling effect resulting in poor conduction heat transfer at the surface.

The work of Das et al. (2003) and Bang and Chang (2005) was contradicted by the work of Wen and Ding (2005) who used alumina/water nanofluids and observed improved nucleate boiling heat transfer. The enhancement was up to ~40% at 1.25 wt.%. They attributed the contradiction to the stability of their nanofluids. They did not observe particle deposition on the surface, and they prepared their suspension without the use of surfactants that are known to affect the boiling process.

Xue et al. (2006) used carbon nanotubes/water in a closed loop thermospyhon and found that the suspension decreased boiling performance and increased the total thermal resistance of the system. The surface tension of the suspension was found to increase compared to water, which would have an effect opposite to that of adding a surfactant. The increase in surface tension would be manifested in larger bubbles with decreased departure frequency. This is consistent with the visual observations of You et al. (2003), although the heat transfer result is opposite. Xue et al. went further by measuring the contact angle of sessile drops. Interestingly, the nanofluids had much smaller contact angles. This should improve boiling heat transfer (Liaw & Dhir, 1989; Kandlikar, 2001), but this decreased contact angle was accompanied by a increase in contact line hysteresis and greater susceptibility to surface imperfections.

The surface wettability modification was discussed by a group at MIT (Kim et al., 2006a). They found that “nano-particle fouled” surfaces significantly improved wettability as measured by the reduction in static contact angle. They suggested that the buildup of a porous layer of nanoparticles on the heated surface during boiling improved surface wettability and promoted liquid rewetting. This they suggested could explain the enhancement in CHF observed by numerous researchers.

This mechanism was specifically probed by the Pohang University (Korea) group of Kim et al. (2006b) during their investigation of titania-water and alumina-water nanofluids on a 0.2 mm diameter NiCr wire. They used particle volume concentrations from $10^{-5}\%$ to $10^{-1}\%$ and observed CHF to increase with nanoparticle concentration. CHF was enhanced by up to 100% when nanofluids were boiled on a bare wire. Scanning electron micrograph pictures taken of the heater surface after boiling revealed that the surface was covered by nanoparticles. Interestingly, when the nanofluid was drained from the chamber and pure water was boiled on the nanoparticle coated wire, CHF was increased up to 2.75 times the baseline. This clearly demonstrated that nanofluids were increasing CHF through surface modification. Furthermore, they demonstrated that nanofluids could actually be worse than pure fluids given the appropriate surface treatment.

The literature cited above presents many contradictions with some groups reporting enhancement and other degradation. Table 4 summarizes the findings of these studies.

Table 4. Summary of nanofluid boiling studies.

Study	Particle Size [nm]	Particle Concentration	Particle Type	Base Fluid	Heater Surface	Nucleate Boiling	CHF
Yang & Maa, 1984	50, 300, 1000	1 wt. %	Al ₂ O ₃	Water	Stainless steel tube	Improved	-
Das et al., 2003	38	0.1 – 4 vol. %	Al ₂ O ₃	Water	Cylindrical cartridge heater	Degraded	-
You et al., 2003	“nanoparticles”	0.001 – 0.05 g/L	Al ₂ O ₃	Water	Cu plate, Pt wire	Unchanged	Improved
Kim et al., 2004a	32	0.001 – 0.05 g/L	Al ₂ O ₃	Water	Cu plate, Pt wire	Unchanged	Improved
Vassalo et al., 2004	15, 50, 3000	0.5 vol. %	SiO ₂	Water	NiCr wire	Unchanged	Improved
Bang & Chang, 2005	47	0.5 – 4 vol. %	Al ₂ O ₃	Water	Horizontal & vertical planes	Degraded	Improved
Wen & Ding, 2005	168	0.32 – 1.25wt. %	Al ₂ O ₃	Water	Stainless steel plate	Improved	-
Moreno et al., 2005	69, 139, 224, 346 (Al ₂ O ₃) 24 – 71 (ZnO)	0.1 – 0.5 g/L (Al ₂ O ₃) 0.001 – 0.5 g/L (ZnO)	Al ₂ O ₃ ZnO	Water, Water/Ethylene Glycol	Cu plate	Unchanged or Degraded	Improved
Xue et al., 2006	15 x 10,000	1 vol. %	CNT	Water	Cu thermosyphon	Degraded	-
Kim et al., 2006b	“nanoparticles”	0.00001 – 0.1 vol %	Al ₂ O ₃ TiO ₂	Water	NiCr wire	-	Improved (Pure water also improved CHF on nanofouled surface)

2.4. Extended Structures

Surface enhancement in the form of surface roughening, pore creation, or extended surfaces has long been known to be an effective way of increasing thermal performance of nucleate boiling systems. Kurihara and Myers (1960) showed that roughening of the surface resulted in increased nucleation site density, which results in greater bubble agitation and increased latent heat transport. Others have extended this technique by creating porous structures on the heater surface. Nakayama et al. (1980, 1982) created interconnected internal cavities consisting of microscale tunnels and pores. Using R-11, water, and nitrogen they found that 80 – 90% less wall superheat was required to transfer the same heat load due to liquid being sucked into the surface and subsequent evaporation inside the tunnel. This technique of providing interconnected pores was extended by adding stacked layers of microporous structures to form an extended surface (Nakayama et al., 1984; Ramaswamy et al., 2003), which increases the total heat transfer by increasing the area available. This is an effective method of improving performance for electronics applications, since large heat loads (over 100 W with FC-72) are removed from the small projected area of the chip. Mudawar and Anderson (1993) studied more fin-like extended surfaces using microgrooves, square microstuds, and pin fin arrays. These structures improved the total heat transfer up to 159 W/cm^2 on a projected area basis compared to $\sim 20 \text{ W/cm}^2$ with a bare surface.

Spray cooling an extended surface might also dramatically improve thermal performance, however the analysis will be further complicated. Add to the inherent complexity of an extended surface with nucleate boiling the addition of radially and axially varying mass flux, droplet size and velocity distribution, shading of parts of the

surface from impinging drops, liquid pooling in parts the structure, capillary effects, splashing, hot vapor condensing on incoming droplets, thin film evaporation, mixing and possible secondary nucleation caused by incoming drops. Furthermore, with all of these phenomena in concert, the system is likely to exhibit different boiling regimes on different parts of the heater. Despite the daunting complexity, spray cooling of extended surfaces has garnered some attention.

Sodtke and Stephan (2005) used water to spray cool a porous surface as well as ones with triangular microgrooves and micro pyramids (width = pitch = $150\mu\text{m}$, height = $75\mu\text{m}$). They found no improvement with the microporous structure. However, with microgrooves and micro pyramids they observed a 2 – 5 fold enhancement when the superheat exceeded $6\text{ }^\circ\text{C}$ and no enhancement at lower superheats. They posited that the higher superheat ruptures the liquid film, allowing capillary forces to distribute a thin film equally between the fin troughs and tips.

Other investigations have shown the potential of extended surfaces to transfer as much as 50% more heat than comparable flat surfaces. Silk et al. (2004, 2005, 2006) investigated spraying gassy (1 atm) PF-5060 on a flat surface and enhanced surfaces including straight fins, square pin fins, and pyramidal fins. All of their enhanced surfaces improved performance in the nucleate boiling regime and significantly increased the critical heat flux. Surprisingly, they also found that straight fins outperformed the other two types of surface enhancements, despite the fact that the straight and pin fins had the same areas and the straight fins would have a larger conduction resistance. In fact, the pyramidal fins showed the worst performance despite being designed to account for the conduction resistance. This lead the authors to speculate that the enhancement was due

to channeling of the liquid into the space between the fins, resulting in much higher CHF. Silk et al. (2006) noted that since the fin width and pitch were held constant, the pin fins had twice the drainage area of the straight fins, which results in half the liquid velocity. This higher velocity with the straight fins could have resulted in a higher heat transfer coefficient in the channels.

CHAPTER 3. EXPERIMENTAL SETUP AND METHODOLOGY

Numerous experiments were designed and constructed to study nanofluids and extended surfaces. In particular, the nanofluid studies required multiple experimental setups as the effect of liquid/surface interaction in pool boiling was investigated. The various experimental apparatuses, procedures, and methodologies used in these studies are described below.

3.1. Nanofluids Boiling and Spray Cooling Setups

The experimental investigation of nanofluids boiling and spray cooling required the use of various heated surfaces. Two basic heater assemblies were used: a thick-film resistive heater and a copper block heater. These experiments shared a common chamber and much of the associated instrumentation but required different data acquisition and control. The common elements are discussed below, while the unique elements of the two different systems are discussed later in their own sub-sections.

3.1.1. Nanofluids Test Rig

The stainless steel boiling and spray chamber is shown in Fig. 7. The rig consisted of two 20.3 cm (8 in.) diameter ConFlat® flanges. The upper flange (33.3 cm long full nipple) housed a copper condensing coil. The lower flange (4-way reducing cross) housed the boiling surface (not visible). The four ports of the bottom flange allowed for two view ports, connection to the upper flange, and a bottom port that facilitated the insertion of various test surfaces.

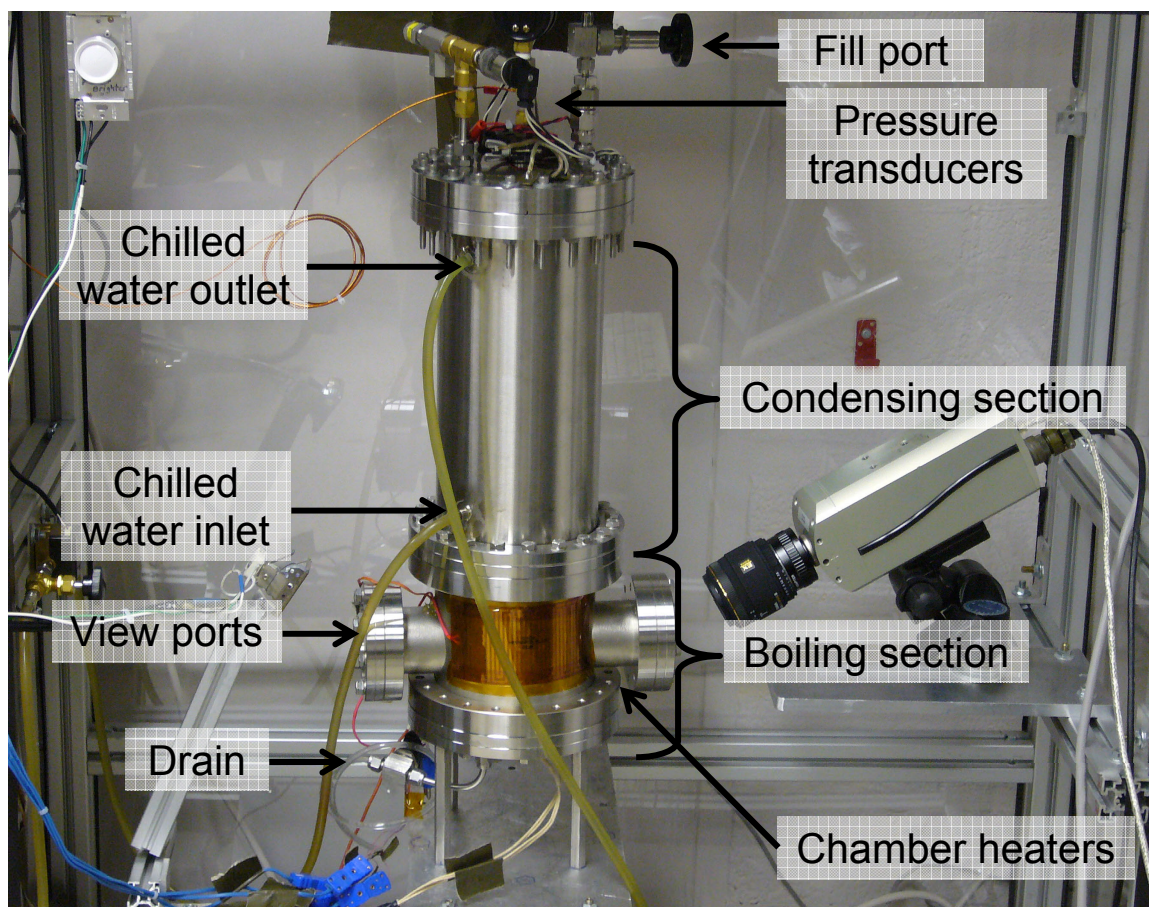


Fig. 7. Test rig.

The copper condensing coil (6.35 mm OD, 4.4 mm ID, ~7.5 m long) was cooled by chilled (15 ± 0.2 °C) water provided by a constant temperature bath (NESLAB RTE17). The 475 ± 11 mL/min flow of the chilled water was measured with a turbine flow meter (Omega FLR1009BR). Chamber pressure was measured using a 0 – 2 atm thin-film pressure transducer (Omega PX212-030AV). Chamber temperature was measured with a Type K thermocouple probe. The chamber temperature was controlled by a proportional integral derivative (PID) temperature controller along with Kapton surface heaters that were attached to the outside walls of the lower flange.

Boiling movies were recorded with a high speed digital camera (Vision Research Phantom V4) capable of 512 x 512 pixel resolution at 1000 frames per second. A Sigma 50 mm macro lens was used, and light was provided by a 300 W projection lamp.

3.1.2. Thick-film Resistive Heater

The first heater assembly (Fig. 8) used for nanofluid boiling and spray cooling was based on a thick-film resistor. An 18 Ω ruthenium-based thick-film resistor on an alumina substrate was obtained from Mini-systems, Inc. The heater was fixed to the G-10 substrate using electronic grade silicone (GE RTV162). The average surface temperature was measured with a surface mount, platinum resistance temperature detector (RTD) (Omega Engineering SRTD-2) that was bonded with heat sink compound to the backside of the heater. To ensure good thermal contact between the heater and the RTD, the heater was pressed against the RTD by aluminum plates (with silicone sealant between to insulate the heater). This assembly was then placed on a two-axis traverse that was mounted to the bottom flange of the chamber.

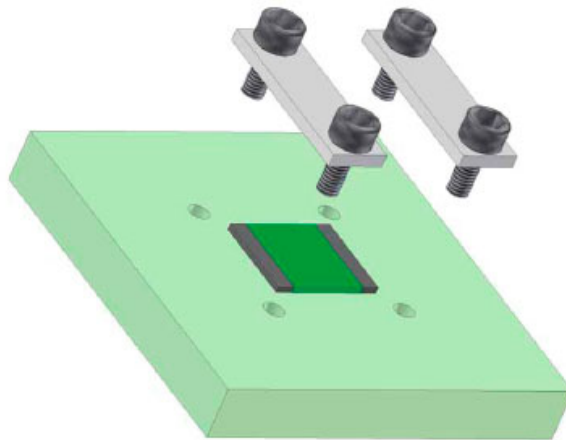


Fig. 8. Thick-film resistor assembly (Courtesy of Alexander Walzenbach).

The thick-film heater was supplied with a glass topcoat. The bond pads of the resistor were covered with a layer of silicone to prevent boiling and maintain a uniform boiling surface at the center of the resistor. With only the glass exposed, the surface area was $0.93 \pm 0.02 \text{ cm}^2$. This heater was subsequently coated with 100 nm of gold through an evaporative physical vapor deposition process. The gold surface decreased the surface energy of the boiling surface, which was done as the first step in the study of surface wettability effects.

The data acquisition (DAQ) and control of the thick-film resistor experiments are shown schematically in Fig. 9. A Fluke Hydra Data Acquisition Unit logged data from all thermocouples as well as recorded the flow rate of the spray, chamber pressure, RTD resistance, and heater supply voltage. Data was then transferred through a general programming interface bus (GPIB) data link (ICS Electronics 488-USB) to a laptop computer. A custom MATLAB program (*DAQ_menu2.m*) was developed to save the results and chart the data as it was acquired (see Appendix B).

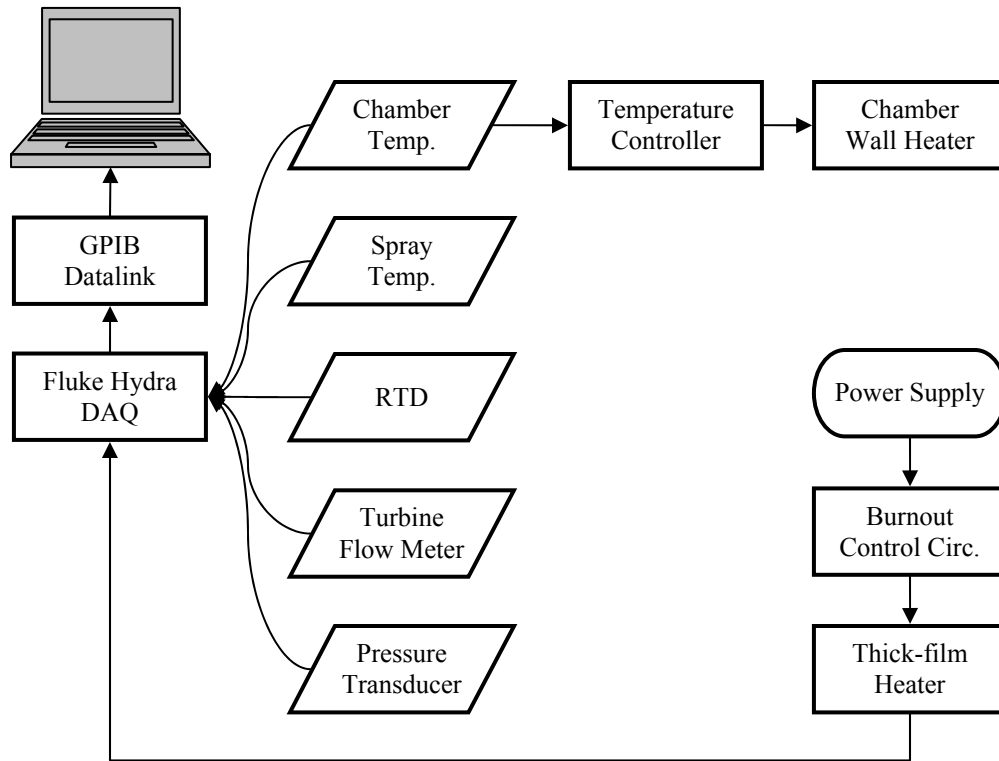


Fig. 9. Data acquisition and control diagram for thick-film resistor heater.

An important component of the DAQ/control system was the burnout control circuit (Fig. 10). The small mass (0.4 g) of the alumina substrate resistor would have made the resistor highly susceptible to burnout post CHF. A Wheatstone bridge circuit (Fig. 11) was designed to prevent burnout of the heater post CHF by cutting off power. The theory behind the circuit's operation is as follows. At room temperature, the heater resistance was nominally 18 Ω . However, as the heater increased in temperature, its resistance increased according to Eq. 29:

$$R(T) = R_0(1 + \alpha\Delta T) \quad , \quad (29)$$

where α is the linear temperature coefficient of resistance. When the heater resistance reached $\sim 18.3 \Omega$ the bridge became balanced. At this point, the comparator (LTC1150)

sensed the balancing of the bridge and output a signal to open two redundant mechanical relays (Struthers Dunn 219BBX-P), cutting off power to the heater.



Fig. 10. Wheatstone bridge circuit to prevent burnout of the thick-film resistor.

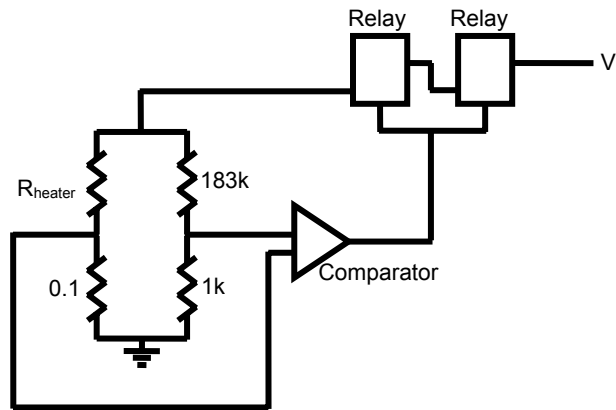


Fig. 11. Wheatstone bridge circuit schematic.

3.1.3. Copper Block Heater

For the experiments using a copper or copper oxide surface, heat was provided by two 250 W cartridge heaters embedded within an oxygen free high conductivity (OFHC) copper heating block (Fig. 12). This block was then inserted through a stainless steel plate, which was sealed by two #16 Viton o-rings. The stainless plate was then bolted to the bottom flange of the boiling chamber and sealed with a 1.6 mm (1/16th inch) neoprene

flat gasket. The heater block featured a neck with a circular cross-section that terminated with a polished surface on which the boiling occurred. The neck of the heating block contained holes (1 mm diameter, 1 cm deep) for four thermocouples spaced 1 cm apart along its length.

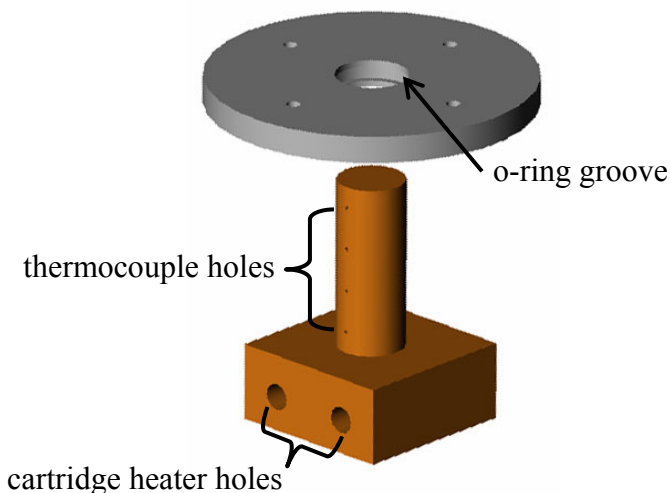


Fig. 12. Copper heating block and stainless steel sealing plate.

The horizontal boiling surface was 2 cm² and was polished using emery paper up to 1200 grit, which provided a mirror-like finish. However, a thin region above the o-rings and around the perimeter was also wetted, which increased the total wetted area to 2.7 cm². Baseline, unoxidized, surfaces were created by using a cotton swab to wipe the surface with dilute nitric acid (1 M HNO₃), which removed the oxidation[†]. Various levels of surface oxidation were then systematically created by heating the copper heating block in air.

To oxidize the surface, the copper block was separated from the stainless steel sealing plate and instrumented with thermocouples and cartridge heaters. This assembly

[†] Dilute nitric acid reacts with copper oxide according to the following balanced chemical equation: $\text{CuO} + 2\text{HNO}_3 \rightarrow \text{Cu}(\text{NO}_3)_2 + \text{H}_2\text{O}$. This reaction reduces the oxide and renders the copper into the aqueous solution. Note that elemental copper reacts similarly with dilute nitric acid: $3\text{Cu} + 8\text{HNO}_3 \rightarrow 3\text{Cu}(\text{NO}_3)_2 + 2\text{NO} + 4\text{H}_2\text{O}$ (Battey et al., 1988).

was then placed on fiberglass insulation. The ramp function of a PID controller was then used to linearly increase the temperature of the block from room temperature to the desired temperature at a rate of 5 K/min. Dwell times of 32 to 132 minutes were used to get the desired oxidation (see Table 5), then the power was cut off and the block was allowed to cool through free convection. The temperature of the block was recorded approximately every 6 seconds by a Fluke Hydra Data Acquisition Unit. A typical temperature history is shown Fig. 13. This oxidation process produced surfaces with similar microstructure yet variable contact angle (the contact angle measurements are described later in this chapter).

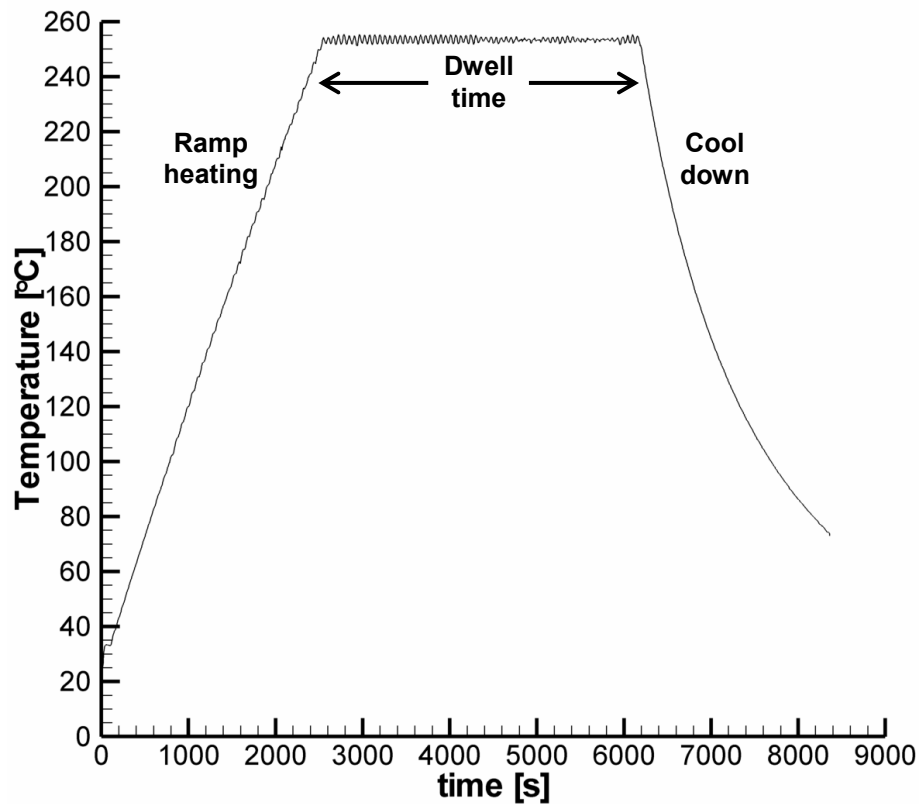


Fig. 13. Typical temperature history of the copper block during the oxidation process.

Table 5. Oxidation parameters used to increase the surface energy.

Relative Degree of Oxidation	T_{peak} [°C]	t_{dwell} [min]
Light	200	33
Medium/light	234	32
Medium	253	61
Heavy	281	132

The data acquisition and control used for the copper block heater experiments are shown schematically in Fig. 14. The cartridge heaters within the copper heating block were powered with a variable voltage level set by the operator and regulated by a variable transformer. Cutoff of power to the heaters to prevent burnout was controlled by two redundant On/Off temperature controllers with temperature input from the two thermocouples that were farthest from the heaters (i.e., nearest the boiling surface). The Fluke Hydra Data Acquisition Unit logged data from all thermocouples as well as recorded the flow through the condenser, chamber pressure, and heater supply voltage. Data was then transferred through the general programming interface bus data link to a laptop computer. A custom MATLAB program (*DAQ_menu4.m*) was developed to save the results and chart the data as it was acquired (see Appendix B).

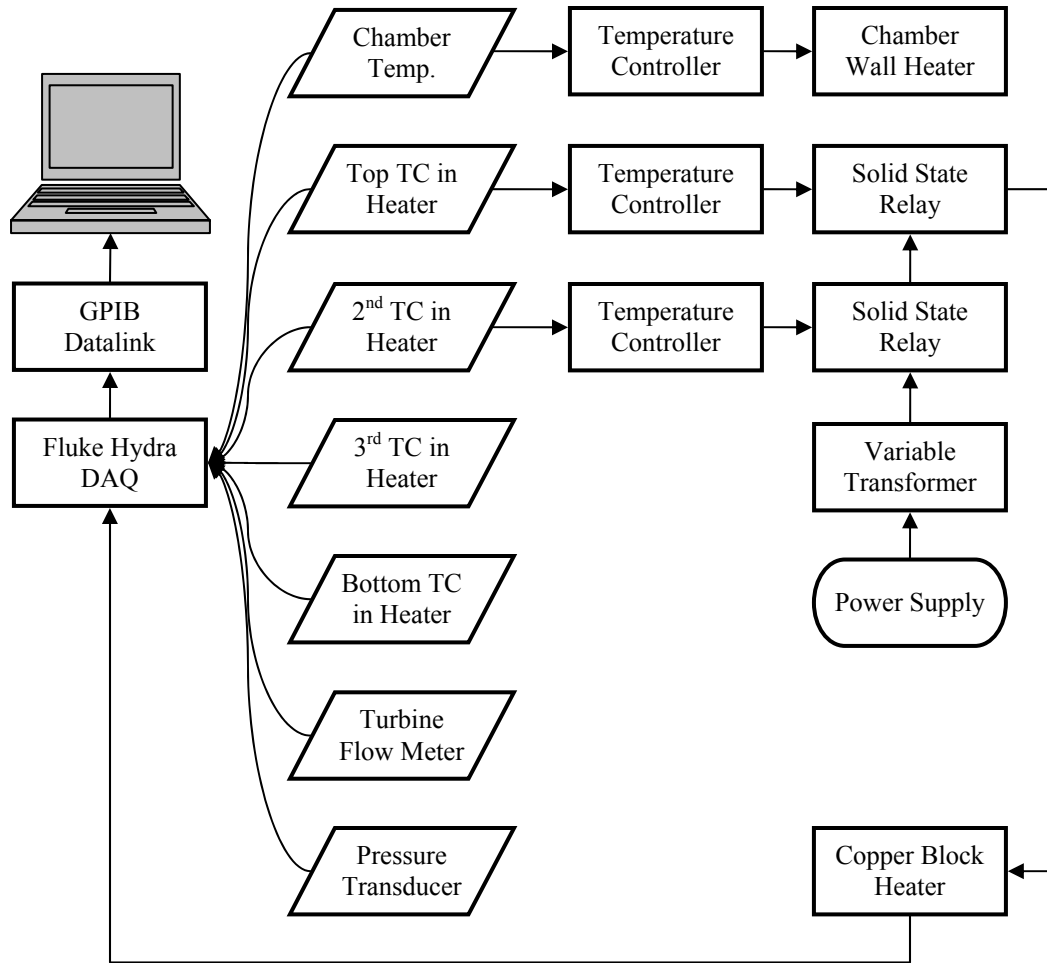


Fig. 14. Data acquisition and control diagram for copper block boiling heater.

3.1.4. Working Fluids and Nanofluid Preparation

Both ethanol and water based nanofluids were used. Although water has excellent thermal properties (Table 6), its electrical conductivity makes it unattractive for many applications. Ethanol, however, is electrically non-conductive provided it is free of water. Ethanol is also non-toxic and features relatively high thermal properties compared to other dielectrics such as FC-72. Interestingly, alcohols have not received much attention from nanofluid researchers, which have focused on water, oils, and ethylene glycol to a lesser degree. Using ethanol had the additional benefit of filling a void in the

literature concerning nanofluid boiling since nearly all studies reported have been performed with water based nanofluids.

Table 6. Thermal properties at saturation (P=101325 Pa) (* Incropera & DeWitt, 1996; ** 3M, 2000; † Dillion & Penoncello, 2003; ‡ Yaws, 1999).

Property	Water*	Ethanol	FC-72**
T _{sat} [°C]	100	78 [†]	56
Latent heat of vaporization [kJ/kg]	2257	849 [†]	88
Liquid thermal conductivity [W/m·K]	0.680	0.216 [‡]	0.054
Liquid specific heat [kJ/kg]	4.217	3.130 [†]	1.101
Liquid dynamic viscosity [N·s/m ²]	0.000279	0.000448 [‡]	0.00043
Molecular weight [g/mol]	18.02	46.07	338

Two concentrated nanofluid suspensions were obtained from Nanophase Technologies Inc.: a 30.84 wt.% alumina-in-ethanol suspension, and a 49.5 wt.% alumina-in-water suspension. The surface area average diameter and specific surface area of these particles were given by the manufacturer to be 45 nm and 35 m²/g, respectively (Nanophase Technologies Inc., 2003).

The ethanol based nanofluid was diluted to a variety of concentrations ranging from 0.001 g/L to 10.07 g/L. Figure 15 shows some of the suspensions used. The concentrated suspension provided by the manufacturer was vigorously shaken and then small samples were extracted to be added to 200 proof ethanol (99.98 vol.% ethanol, 0.02 vol.% water). Volume fraction, mass fraction, and concentration were calculated using Eqs. 30 - 32.

$$\phi_{Al_2O_3} = 1 - \left(\frac{\rho_{mix} - \rho_{Al_2O_3}}{\rho_{pure\ liquid} - \rho_{Al_2O_3}} \right) \quad (30)$$

$$y_{Al_2O_3} = \frac{\rho_{Al_2O_3}}{\rho_{mix}} \phi_{Al_2O_3} \quad (31)$$

$$c_{Al_2O_3} = \rho_{Al_2O_3} \phi_{Al_2O_3} \quad (32)$$



Fig. 15. Alumina-in-ethanol nanofluid samples (from left to right: 200 proof ethanol, 0.005 g/L, 0.01 g/L, 0.05 g/L, 0.1 g/L, 0.5 g/L, and 30.84 wt.%).

The water based nanofluids were prepared by using a pipette to extract 10 mL of the concentrated solution provided by the manufacturer. Fluid was drawn from the middle of the concentrated sample to obtain suspended particles rather than those that had coagulated and settled. The solution was then weighed to determine the density, ρ_{mix} , of the sample to be used. Then, the volume fraction, mass fraction, and concentration were calculated using Eqs. 30 - 32, respectively. This suspension was then diluted with distilled water to concentrations of 0.026 g/L to 1.02 g/L.

3.1.5. Test Conditions

Nanofluids were used in both boiling and spray cooling systems. Boiling was tested on four different surfaces with two different base working fluids at concentrations ranging across five orders of magnitude. The test matrix for nanofluid boiling is shown in Fig. 16.

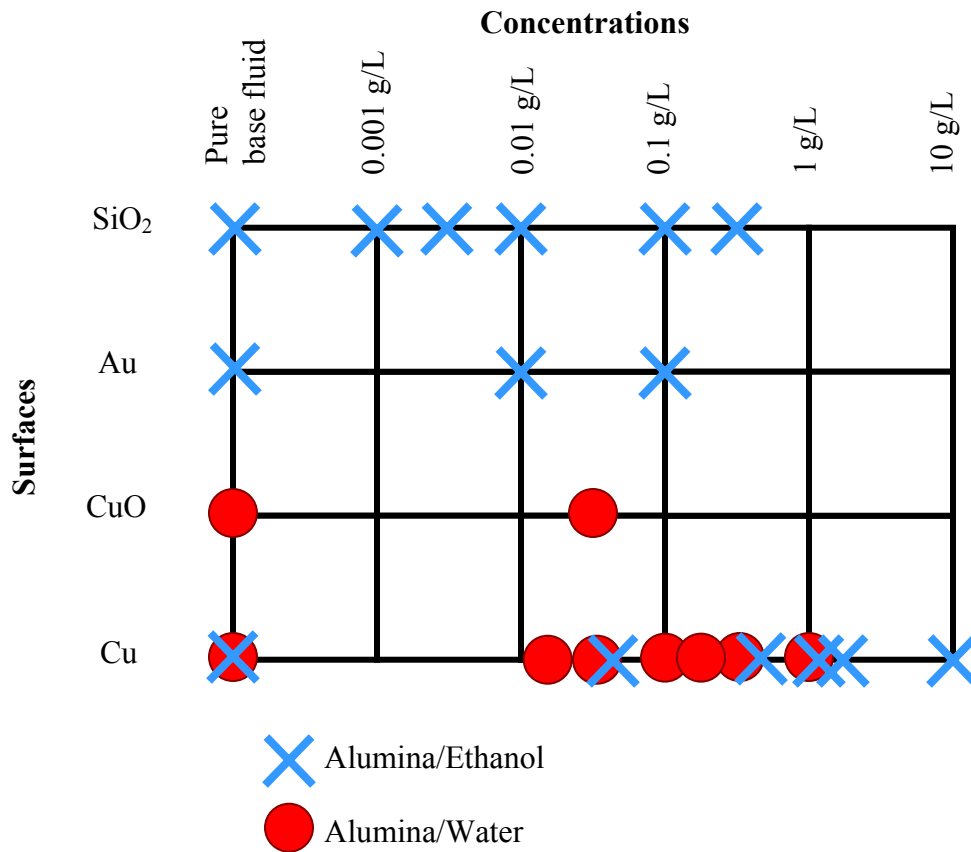


Fig. 16. Experimental test matrix for nanofluid boiling studies.

Boiling experiments were conducted with reduced pressure under saturated and subcooled conditions. The system pressure was reduced prior to each experiment by repeatedly pulling a partial vacuum on the liquid. For the subcooled experiments, dissolved gas (air) remained in the working fluid. In the thick-film heater experiments, the pool temperature was maintained at 30.6 ± 0.5 °C, while the saturation temperature was 51.7 ± 0.4 °C. With the copper block heater, the pool temperature was maintained at 28.8 ± 0.3 °C (with ethanol) or 29.3 ± 0.7 °C (with water). These experiments were run at near saturated conditions with a saturation temperature of 28.9 ± 1.0 °C (with ethanol) or 29.8 ± 0.7 °C (with water).

Spray cooling experiments were conducted at two different nozzle pressure differences and four different concentrations. With a nozzle pressure difference of 69 kPa (10 psi), the flow rate was 18 ± 1 mL/min. For a higher flow rate and better atomization, a nozzle pressure difference of 345 kPa (50 psi) was also used: the flow rate was 52 ± 1 mL/min. The nozzle-to-heater distance was 10.1 ± 0.5 mm. The saturation and spray temperature were 51.7 ± 0.4 °C and 30.5 ± 0.3 °C, respectively. In all cases, ethanol based nanofluids were used on a glass substrate. Nanofluid concentrations ranged from 0.001 g/L – 0.5 g/L.

3.2. Contact Angle Measurements

To determine the effect of surface wettability on nanofluid boiling, the contact angle needed to be quantified. As discussed in Appendix A, the advancing contact angle is much larger than the receding angle[†] and is easier to measure accurately. Both angles are also affected by the liquid's affinity for the solid surface, and, therefore, only the advancing contact angle was measured in the present work as an indication of the wettability of the surface. An advancing contact angle was created by dispensing liquid onto a horizontal surface. A screw driven syringe pump (Harvard Apparatus PHD 2000) was used to infuse liquid onto the surface at a constant rate resulting in a gradually growing liquid droplet. The infusion pump setup is shown schematically in Fig. 17. Liquid was delivered at a rate of 0.125 mL/min through a 305 μ m ID microneedle. The measurements were made in an open environment and at room temperature.

[†] In one case, the receding angle for water on copper was measured to be $\sim 10^\circ - 20^\circ$ compared to the advancing angle of $\sim 90^\circ$.

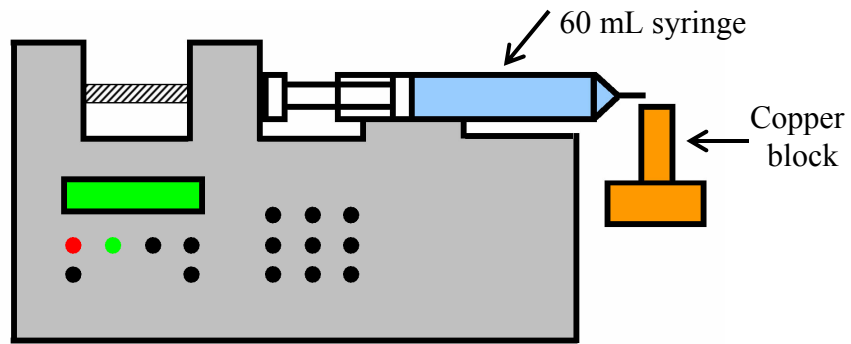


Fig. 17. Infusion pump setup.

Two different photographic techniques were used to record the advancing droplet. A series of high resolution (3008 x 2000 pixels) digital still photographs were captured by a Nikon D50 camera with a Sigma 50 mm macro lens. Photographs were taken with a shutter speed of $1/5^{\text{th}}$ of a second, allowing the aperture to be minimized and the depth of field to be maximized. Using delayed shutter release (2 s), camera shake was minimized and the resulting photographs were sufficiently sharp for image analysis. A typical photograph is shown in Fig. 18. Movies were also recorded using a digital video camera (Vision Research Phantom V4) and the above lens.

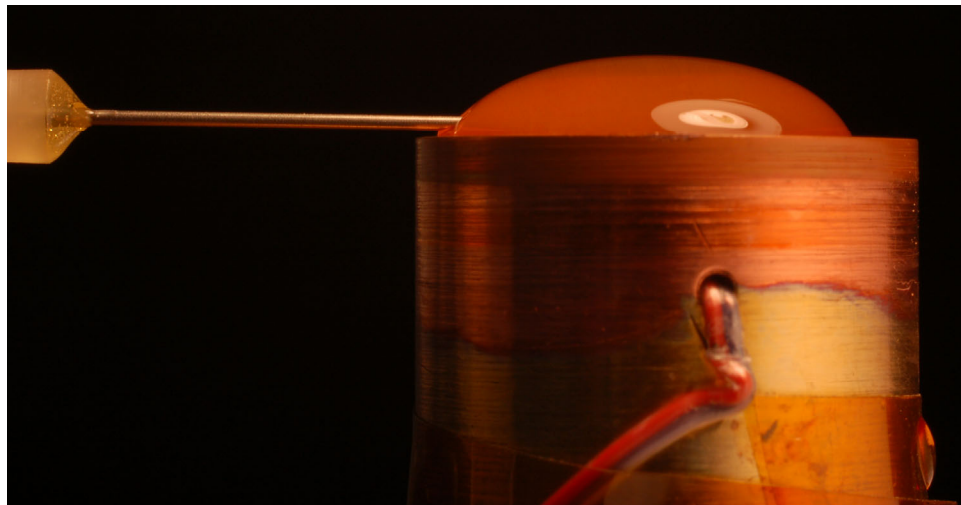


Fig. 18. Advancing water droplet on a copper surface.

3.2.1. Contact Angle Measurement Algorithm

Contact angles were then measured from the digital still photographs using the following algorithm implemented in MATLAB (see Appendix B):

1. Convert the image to grayscale.
2. Perform edge detection using the Canny (1986) method, which finds local maxima in the gradient of the image.
3. Choose six points along the droplet/air interface and one on the horizontal heater surface.
4. Fit an ellipse through the points on the droplet/air interface using the Halif and Flusser (1998) method.
5. Calculate the tangent at the intersection between this ellipse and the horizontal.
6. Determine the contact angle from the inverse tangent.

Fig. 19 illustrates the edges of the image detected using the above algorithm. After zooming in on the digital image, points were selected along the interface and the curve fitting was performed. The resulting curve fit and tangent determination that followed are shown in Fig. 20.

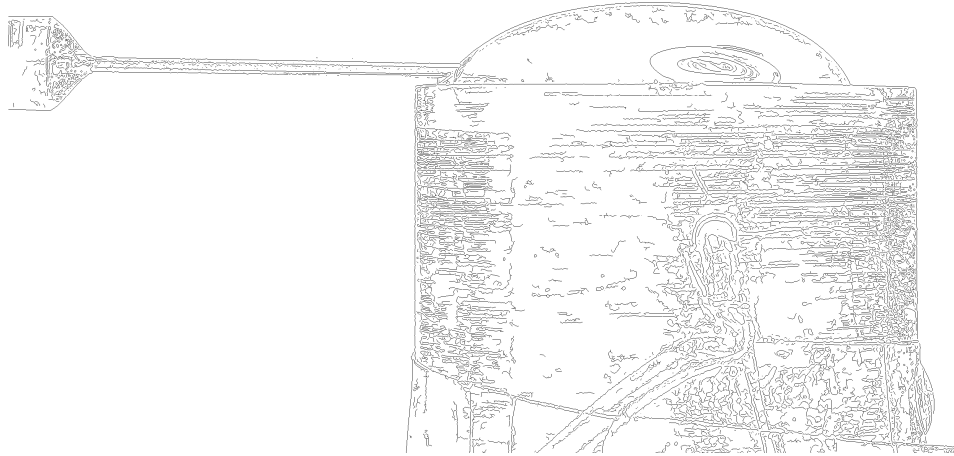


Fig. 19. Results of edge detection on the image of an advancing water droplet.

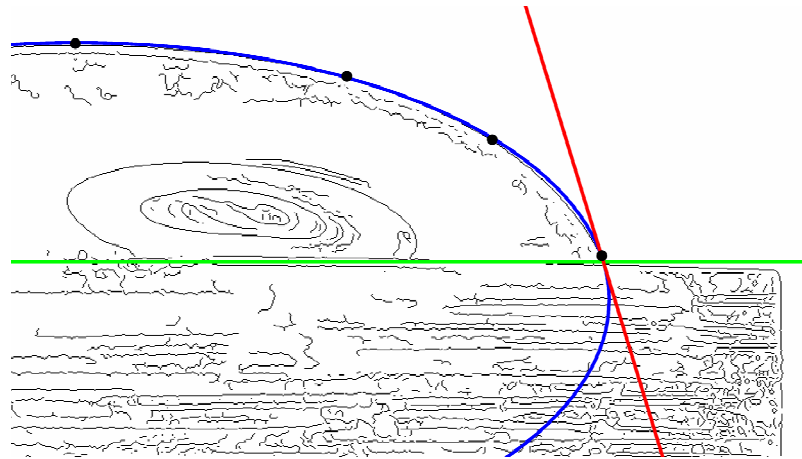


Fig. 20. Curve fitting results (the two other points on the interface are on the other side of the droplet).

3.3. High Aspect Ratio Open Microchannel Spray Cooling Experiments

To elucidate the mechanisms behind spray cooling extended structures, a series of experiments involving high aspect ratio open microchannels was performed. The experimental apparatus, data acquisition and control, as well as the test conditions used are described below.

3.3.1. Test Rig

A schematic diagram of the experimental setup and flow loop is shown in Fig. 21. A spray chamber was formed by attaching polycarbonate discs to a large diameter acrylic tube. The top plate included feedthroughs for the nozzle and a condensing coil. A brass spray nozzle from Isothermal Systems Research (ISR) was insulated with 5 mm of neoprene to minimize temperature increases due to vapor condensation on the nozzle housing. The copper coil (with 30°C water flowing inside) provided the primary condensation location. The chamber base featured a drain and another opening which allowed the insertion of the test surfaces. Each test surface was surrounded by ceramic insulation (OD=10 cm, 6 mm thick, Cotronics 914 machinable glass ceramic), which was sealed to the chamber base with a neoprene o-ring.

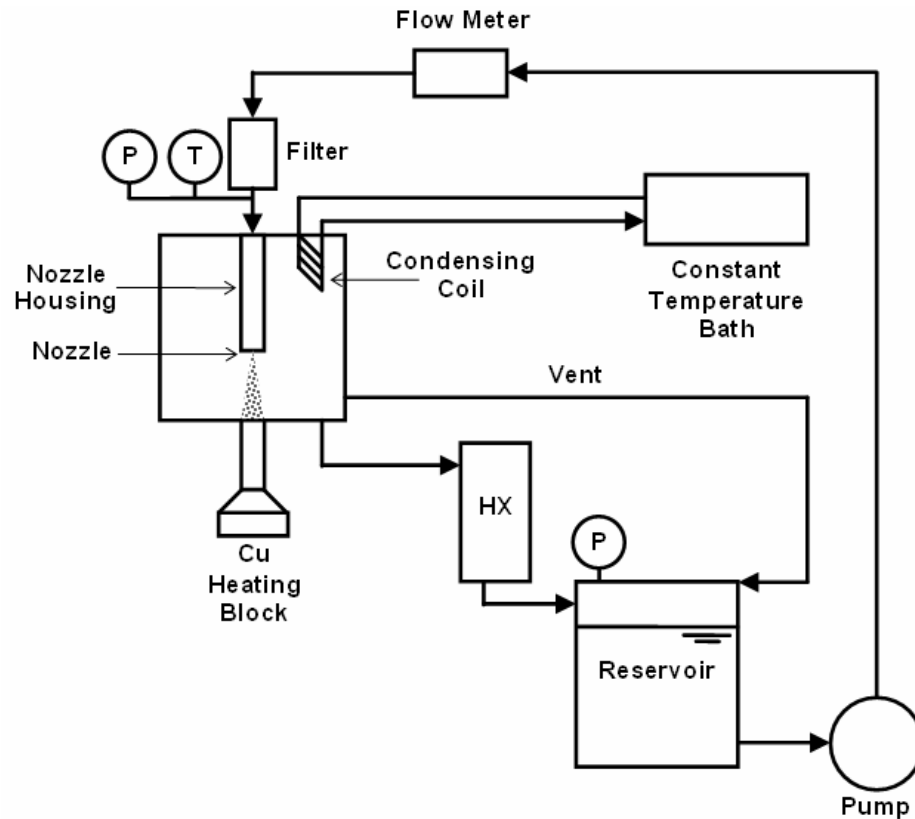


Fig. 21. Experimental setup for microchannel spray cooling.

3.3.2. Heater Assembly

Heat was provided by two 250 W cartridge heaters (0.635 cm OD, 3.8 cm long) embedded within an OFHC copper heating block. The top of the heating block featured a female threaded hole into which different heating necks could be screwed (see Fig. 22). The necks were surrounded by air, which provided sufficient insulation to effectively create a one-dimensional heat flux along their axes. This was verified by the measurement of a linear temperature gradient along their length. This heat flux and the wall temperature were measured with a sheathed thermocouple probe (type K) that was dry-fit into each of four close-fit holes (1.2 mm-diameter, 7.1 mm deep, 10 mm separation) located in the heating necks. Heat losses from the thermocouple probes were negligible due to the small diameter and low thermal conductivity of the probe[†]. Heat losses from the neck in the instrumented region were also negligible, as indicated by the good agreement between the electric power input (after accounting for losses from the base) and the heat flux calculated using one-dimensional conduction through the neck of the heater—see Chapter 4 for further details.

[†] A 1-D finite difference fin analysis of the thermocouple probe was performed in which the free convection from the probe was modeled using Morgan's (1975) long horizontal cylinder correlation. For a heat flux of 100 W/cm^2 and wall temperature of $87.5 \text{ }^\circ\text{C}$, the heat loss due to the probes was found to be $\sim 0.25\%$ of the 1-D heat flux attributed to the spray.

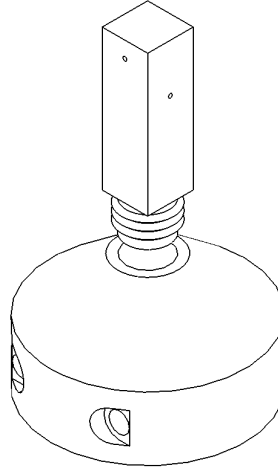


Fig. 22. Heating block assembly (Courtesy of William Michie).

Six different heaters with $1.41 \times 1.41 \text{ cm}^2$ profiles were used. Square rather than circular profiles were used to better simulate the cooling of an electronic device. One heater featured a simple flat surface for baseline comparisons. Five heaters featured electric discharge machined (EDM) straight fins with a channel width (C) of $360 \text{ }\mu\text{m}$; fin width (W) of $500 \text{ }\mu\text{m}$; and fins lengths (L) of 0.25 mm , 0.50 mm , 1.0 mm , 3.0 mm , and 5.0 mm (see Table 7 and Fig. 23). These heaters were then bonded to the ceramic insulation described above using an electronic grade silicone (GE RTV162).

Table 7. Channel aspect ratio and surface areas of test surfaces.

Fin Length (L) [mm]	Channel Aspect Ratio (L/C)	Total Surface Area [mm^2]	Area Enhancement
0	-	200	1
0.25	0.7	320	1.6
0.5	1.4	440	2.2
1	2.8	681	3.4
3	8.3	1642	8.2
5	13.9	2604	13



Fig. 23. Heater necks with 5 mm (left) and 1 mm (right) long fins.

3.3.3. Working Fluid and Spray Characteristics

PF-5060 (3M performance fluid composed of perfluoro compounds with primarily 6 carbons) was chosen as the working fluid because its chemical stability and dielectric nature make it suitable for direct cooling of electronics. Furthermore, its boiling point of 56°C at 1 atm is low enough to allow for two-phase cooling at a temperature that is appropriate for high reliability electronics. Note that PF-5060 is essentially a less pure (and less costly) form of 3M's FC-72. According to their datasheets, their thermal properties are the same (3M, 2000 & 2003).

Flow was provided by a magnetically coupled gear pump (Cole Palmer 75211-10), and the flow rate through the nozzle was measured with a digital turbine flow meter (Omega FLR1000BR). The working fluid was filtered using a 2 μm borosilicate glass filter. The pressure immediately upstream of the nozzle housing was measured with a Bourdon tube gauge (Omega PGS-25L-160). The chamber pressure was maintained at one atmosphere through use of a vent on the fluid reservoir. The fluid was not degassed

and had a dissolved gas concentration that was estimated using Henry's Law for ideal solutions:

$$c_{gas} = H(P_T - P_{sat}) \quad , \quad (33)$$

where H is Henry's constant, $0.005438 \text{ atm}^{-1}$ for FC-72 (You, 1990). With Eq. 33, the gas concentration, c_{gas} , was estimated to be 3420 ppm. Nozzle pressure differences ranged from 138 kPa – 413 kPa (20 – 60 psig).

The upstream spray temperature was measured with a type T thermocouple inside the nozzle housing body. The temperature directly upstream of the nozzle was $30.4 \pm 0.9^\circ\text{C}$. The temperature of the droplets actually striking the heater was measured with four separate downstream thermocouples (OD=500 μm) that were placed within and around the spray cone. Repeated trials indicated that the addition of the downstream thermocouples had a negligible impact on thermal performance, and therefore they were included in all data presented in this work. Although the upstream spray temperature, copper cooling coil, and external heat exchanger were all maintained at nominally 30°C , hot spent gas leaving the heated surface resulted in an increase in the downstream temperature. The downstream temperature ranged from 30.6°C (for the bare surface at its lowest heat flux) to 40.8°C (for the 3 mm long fins at its highest spray efficiency). This downstream thermocouple within the spray cone was considered the most accurate measure of the average spray temperature and was used in all calculations below.

A nominally full cone spray nozzle was used. This pressure atomizing nozzle had an orifice diameter of $404 \pm 14 \mu\text{m}$. The nozzle was fixed $18 \pm 1 \text{ mm}$ above the heated wall (i.e. the base of the fins for the finned surfaces), which resulted in a spray that appeared to approximately inscribe the square test surface at the smooth-wall elevation.

The nominal flow rate through the nozzle ranged from $69 - 123 \pm 1$ mL/min, however the amount of fluid incident on the test surface was less due to some overspray. Since the nozzle height was fixed with respect to the heated wall, the incident flux on the top of the fins increased with fin length due to decreased overspray (Fig. 24).

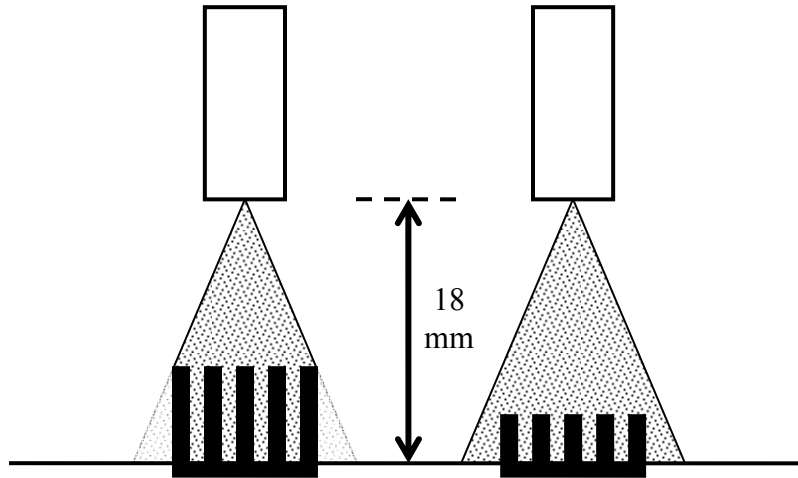


Fig. 24. Illustration of overspray and incident flux increasing with fin length.

The amount of fluid incident on the top of the fins was measured by removing the heaters and replacing them with rapid prototyped collection funnels that were shaped as hollow, truncated, square pyramids. The top lip of the funnel was placed at the same height as the upper surface of the finned heat sinks and featured a 2 cm^2 opening that allowed incident fluid to be collected into a graduated cylinder. The collection system (Fig. 25) was sealed from the ambient and vented to the spray chamber to prevent evaporation. The amount of fluid incident on each of the heat sinks is given in Table 8.

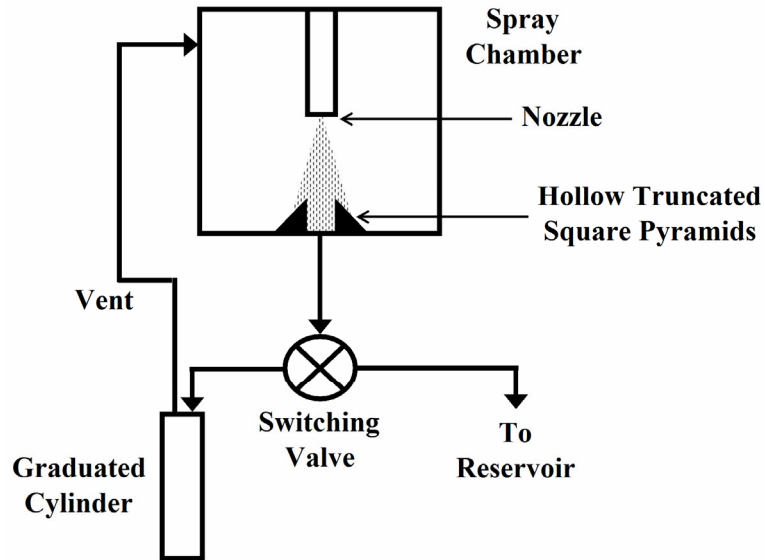


Fig. 25. Incident flow measurement system.

Table 8. Fluid flow rate incident on top surface of heat sinks.

Fin Length [mm]	Fraction of Total Flow Rate Incident on Top Surface (± 0.02)
0	0.75
0.25	0.76
0.5	0.77
1	0.78
3	0.85
5	0.91

The Sauter mean diameter (SMD) of the droplets was estimated using the correlation of Estes and Mudawar (1995), Eq. 15. The SMD varied from 54 to 72 μm over the range of pressures used. The droplet breakup velocity was estimated using Ghodbane and Holman’s (1991) expression, Eq. 18, and was found to range from 13 to 22 m/s.

3.3.4. Data Acquisition and Control

Data acquisition and heating control (Fig. 26) were provided by a custom Visual C++ program implemented through a general programming interface bus (GPIB) on a

Pentium III personal computer. An HP6675A DC power supply provided a controllable power source, while a Fluke Hydra Data Acquisition Unit acquired data every six seconds. Power was initially set at 30 W and thermocouple temperatures were monitored to determine when steady state occurred. Once the time- and space-averaged temperature in the heater neck changed by less than 0.1°C over a 60 second period, 60 seconds of steady-state data were recorded. Power was then incremented by 10 W, and system monitoring resumed. Experiments were concluded when the temperature of the heating block (monitored with two separate thermocouple probes) reached a temperature limit of 260°C, set to ensure safe operation of the test apparatus or when the surface temperature increased rapidly indicating CHF.

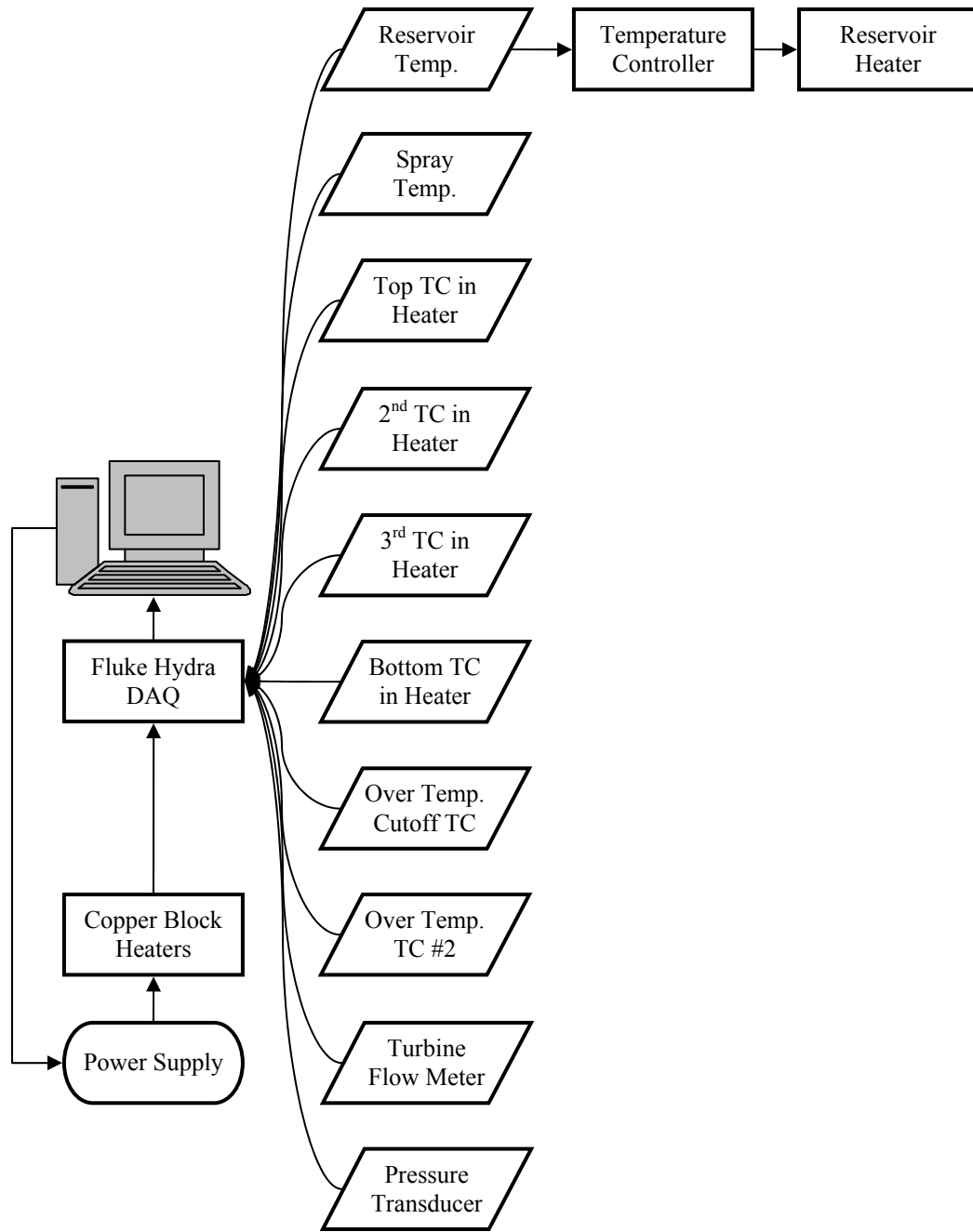


Fig. 26. Data acquisition and control diagram for microchannel spray cooling.

CHAPTER 4. UNCERTAINTY AND DATA ANALYSIS

The majority of the quantitative results of this dissertation are spray cooling and boiling curves. This chapter, therefore, describes the methods used to calculate heat flux and surface temperatures. The uncertainties in these calculations were estimated using both standard propagation of uncertainty techniques and Monte Carlo methods (the basics of this method are described in Appendix C). Furthermore, finite element models were developed to investigate heat losses and verify the validity of the heat flux calculations. Finally, this chapter reviews the methods used to determine the uncertainty of the contact angle measurements. Unless otherwise noted, all error bars shown in figures are based on twice the standard deviation (i.e., 95.5% confidence).

4.1. Thick-film Resistive Heater

The power dissipation of the thick-film resistor was obtained by dividing the square of the measured voltage drop by the resistance. The error in the heat flux was then calculated using the standard propagation of uncertainty technique (Lyons, 1996):

$$\sigma_{q''} = \sqrt{\left(\frac{2V}{RA} \sigma_V\right)^2 + \left(\frac{V^2}{R^2 A} \sigma_R\right)^2 + \left(\frac{V^2}{A^2 R} \sigma_A\right)^2} \quad (34)$$

Errors in heat flux were found to be 4% (with 95% confidence), due in large part to the error in the exposed heater area.

The average temperature of the boiling surface was measured by an RTD bonded to the backside of the heater. The RTD had approximately the same area as the heater. Furthermore, the relatively high thermal conductivity of the alumina substrate ($k=36$ W/m·K) and the insulation provided by the G-10 base ($k=0.25$ W/m·K) ensured that there was negligible temperature difference between the front and backside of the heater. The

RTD was calibrated with a NIST traceable liquid-in-glass mercury thermometer producing a linear calibration curve. To estimate the errors in RTD measurements, a two-part Monte Carlo simulation was used (this was an extension of the basic method described in Appendix C).

The first step in the simulation process involved simulating the calibration. The actual calibration involved 5 separate measurements of resistance and temperature. For each iteration of the simulation, 5 sets of random measurements (resistance and temperature) were used to create a linear calibration curve. The inputs were based on the nominal values (recorded during the calibration) plus random normally distributed errors (based on DAQ accuracy and thermometer reading error)[†]. Running 10,000 iterations produced the statistical equivalent of calibrating 10,000 times. This yielded 10,000 pairs of coefficients (constant and linear terms).

In the second step, the use of the calibration was simulated. In typical practice, a resistance measurement would be input into the calibration curve to determine the temperature. For the Monte Carlo simulation, additional random data were input into the simulated calibrations. The inputs were based on typical RTD resistances that were added to random normally distributed errors (again based on DAQ accuracy). The random RTD measurement was simulated once for each of the 10,000 simulated calibrations, making a total of 10,000 different estimates. Figure 27 shows a histogram of typical results. The estimated error in the RTD measurement was then determined by taking twice the standard deviation of all 10,000 results. In this manner, the error in surface temperature was estimated to be 0.1 °C.

[†] Reading errors are uncorrelated, but DAQ accuracy is correlated (i.e., the same for each measurement) since all measurements are made with the same device. Uncorrelated errors are based on unique random numbers. Correlated errors are based on the same random number.

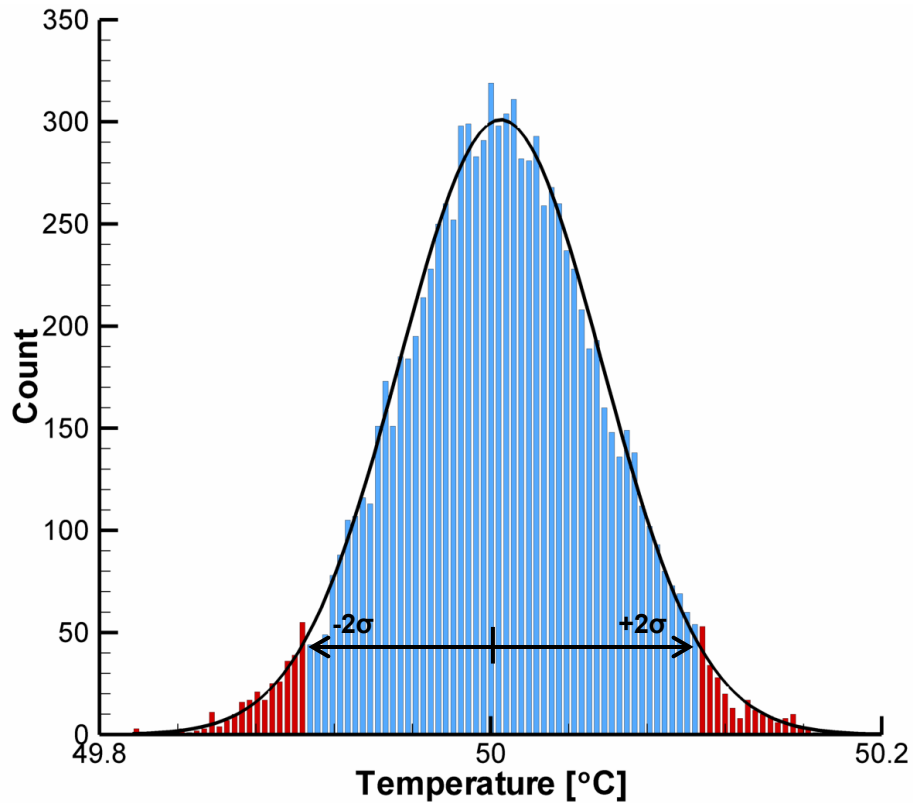


Fig. 27. Histogram of Monte Carlo results with input from an RTD measurement that corresponds to a nominal temperature prediction of 50 °C.

To determine the heat losses, the heater assembly was modeled using commercial finite element software (FEMLAB). Natural convection from the G-10 base, silicone, and aluminum press were modeled using the Lloyd and Moran (1974) correlation:

$$Nu = 0.54Ra_L^{1/4} \quad (35)$$

The natural convection heat transfer coefficient was found to be 225 – 325 W/(m²·K). The chip power and temperature measured during the experiment were input into the model. Then, the boiling heat transfer coefficient was determined iteratively by assuming a value and verifying the modeled power dissipation against the measured chip power. A representative surface temperature plot for a quarter section of the heater assembly is shown in Fig. 28. Up to 28% of the applied power was lost to the insulation in the

natural convection regime of the boiling curve. This heat loss dropped to 12.8% by the onset of nucleate boiling and continued to decrease as the wall temperature increased. At CHF the heat loss was only 3 – 4%. Results from nine simulations (from the natural convection regime through CHF) were used to determine the heat losses as a function of applied heat load. The estimated heat loss was then subtracted from the raw power dissipations measured during the experiment for all the results presented in Chapter 5.

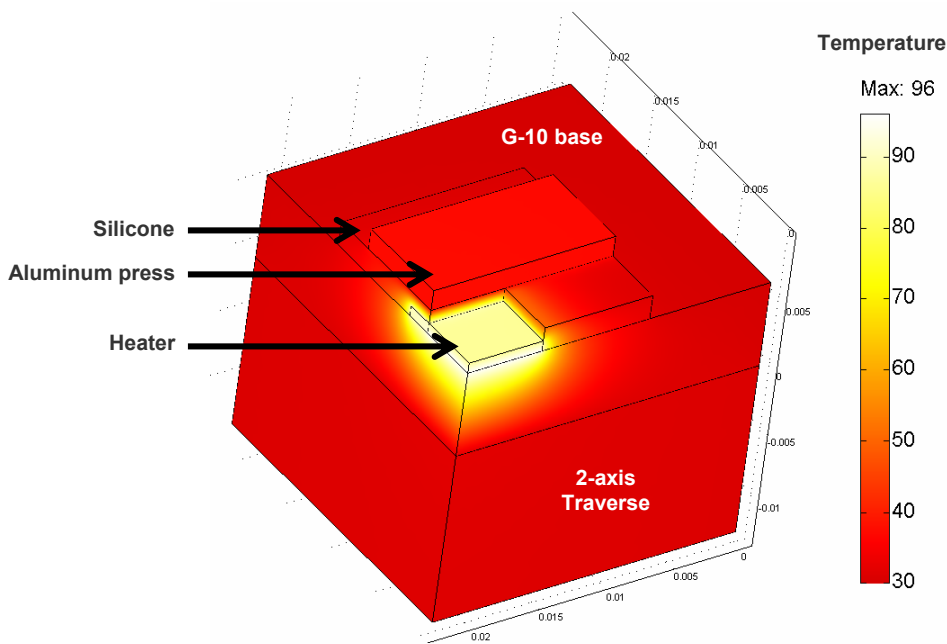


Fig. 28. Finite element model of a quarter section of thick-film heater.

4.2. Copper Block Heaters

Copper block heaters were instrumented with thermocouples along the length of their necks to measure the temperature gradient. Since the necks of the heaters were insulated by air (free convection losses were small), the heat applied at the bottom of the heater traveled primarily in the axial dimension (the assumption of 1-D conduction is explored later in this section). From the measured temperature gradient, the heat flux was calculated using Fourier's Law.

$$q'' = -k \frac{dT}{dx} \quad (36)$$

The thermal conductivity of pure copper is known to be 391 W/m·K (ASM International, 2001). The temperature gradient was determined from a least squares fit of the temperature measurements:

$$\frac{dT}{dx} = \frac{\sum_{i=1}^4 (x_i - \bar{x})(T_i - \bar{T})}{\sum_{i=1}^4 (x_i - \bar{x})^2} \quad (37)$$

The error in the heat flux was again calculated using the standard propagation of uncertainty technique:

$$\sigma_{q''} = \sqrt{\left(k \sigma_{dT/dx}\right)^2 + \left(\frac{dT}{dx} \sigma_k\right)^2} \quad (38)$$

To calculate the heat flux error, the error in the thermal conductivity was assumed to be 5%, and the error in the temperature gradient was calculated using a Monte Carlo simulation. This simulation was similar to the one described above in the thick-film heater section. In this case, the measured temperatures from the neck of the copper block, thermocouple positions, and random normally distributed errors were input into the simulation and 10,000 temperature gradients were determined. The error was again determined by taking twice the standard deviation of all 10,000 temperature gradients.

The temperature of the boiling/sprayed surface was determined by extrapolating the linear temperature profile out to the wall. If the boiling/sprayed surface is defined as $x=0$ in the least squares fitting process, then the wall temperature is given by the constant determined with the fit:

$$T_{wall} = \bar{T} - \frac{dT}{dx} \bar{x} \quad (39)$$

The error in wall temperature was also determined using the Monte Carlo technique.

4.2.1. Boiling Heater

The method described above was used to calculate the errors associated with the copper/copper oxide boiling experiments. Figure 29 shows an example of the linear least squares fit compared to actual temperature measurements. The absolute value of the residuals averaged 0.1°C , and the largest deviation from the fit was 0.7°C . Figure 29 shows the temperature distribution to be very linear proving the assumption of 1-D conduction to be a valid one.

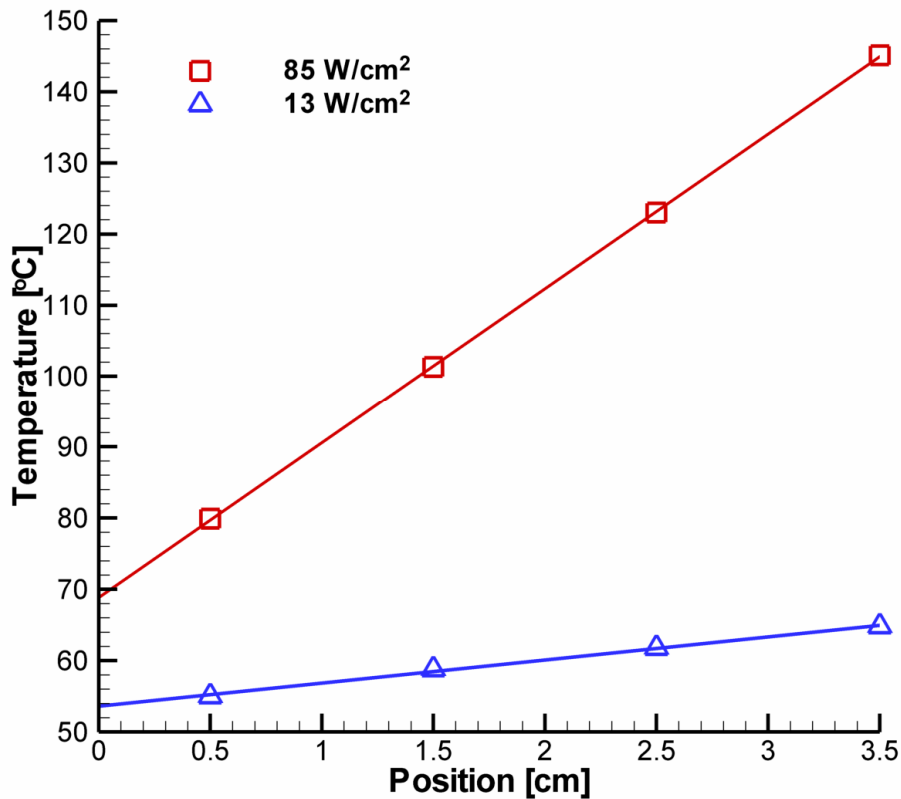


Fig. 29. Typical temperature profiles in the neck of the copper heater block (data from 0.05 g/L alumina-in-water nanofluid boiling on well oxidized copper).

Using the analysis described above, the heat flux error was estimated to be 5%. The wall temperature error was dependent on temperature gradient and ranged from 0.3 to 0.7°C (95% confidence estimates). The average wall temperature error was 0.4°C .

By measuring the power delivered to the cartridge heaters and comparing to the heat transfer calculated assuming 1-D conduction, the fraction of heat lost was found to be 0.21 ± 0.02 . To verify that this heat loss was reasonable, a heat loss prediction was made based on a 3-D finite element model developed in FEMLAB. The entire copper block was modeled, and heat transfer coefficients were applied to the external boundaries. The boiling heat transfer coefficient was assumed to be $10,000 \text{ W}/(\text{m}^2 \cdot \text{K})$ based on the boiling curves presented in Chapter 5. The free convection heat transfer coefficient was assumed to equal $10 \text{ W}/(\text{m}^2 \cdot \text{K})$, which is in good agreement (within 10%) with Lloyd and Moran (1974), Eq. 35. The resulting false-color temperature plot is shown in Fig. 30. The heat loss was estimated to be only 7%. Varying the boiling heat transfer coefficient from half to twice the default value changed the heat loss from 10% to 5%, respectively. Therefore, the difference between the modeled and measured heat loss is likely due to the cartridge heaters, which extended outside their holes. Due to their poor fit into the copper block, the heaters would be hotter than the copper block and could contribute significantly to the heat loss through natural convection. Unfortunately, this portion of the heat loss cannot be modeled because the contact resistance between the heaters and the copper block is unknown. However, the modeling results confirm that the measured heat lost is reasonable.

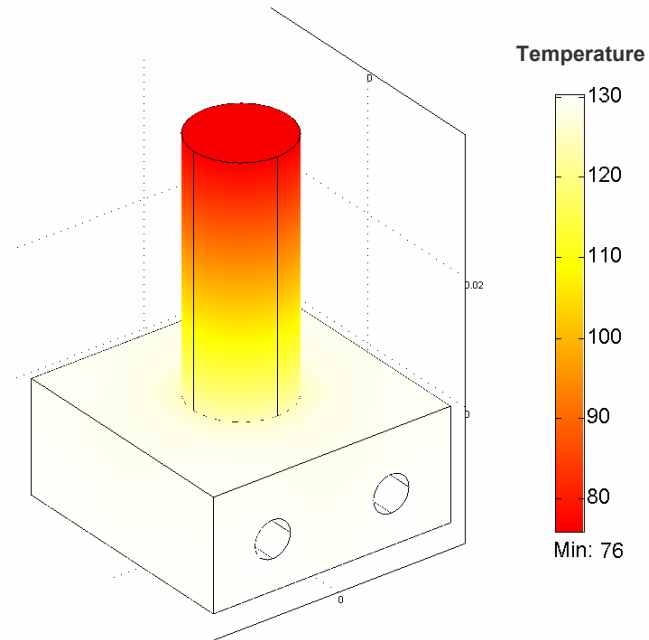


Fig. 30. Finite element model results for copper block with boiling at the top of the neck and free convection heat losses.

4.2.2. High Aspect Ratio Open Microchannel Spray Cooling Heater

The copper block heater used in the extended surface studies was similar to the boiling block described above. Therefore, the analyses used to calculate the heat flux and wall temperature were the same. Using the same procedure outlined above, the error in the heat flux was estimated to be 5%. The wall temperature error ranged from 0.3 °C – 0.7 °C, with an average of 0.4 °C.

Heat transfer calculated assuming 1-D conduction was 0.87 ± 0.02 times the power supplied to the cartridge heaters, depending on ambient conditions and the contact resistance of the threaded heating neck. This heat loss was consistent with losses expected due to natural convection from the base, verified using the Lloyd and Moran (1974) correlation, Eq. 35.

Another potential for heat losses was to the ceramic insulation, which was also modeled in FEMLAB. For the spray impacted heater, the heat transfer coefficient was estimated based on the data presented in Chapter 6. However, the heat transfer coefficient outside the spray impact region would be much lower as noted by Sakamoto et al. (2006). Therefore, the heat transfer coefficient in the region just outside (within 2 mm) of the heater was assumed to be only 10% of the heat transfer in the impacted region. The far-stream region where there was essentially no flow was assumed to have a heat transfer coefficient of $100 \text{ W}/(\text{m}^2\cdot\text{K})$. In this manner, losses from the heater to the insulation were found to be about 1 – 2% depending on the experimental data point being modeled. A false-color temperature plot of the modeling results is shown in Fig. 31.

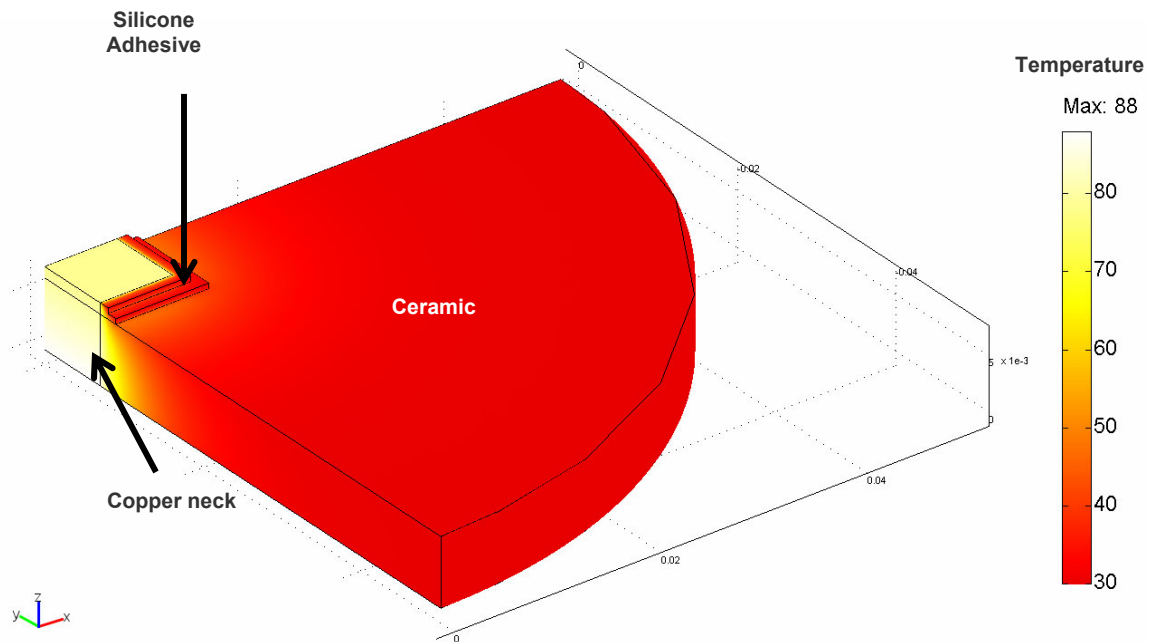


Fig. 31. Finite element model of a quarter section of the heater, silicone adhesive, and ceramic insulation showing the temperature distribution.

The spray cooling results that are presented in the following chapter have been corrected to account for this modeled heat loss (i.e., the heat loss was subtracted from the original flux calculated using Fourier's Law).

4.3. Contact Angle Measurements

Contact angle measurements are notoriously difficult to reproduce due to surface irregularities (de Gennes, 1985) and a variety of measurement techniques available to investigators. In this study the measurements were made using consistent surface preparation, infusion rate, lighting, and imaging. However, contact line pinning caused individual still photographs of the contact angle to differ. Therefore, all angles reported in the present work are averages of all the measurements made for a particular surface. Furthermore, the ellipse fitting technique described in Chapter 3 resulted in $\pm 1.3^\circ$ variability due to the author's choice of points along the droplet interface. The standard deviation of advancing contact angles was determined by adding these two sources of variability using the standard square root sum of squares technique:

$$\sigma_{\bar{\theta}} = \left(\frac{\sum_{i=1}^n (\theta_i - \bar{\theta})^2}{n-1} + \sigma_{\text{ellipse fit}}^2 \right)^{1/2} \quad (40)$$

After combining these two sources of uncertainty, the standard deviation of advancing contact angles were found to range from 2° to 9° .

CHAPTER 5. NANOFUID POOL BOILING & SPRAY COOLING

A literature review of nanofluids properties indicates some promise for two-phase heat transfer improvement. Pool boiling systems are considered first as a prerequisite to utilization in more complex spray cooling.

5.1. Boiling Ethanol Based Nanofluids

Due to the lack of prior research, little is known of how ethanol based nanofluids differ from water based nanofluids. Ethanol is unlike water in that it is highly wetting: the three-phase (liquid-vapor-substrate) contact angle is very small. Therefore, it is possible that the mechanisms responsible for heat transfer enhancement are quite different with ethanol than with water. This thesis has focused on the relationship between wetting characteristics and nanofluid performance. To that end, ethanol based nanofluids were used with three different substrates: glass, gold, and copper.

5.1.1. Glass Surface

The steady-state boiling curves for the ethanol based nanofluid on glass are shown in Fig. 32. The nanofluid concentration was varied from 0.001 g/L to 0.5 g/L and no enhancement or degradation in CHF was observed. The nucleate boiling heat transfer coefficient was also unaffected by the nanofluid concentration. This seems to contradict the findings of other researchers such as You et al. (2003) and Vassalo et al. (2004), who observed significant CHF enhancement. It also seems to contradict the work of Yang and Maa (1984) who found significant nucleate boiling enhancement. Furthermore, this also seems to contradict the work of Das et al. (2003) who observed nucleate boiling

degradation. However, it is important to note that these results are for different experimental conditions. Specifically, the base fluid and substrate material are different.

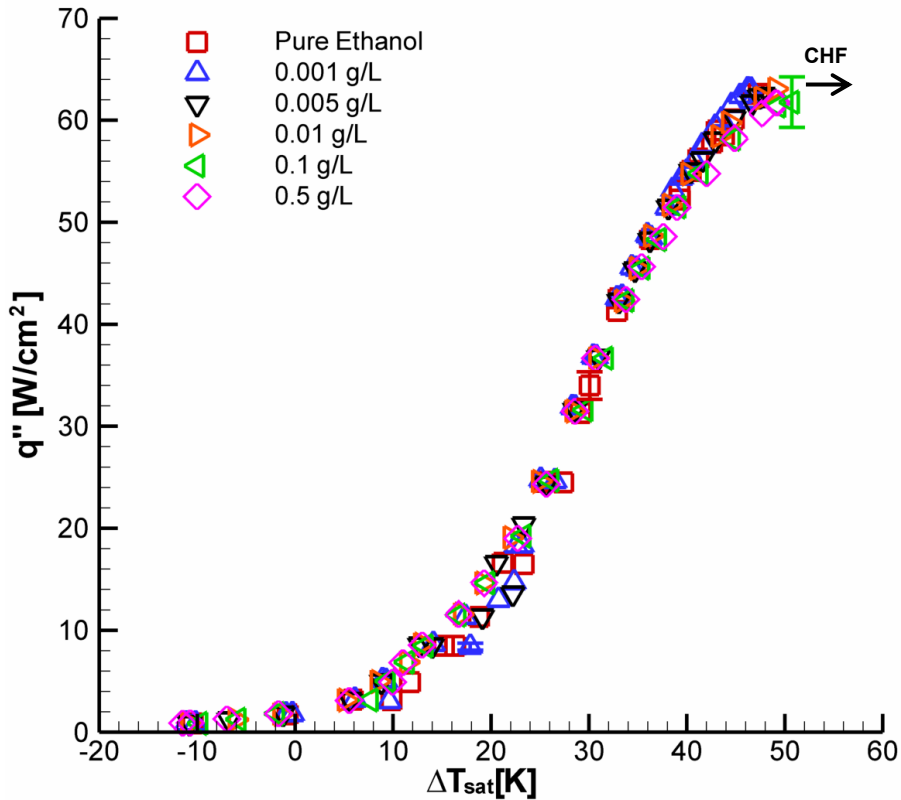


Fig. 32. Steady-state boiling curves for subcooled ($T_{sat} = 51.7 \text{ }^\circ\text{C}$, $T_{bulk} = 30.6 \text{ }^\circ\text{C}$) alumina/ethanol nanofluid over a range of concentrations on glass.

Two hypotheses were developed to explain the observed behavior. First, the concentrations used may be insignificantly small. While the concentrations used were typical of nanofluid boiling studies, they are in fact quite small. Should inert oxide particles in such small quantities actually improve boiling heat transfer? Another view of the concentration would be to consider that the particulate loading of “pure” fluid is relatively high. Consider that there are of 10^4 particles per cubic centimeter in the typical room and 10^5 per cubic centimeter in a polluted urban atmosphere (Friedlander, 2000). Even using distilled water, particles would be present in the room, test apparatus, and

ultimately the working fluid. The nanofluid concentrations used may have been too similar to the particulate loading of the “pure” fluid to observe an effect on boiling performance.

The second hypothesis was that the lack of a nanofluid effect might be due to the highly wetting nature of the ethanol/glass system. The above mentioned CHF enhancement studies were with water based nanofluid, and water is less wetting than ethanol (see Fig. 33). If the nanofluid served to increase the liquid’s affinity for the surface, then the ethanol/glass system might have little need for improved wettability. Nanofluid systems including metal surfaces and water like those studied by You et al. (2003), Vassalo et al. (2004), and others might indeed have benefited from increased wetting.

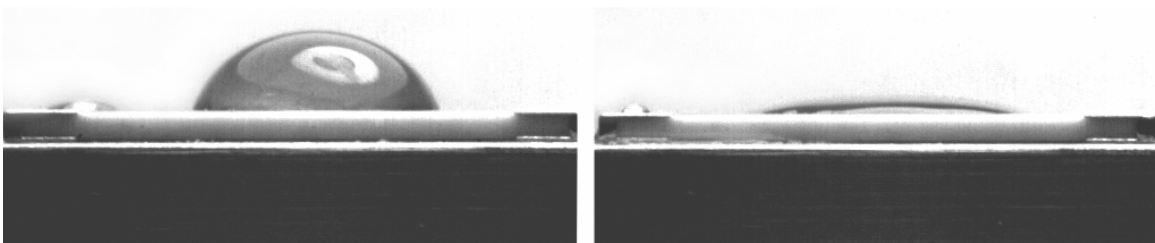


Fig. 33. Photographs of static droplets on a glass substrate (water on the left, ethanol on the right).

5.1.2. Gold Surface

The glass substrate used in the above study was then coated with a 100 nm gold layer to decrease the surface energy and surface wettability. The steady-state boiling curves for the alumina-in-ethanol nanofluid on gold are shown in Fig. 34. Tests were performed with pure fluid, as well as nanofluid concentrations of 0.01 g/L and 0.1 g/L. Effects on CHF enhancement and the nucleate boiling heat transfer coefficient were again minimal. While this test does provide support for the theory that dilute nanofluids are

insignificant, it is not definitive since the working fluid used (ethanol) is still highly wetting. A better test would be to systematically change the surface wettability to determine if nanofluids improve heat transfer through a surface wettability modification. This kind of surface wettability experiment was done with water based nanofluid on copper surfaces with various levels of oxidation and will be discussed later. However, ethanol based nanofluids were also tested on a copper surface, specifically a pure copper block.

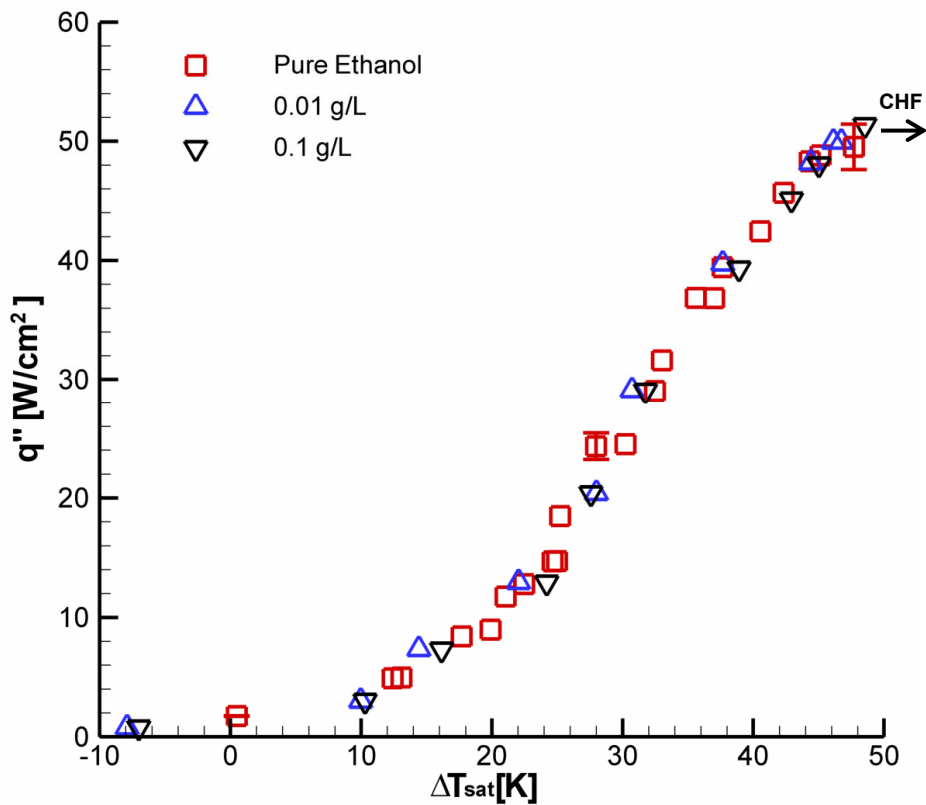


Fig. 34. Steady-state boiling curves for subcooled ($T_{sat} = 51.7 \text{ }^\circ\text{C}$, $T_{bulk} = 30.6 \text{ }^\circ\text{C}$) alumina/ethanol nanofluid on gold.

5.1.3. Copper Surface

The final surface used with ethanol based nanofluids was a copper substrate. This time the nanofluid concentration was varied over four orders of magnitude from 0.06 g/L

to 10.07 g/L. The pool was not subcooled in these tests unlike the previous tests because the large thermal mass of the heater resulted in long experiments and a large heat load that proved difficult for the condenser to handle. With the higher heat fluxes of subcooled boiling it was not possible to keep the pool at a nominally constant temperature. However, under near saturated conditions, with a lower heat flux, the pool could be maintained at nominally 30°C. The steady-state boiling curves for near saturated boiling of alumina-in-ethanol nanofluids is shown in Fig. 35.

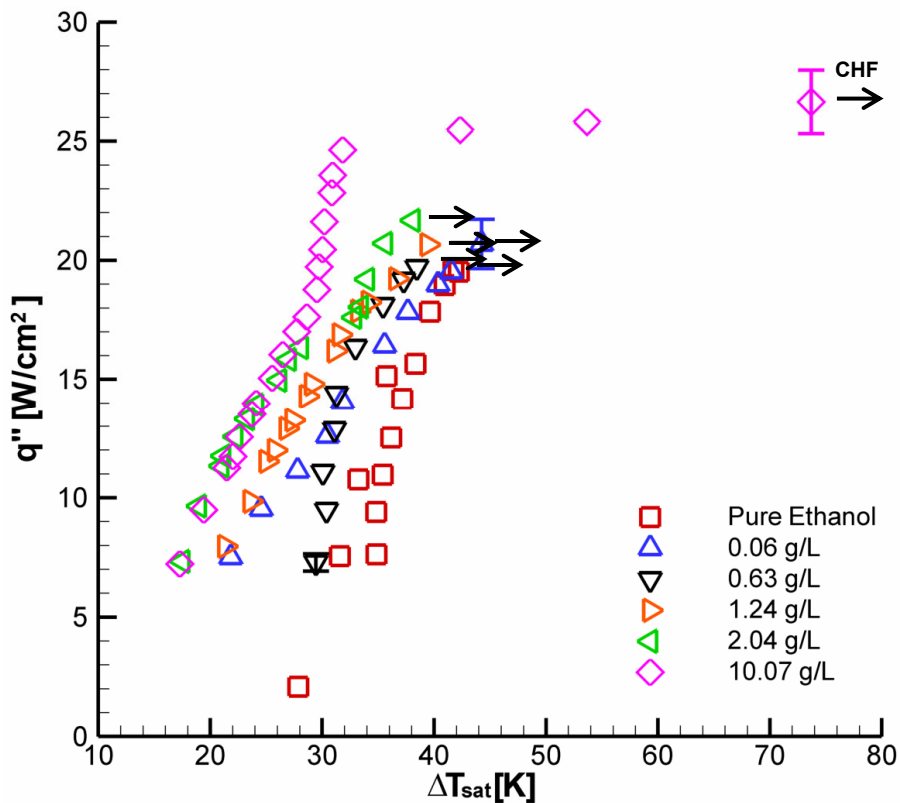


Fig. 35. Steady-state boiling curves for near saturated ($T_{sat} = 28.9$ °C, $T_{bulk} = 28.8$ °C) alumina/ethanol nanofluid on copper.

This system illustrates vastly different phenomena than were previously observed. First, the nucleate boiling regime is marked by a decrease in superheat required to achieve a given heat flux. Second, there is a CHF enhancement at high particle loadings,

while very dilute suspensions (like those reported by You et al. (2003)) produced no significant CHF enhancement. Third, there is a very slow dryout or transition to film boiling at high particle loadings.

The nucleate boiling results appear to agree with Yang and Maa (1984) and Wen and Ding (2005). They are also contrary to the findings of Das et al. (2003). The decrease in superheat required to achieve a certain heat flux was determined for three different fluxes (by interpolation of the data) and was plotted as a function of particle concentration (see Fig. 36). At low concentrations, the superheat required decreased linearly. However, the highest concentration, 10.07 g/L, was very similar to the next lower concentration. The precise reasons for this behavior is unknown but could be explained by particles depositing onto the surface and increasing the nucleation site density. This may also help explain the CHF enhancement.

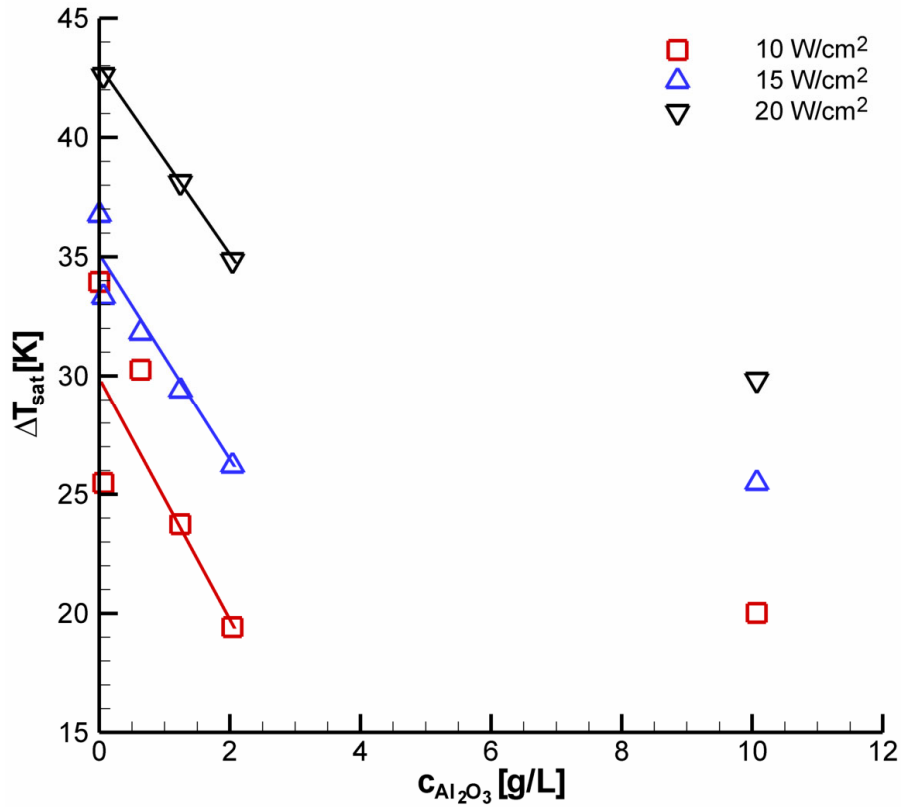


Fig. 36. Superheat required for a given heat flux for various alumina-in-ethanol nanofluids on copper.

The CHF enhancement is shown as a function of concentration in Fig. 37. CHF was enhanced up ~25% at the highest particle loading. This enhancement is significantly less than that reported by You et al. (2003) or Vassalo et al. (2004). Furthermore, the concentrations required to see an enhancement were about 1000 times as large as those used by You et al. (2003), although about half that used by Vassalo et al. (2004). The fact that very dilute solutions provided little or no enhancement and that 10 g/L provided ~25% enhancement in CHF may provide insight into the mechanisms responsible.

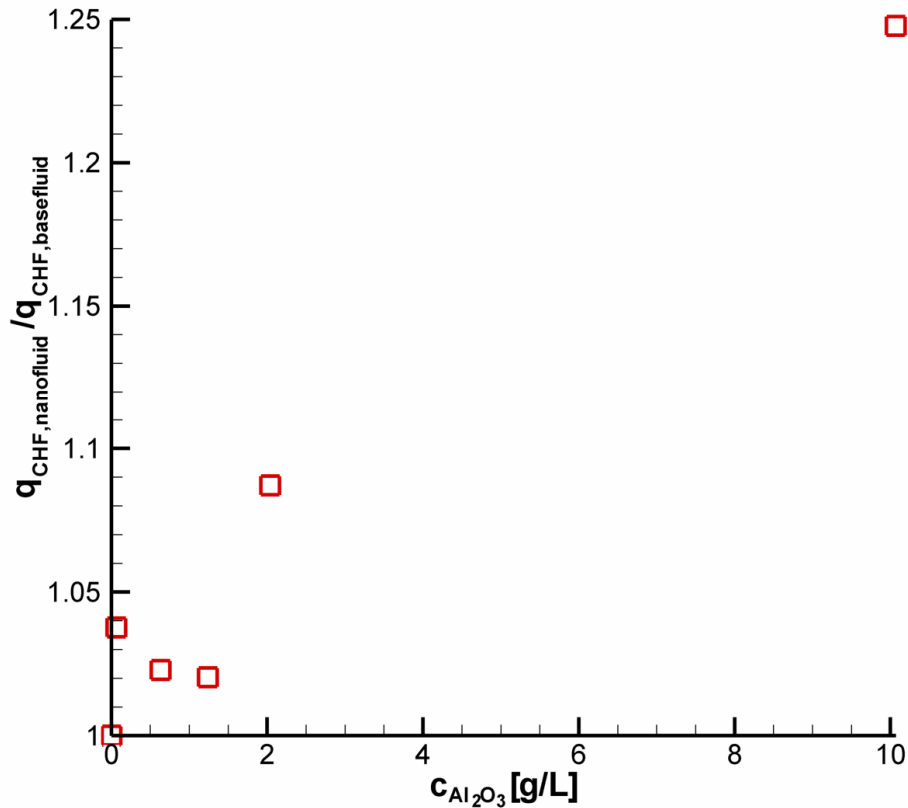


Fig. 37. CHF enhancement as a function of nanoparticle concentration for near saturated ethanol suspensions on copper.

First, consider the thermal conductivity, which will need to be estimated since there is no reliable theory for the thermal conductivity of nanofluid. Figure 38 shows the thermal conductivity enhancement measured at room temperature by various research groups. There are clearly differences due to preparation method, particle size, and base fluid. However, there is a linear trend with respect to particle volume fraction. Using this linear fit, the thermal conductivity of the 10 g/L suspension is estimated to be 1% higher than the base fluid. The more dilute suspensions provide a negligible increase in thermal conductivity. Given that CHF is a weak function of thermal conductivity, this difference is insufficient to account for the CHF enhancement.

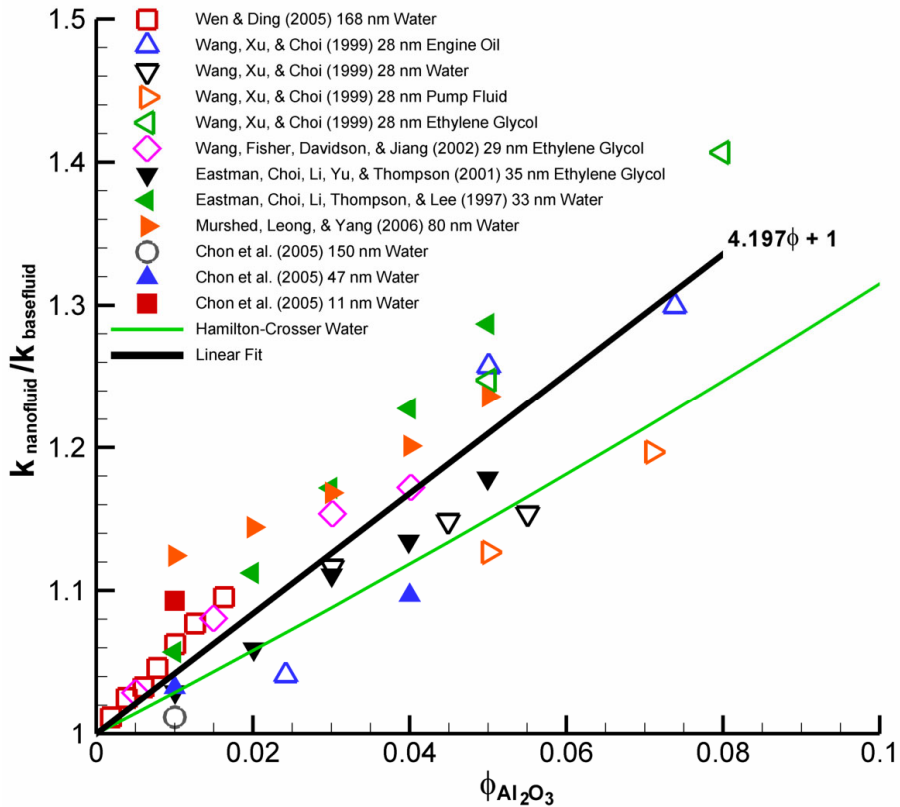


Fig. 38. Thermal conductivity enhancement of alumina nanofluids at room temperature.

A second possible explanation for the observed enhancement in both nucleate boiling and CHF is nucleation theory. Lowery and Westwater (1957) showed that small quantities of additives could affect all aspects of the boiling curve. They tested cationic, anionic, and nonionic agents in methanol with a variety of concentrations from 0.001 – 1 wt.%. They measured both the surface tension and the receding contact angle (from photographs of growing bubbles). Both were found to be nominally constant across the different test liquids. Therefore, they speculated that nucleation theory provided a possible explanation. With the addition of small particles or large molecules, additional interfacial tensions become important, namely the particle-liquid-vapor system. This could create a “synthetic nucleus” promoting vapor generation on the hot solid and/or in surrounding superheated liquid. Such a mechanism might be necessary for one to

observe an increase in boiling heat transfer. Those systems lacking nucleation sites might be improved with nanofluid, while a different mechanism such as fouling may degrade a system with sufficient pre-existing nuclei. This would also explain the importance of nanoparticle concentration, with higher concentrations leading to more nuclei and higher heat transfer.

A third possible explanation for the behavior observed is the effect of the proprietary dispersant that was used in the preparation of the commercial nanofluid. According to the manufacturer's Materials Safety Data Sheet (MSDS), as provided the nanofluid contains 0.5 – 20% dispersant (Nanophase Technologies Corporation, 2003). As mentioned above, additives are known to affect the boiling process. One particular type of additive that has been shown to affect nucleate boiling is surfactants. Ammerman and You (1996) showed that the addition of the surfactant sodium dodecyl sulfate (SDS) to water resulted in a significant increase in the heat transfer coefficient. They correlated this with an increase in the convective component of heat transfer and a decrease in the latent heat component. Since the exact nature of the dispersant used in the preparation of the nanofluid is unknown, it is possible that the decrease in superheat observed in this work is due to the increase in dispersant concentration. Unfortunately, the two effects are difficult to separate since a dispersant is required to make a stable nanofluid.

5.2. Boiling Water Based Nanofluids

With the novel findings from the ethanol based nanofluids research discussed above, an attempt was made to verify the work of other researchers by using water based nanofluids. This section discusses the follow-on work on boiling with alumina-in-water on copper and copper oxide surfaces. The surface wettability was systematically varied

by increasing the oxidation of the copper surface as well as varying the nanofluid concentration.

5.2.1. Concentration Effects

Using the same copper surface as discussed in the previous section, alumina-in-water nanofluids were used in near saturated pool boiling. The steady-state boiling curves are shown in Fig. 39. No discernable effect was observed in the nucleate boiling regime due to scatter in the data. However, the CHF varied with concentration. Again, different trends were observed with dilute suspensions than with more concentrated ones. Specifically, dilute suspensions actually decreased the CHF slightly, while the higher concentrations resulted in significant CHF enhancement. The CHF enhancement is shown as a function of alumina concentration in Fig. 40. The reasons for this unique dependence of CHF on concentration is not completely understood. If the addition of foreign nuclei were to explain these results, then an increase in the nucleate boiling regime would be expected. If the nucleate boiling regime is at all affected by the addition of nanofluid, then it is much smaller than that observed with the ethanol based nanofluids discussed above.

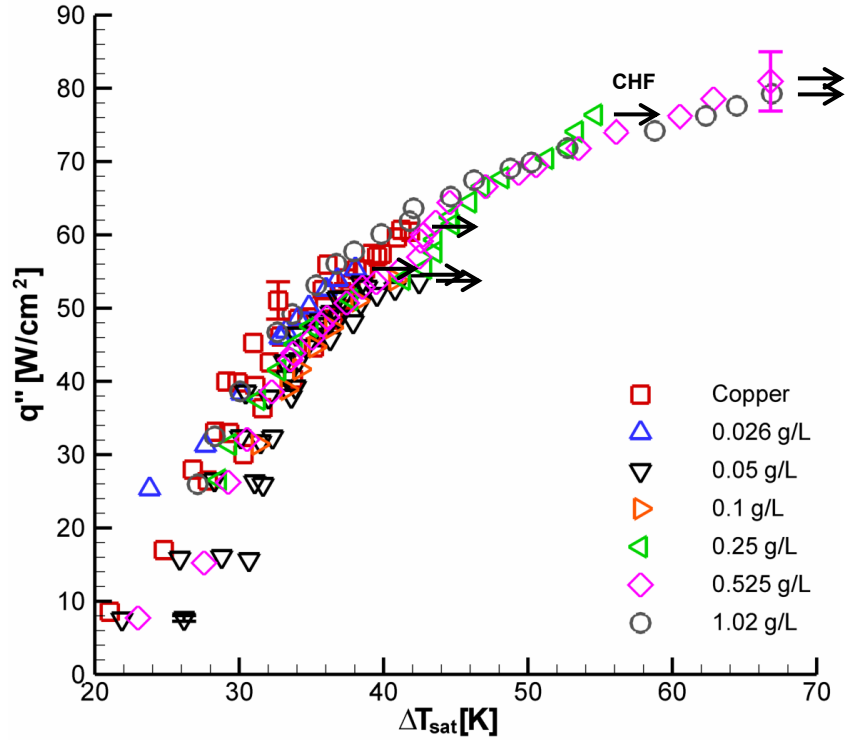


Fig. 39. Steady-state boiling curves for near saturated ($T_{sat} = 29.8\text{ }^{\circ}\text{C}$, $T_{bulk} = 29.3\text{ }^{\circ}\text{C}$) alumina/water nanofluid on copper.

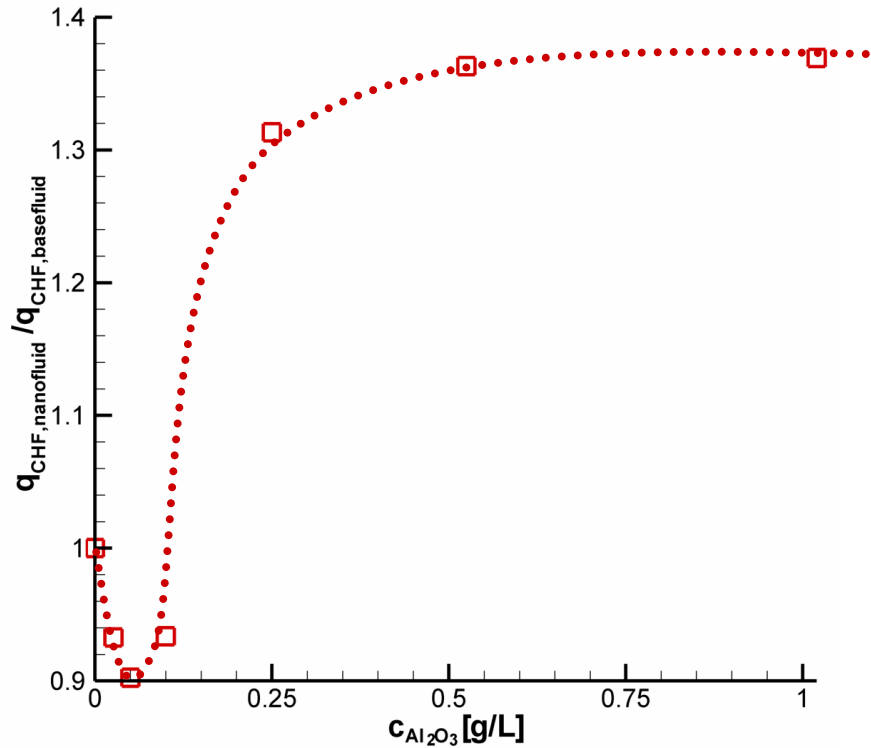


Fig. 40. CHF enhancement as a function of nanoparticle concentration for near saturated water suspensions on copper.

Another possible explanation might be fouling. Moreno et al. (2005) observed impressive CHF enhancement, up to ~240%, but they also noticed that higher concentrations (≥ 0.025 g/L) resulted in the deposition of a thin film on the heater surface. At even higher concentration (0.5 g/L), they observed a decrease in nucleate boiling heat transfer, which may have been caused by the particulate film. This kind of particle deposition could easily affect all aspects of the boiling curve. The deposition of the film would change the nucleation site density. Das et al. (2003) theorized that surfaces with large roughness scales could be plugged by nanoparticles resulting in a smoother surface. The particulate film would also add conduction and contact resistances which would depress heat transfer. At what point the degradation mechanisms outweigh any enhancement remains unclear. This may explain the complex dependence on particle concentration observed in this study.

The CHF enhancement observed with water based nanofluids was larger than with ethanol (~37% compared to ~25%) for the same heater. Furthermore, lower nanoparticle concentrations were required for CHF enhancement with water based fluids. This apparent discrepancy may be due to the poorer wetting characteristics of water. This is explored in some detail later because there is some evidence to suggest that surface wettability is responsible for the observed CHF enhancement. Consider the water/ethylene glycol results of Moreno et al. (2005), who observed that the CHF enhancement caused by nanofluids decreased as the volume fraction of ethylene glycol increased. The authors provided no explanation for the observed behavior, but detailed consideration of the thermophysical properties can provide insight. For instance, the surface tension of water/ethylene glycol mixtures has been shown to decrease as the

ethylene glycol fraction is increased (see Fig. 41). If the nanofluid is depositing particles that increase wettability, then liquids with lower surface tensions should be less affected. The data of Moreno et al. (2005) shows this precisely. As they increased the amount of ethylene glycol, the surface tension would decrease. This then makes the surface easier to wet and nanoparticles less significant. The result is that the CHF enhancement disappeared as the concentration of ethylene glycol was increased.

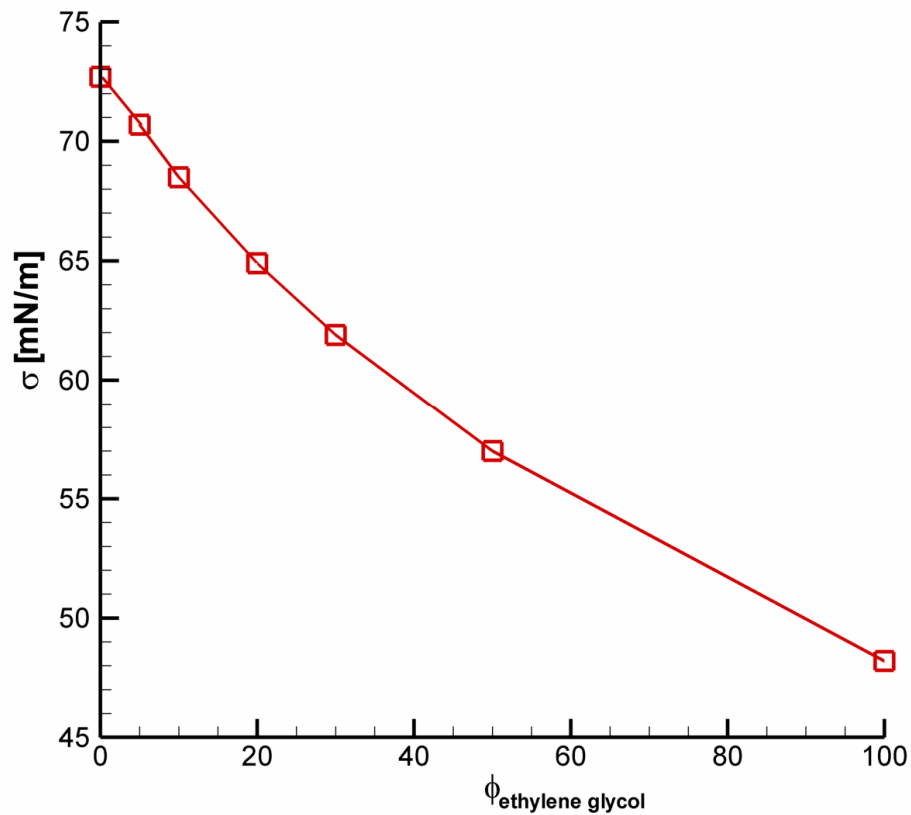


Fig. 41. Surface tension of water/ethylene glycol mixtures at 20 °C (after Horibe et al., 1996).

The unexpected degradation/enhancement of CHF observed with water based nanofluids indicates that the effect of nanofluids on boiling remains ambiguous. However, the present data in concert with the literature indicates that it is likely that the ultimate mechanism for heat transfer augmentation is a change in surface microstructure.

5.2.2. Surface Wettability Effects

To test the hypothesis that nanofluids augment boiling heat transfer through a modification of the surface microstructure and an improvement in surface wetting, the wetting of the copper surface was systematically improved by growing a native oxide. Pure water was tested on the same copper heater oxidized to five different surface oxidation levels. Nanofluid then was used on both the least and most oxidized of these surfaces. To isolate the effect of the surface oxidation, its wettability was characterized prior to the experiment by measuring the advancing contact angle with pure water. In many cases, the contact angle was also measured after the experiment to determine if further oxidation occurred during the run. Again, this measurement was made with pure water to isolate the effect of the surface alone. The test matrix is shown in Table 9.

Table 9. Test matrix in the order in which it was run. † These angles were measured after the surface was rinsed with water.

Trial No.	Oxidation Level	Fluid	θ_{prior} [degrees]	θ_{post} [degrees]
1	None	Pure Water	83±3	63±3
2	None	Pure Water	79±4	64±2
3	Light	Pure Water	56±3	36±4
4	None	Pure Water	65±9	60±4
5	Medium/light	Pure Water	62±8	43±5
6	Medium	Pure Water	97±5	41±4
7	Heavy	Pure Water	25±6	-
8	Heavy	Nanofluid	-	43±6 [†]
9	Heavy	Nanofluid	43±6	41±4 [†]
10	None	Nanofluid	84±7	-
11	None	Nanofluid	-	52±3 [†]
12	None	Pure Water	75±5	72±7

As expected based on the work of Liaw and Dhir (1989), the oxidation reduced the advancing contact angle. Figure 42 shows the contact angle on an unoxidized surface (left) and a well oxidized surface (right), both prior to the boiling run. There was

however some variation in the contact angle measurements. In particular, Trial 6 had an unexplainably large contact angle prior to the experiment. The reason(s) for this remain undetermined. However, its CHF enhancement (discussed below) is in line with expectations given its level of oxidation. Table 9 also shows that the contact angle prior to the experiment varied considerably for the four unoxidized surfaces. This may be due to the cleaning technique which involved dilute nitric acid, which contains a considerable amount of water that could quickly produce some oxidation. However, as will be noted in the results section below, the unoxidized surface had very repeatable CHF. The repeatability with which CHF could be measured on these surfaces may be due to the fact that the surface was oxidized by the time it approached CHF. As Tachibana et al. (1967) observed, a native oxide may develop during the experiment. They believed that this native oxide growth may be responsible for the high CHF observed with aluminum. For this reason, the post-CHF contact angle was measured in this study for a number of trials to estimate the contact angle just prior to CHF. The unoxidized surfaces were clearly affected by the boiling process as seen in Table 9.



Fig. 42. Photographs of the advancing contact angle on polished copper (left) and copper oxide (right).

Boiling curves that illustrate the effect of surface oxidation are shown in Fig. 43, where the working fluid was pure water. No effect of oxidation was discernable in the nucleate boiling regime due to scatter in the data. Oxidation, however, tended to increase CHF. This confirms the results of Liaw and Dhir (1989). For this study, the baseline unoxidized surface was run four times with pure water and CHF was repeatedly measured to be 61 ± 1 W/cm². The medium/light oxidized surface did not have the enhancement one might expect. Noting Table 9, its contact angle was actually higher than the lightly oxidized surface. This information could perhaps have been used to predict its anomalously low CHF. Figure 44 shows the CHF enhancement versus the advancing contact angle, as measured before and after the boiling experiment, and the trend is clear: lower contact angle (i.e., oxidation) increases CHF. The well oxidized surface had 141% the CHF of the baseline surface. These results were in good agreement with those of Liaw and Dhir (1989), who measured the static contact angle and observed up to ~90% enhancement.

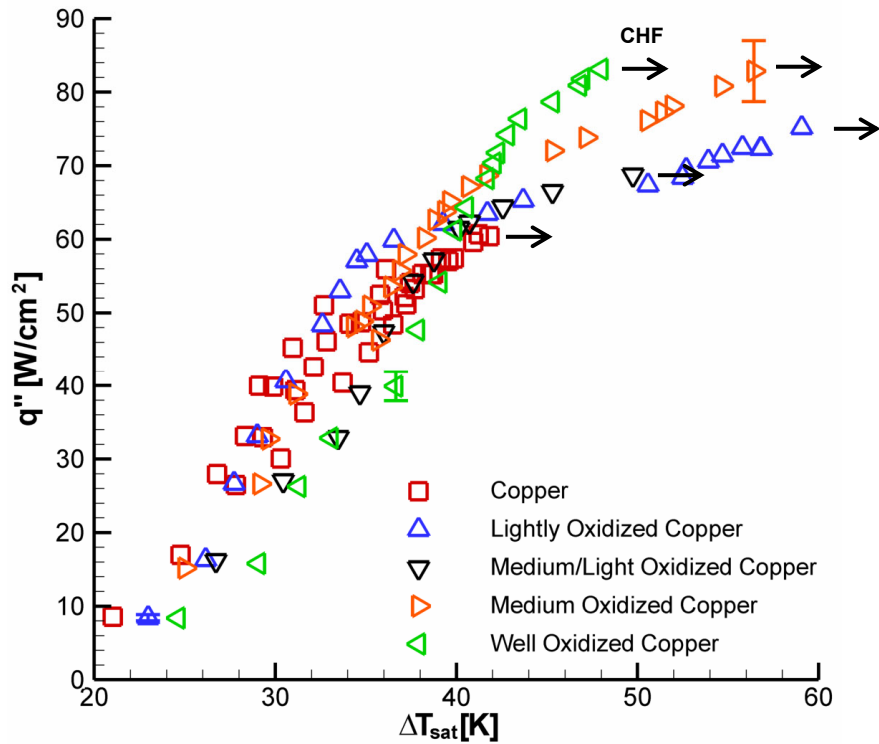


Fig. 43. Steady-state boiling curves ($T_{sat} = 29.8\text{ }^{\circ}\text{C}$, $T_{bulk} = 29.3\text{ }^{\circ}\text{C}$) illustrating the effect of surface oxidation.

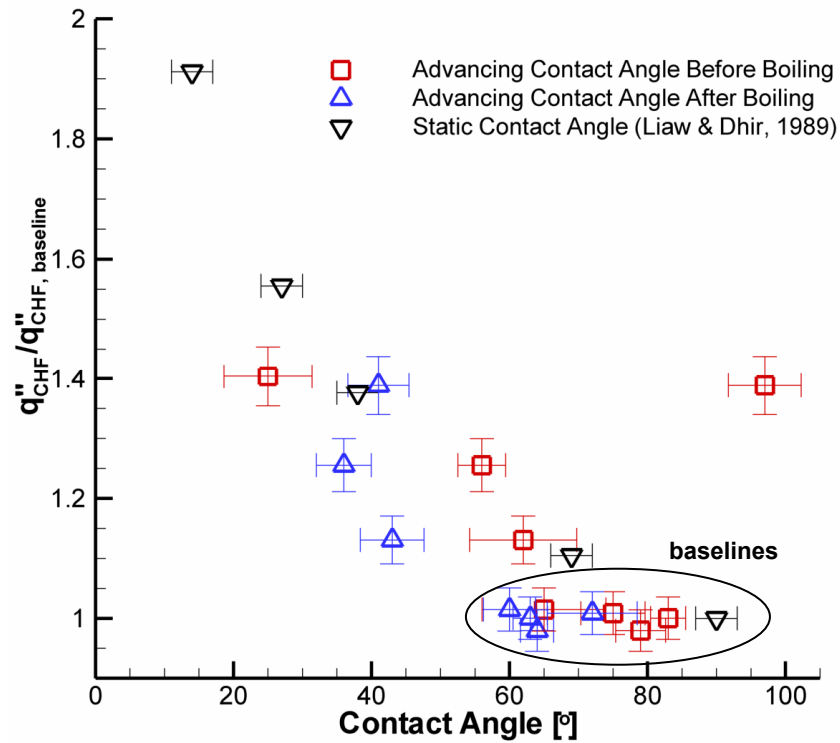


Fig. 44. CHF as a function of advancing contact angle for pure water on copper and copper oxide. Error bars represent standard deviation estimates.

Alumina/water nanofluid was then used as the working fluid for the unoxidized surface as well as the well oxidized surface. Boiling curves that illustrate the effect of the nanofluid are shown in Fig. 45. In both cases, nanofluid decreased CHF: by 22% for the oxidized surface and 13% for the unoxidized surface. Initially, these results were unexpected since nanofluids are known to improve surface wetting (Kim et al., 2006a), which tends to increase CHF. Furthermore, note that with the easily wetted copper oxide CHF was more degraded than with the less wettable unoxidized surface. This indicates that an increase in CHF due to improved wettability may be negated by another mechanism such as fouling. Each nanofluid test was immediately repeated, with similar results. The nanofluid was then removed from the chamber, the chamber was thoroughly cleaned and filled with pure water, and a final trial was run. This test yielded a CHF of 62 W/cm^2 compared to the previous three baseline CHF measurements of $61 \pm 1 \text{ W/cm}^2$. This provided a valuable check on the integrity of the experimental technique and illustrates the consistency of the CHF measurements.

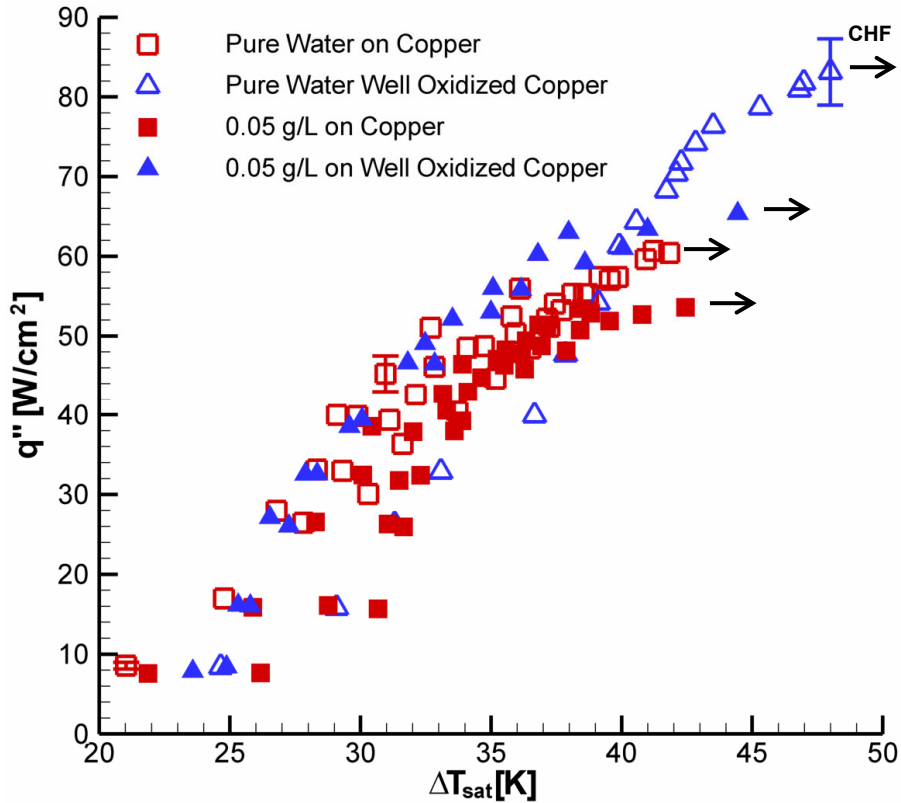


Fig. 45. Boiling curves ($T_{sat} = 29.8$ °C, $T_{bulk} = 29.3$ °C) illustrating the CHF degradation caused by the addition of nanofluid.

Another interesting aspect of these oxidation experiments to note is that the oxide provided a more controllable and significant CHF enhancement (see Fig. 46). The well oxidized surface increased CHF by 41% at a superheat of 49 K. In contrast, it required ~ 0.5 g/L of alumina to increase CHF by 37% on a plain surface, and this required ~ 20 K higher superheat. Thus, even with comparable heat fluxes, the higher superheat required with nanofluids makes their use significantly less desirable. Furthermore, the oxidation is a simple and controllable process that does not rely on expensive precursor materials.

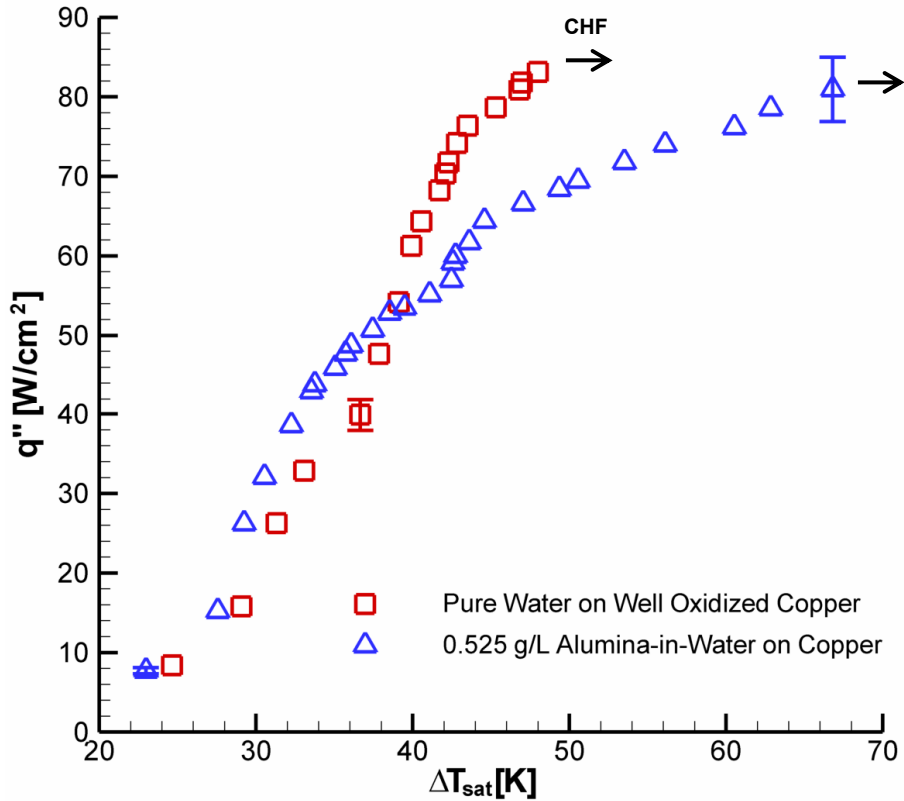


Fig. 46. Comparison of nanofluid and oxidation enhancement techniques.

5.3. Nanofluid's Contact Angle Modification

The data presented above, indicate that surface wettability is key in determining whether nanofluids enhance boiling heat transfer. To test the ability of nanofluid to improve surface wetting, the advancing contact angle of water based nanofluid (1.02 g/L) was compared to that of pure water on two different types of surfaces: copper and copper oxide.

5.3.1. Advancing Droplets on Copper

For the first run, pure water was advanced across a copper surface and the advancing contact angle was found to be $88.6 \pm 5.4^\circ$. Then, 1.02 g/L alumina-in-water was advanced across the surface four times. Nothing was done to the surface between

runs: the surface was only dried with nitrogen gas. The advancing contact angle is shown as a function of distance from the tip of the syringe in Fig. 47. The first time the nanofluid advanced across the surface, the advancing contact angle was indistinguishable from pure water. However, in subsequent trials, after the surface had been fouled by the nanoparticles, the advancing contact angle decreased. Since the advancing contact angle decreased with each run, it is posited that more particles were coating the surface during each advance. Furthermore, when the contact angle is plotted as a function of distance from the tip of the syringe, the area closest to the tip of the syringe is found to have the lowest contact angle, which increases almost linearly as the distance from the needle increases. One reason for this behavior may be that the area closest to the needle is exposed to every particle that exits the needle. Whereas, the area of the substrate that is farthest from the needle is only exposed to particles that are yet to deposit.

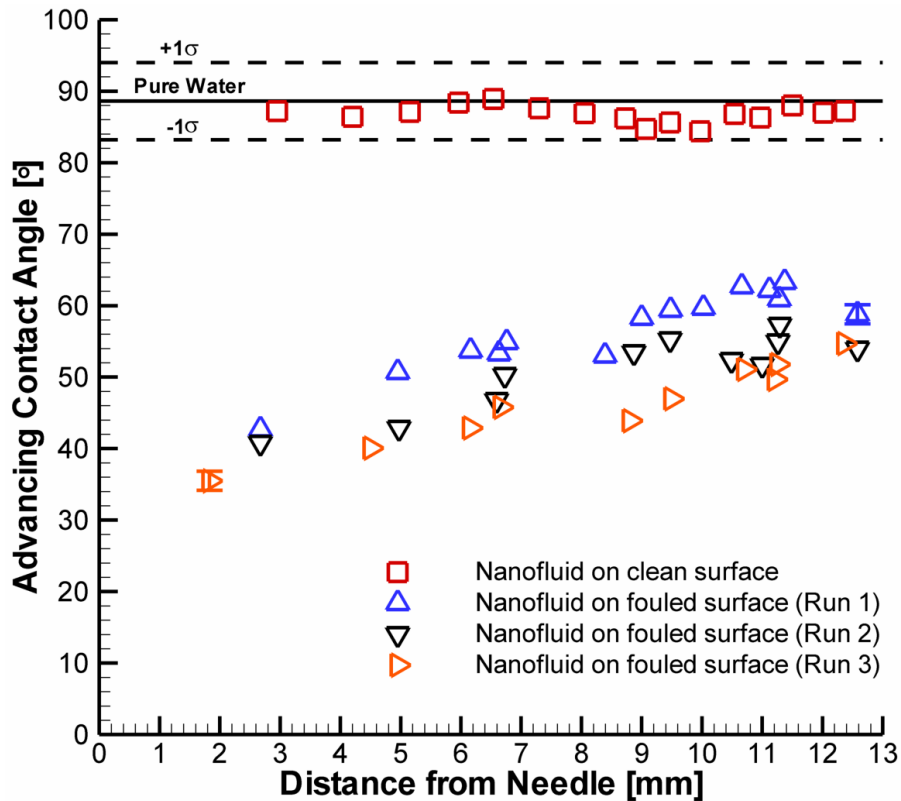


Fig. 47. Advancing contact angle of 1.02 g/L alumina-in-water nanofluid on copper. Pure water error bands show the standard deviation of a series of measurements, but the other error bars represent the standard deviation based on a single photograph.

Two months later, this experiment was repeated on a similarly prepared copper surface (see Fig. 48). While the magnitude of the contact angle was slightly different, the behavior was essentially the same: nanofluid on a clean surface was indistinguishable from pure water, but with each subsequent run the contact angle decreased. Still the near needle region had a lower contact angle than the region farthest from the needle, however the trend was not linear.

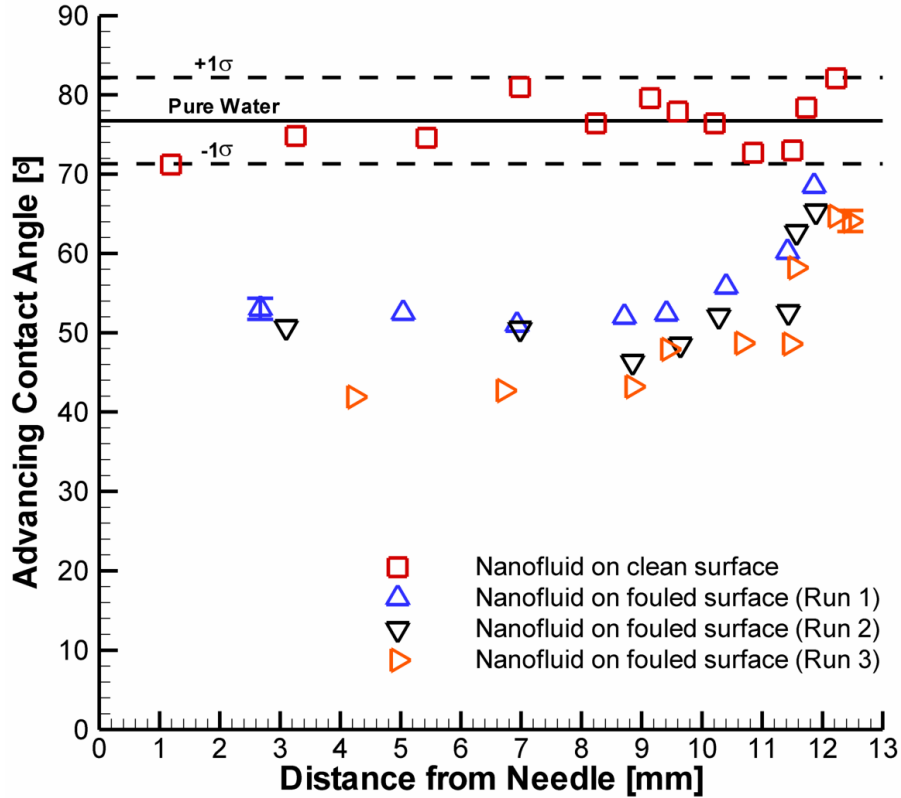


Fig. 48. Second trial for advancing contact angle of 1.02 g/L alumina-in-water nanofluid on copper. Pure water error bands show the standard deviation of a series of measurements, but the other error bars represent the standard deviation based on a single photograph.

Figures 47 and 48 clearly point to a possible boiling enhancement mechanism since they illustrate that nanofluid decreases the advancing contact angle only after dry out. Consider bubble growth and detachment (Fig. 49). As a bubble grows, the dry patch beneath it would grow as the liquid around the bubble's perimeter recedes (Fig. 49, left). The dryout process would leave nanoparticles on the surface of the heater. Then during detachment (Fig. 49, right), as the bubble is pinched off the surface, the dry patch is rewetted by advancing bulk liquid. However, the nanofouled surface will be more easily wetted as shown above in Figs. 47 and 48. The thinner wedge of liquid caused by the

smaller advancing contact angle would improve heat transfer from the substrate through improved evaporation efficiency (Liaw & Dhir, 1989).

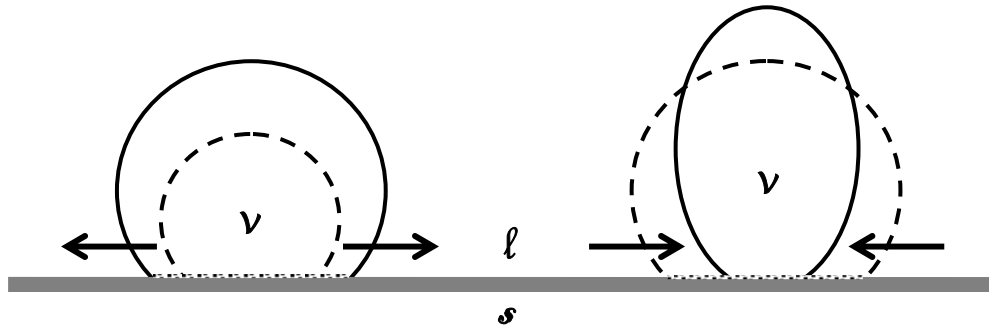


Fig. 49. Bubble growth leaving nanoparticles on the surface (left) and bubble detachment when liquid advances to cover the nanofouled dry patch (right).

5.3.2. Advancing Droplets on Copper Oxide

The boiling results presented in sections 5.1 and 5.2 demonstrated that highly wetting fluid/surface combinations were less likely to benefit from the use of nanofluid. Since nanofluid on nanofouled copper was found to reduce the advancing contact angle, the same advancing contact angle experiment was performed on a more easily wetted copper oxide surface.

The copper heating block was oxidized as described in Chapter 3 (see Table 5, medium oxidation). For the first run, pure water was advanced across a copper surface and the advancing contact angle was found to be $41.2 \pm 4.8^\circ$. Then, 1.02 g/L alumina-in-water was advanced across the surface four times (see Fig. 50). Again, the nanofluid only reduced the advancing contact angle on the nanofouled surface. However, since the contact angle of pure water on oxide is lower than on unoxidized copper, the effect of the nanofluid was reduced. On the oxidized surface the angle was only reduced $\sim 10 - 15^\circ$. This is consistent with the enhancement mechanism and the boiling results discussed above. With highly wetting fluid/surface combinations, the advancing contact angle is

reduced less by the nanofouling. The lower reduction in contact angle would decrease the enhancement in evaporation seen during rewetting. This results in less CHF enhancement with highly wetting fluid/surface combinations.

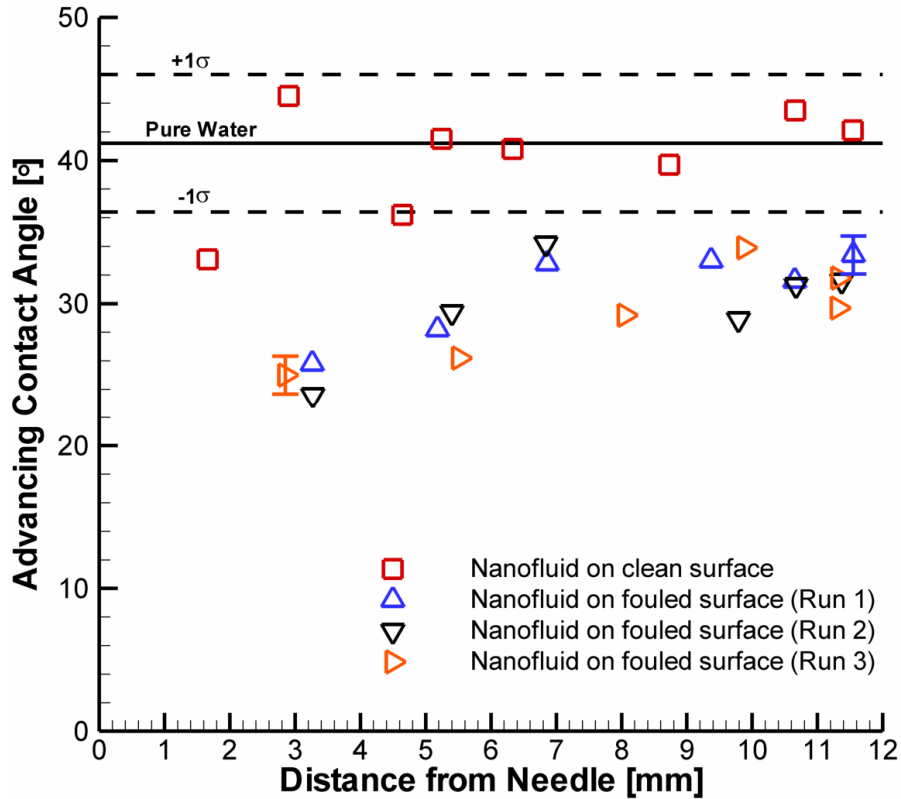


Fig. 50. Advancing contact angle of 1.02 g/L alumina-in-water nanofluid on copper oxide. Pure water error bands show the standard deviation of a series of measurements, but the other error bars represent the standard deviation based on a single photograph.

5.4. Spray Cooling with Nanofluids

While boiling with nanofluids is complicated and still not completely understood, there appears to be some hope of enhancing heat transfer, most likely through a modest increase in CHF. Like boiling, a spray cooled surface will also be affected by the wetting characteristics of the working fluid (Sehmbey et al., 1994). In addition to the processes such as bubble growth and liquid rewetting that affect boiling, spray cooling is complicated by the addition of droplet evaporation. Droplets with smaller contact angles

will have a decreased droplet thickness, which enhances heat conduction and thus the evaporation rate (Chandra et al., 1996). Therefore, there is reason to believe that nanofluids may also enhance spray cooling heat transfer.

5.4.1. Spray Cooling Curves

Alumina-in-ethanol nanofluids were sprayed at a glass substrate with differential nozzle pressures of 69 kPa (10 psig) and 345 kPa (50 psig). Note that 69 kPa did not produce a fully atomized spray and was more jet like, but this lower pressure is more typical of real world applications. The 69 kPa spray cooling curves are shown in Fig. 51. There was no effect of nanofluids at these concentrations. Both the single-phase and two-phase regimes were unaffected, as was the CHF.

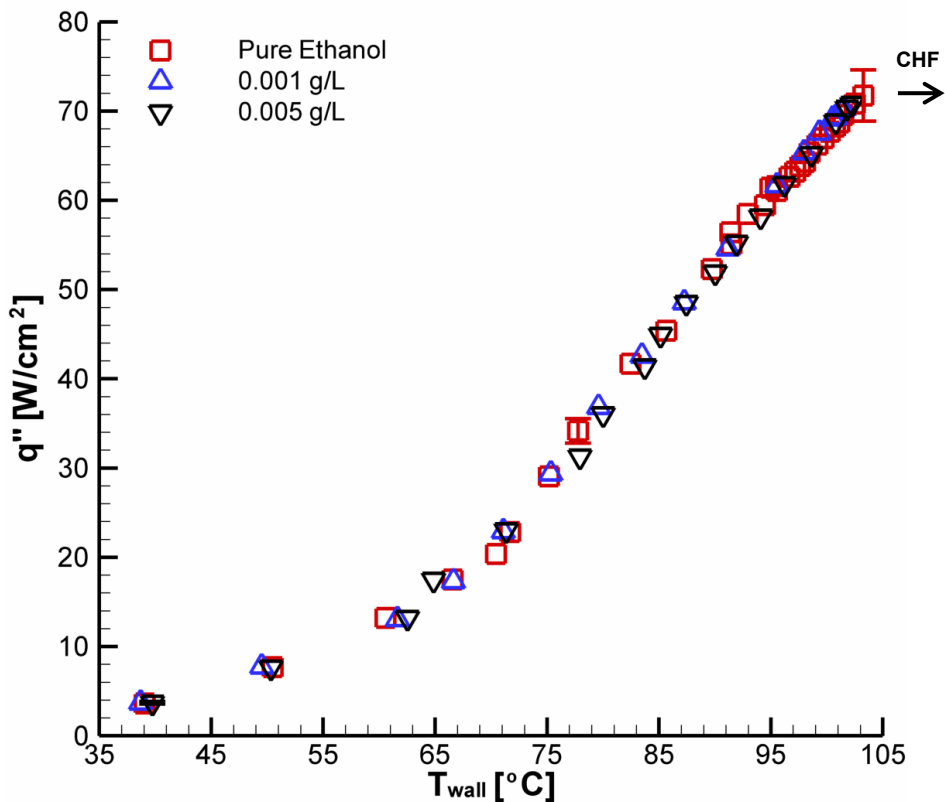


Fig. 51. Spray cooling curves for subcooled ($T_{sat} = 51.7$ °C, $T_{spray} = 30.5$ °C) ethanol sprays ($\Delta P=69$ kPa) at various alumina nanoparticle concentrations.

The results of the 345 kPa tests are shown in Fig. 52. Again, low concentrations had no effect on performance. However, 0.5 g/L resulted in a significant degradation in all regions of the spray cooling curve. The CHF decreased by 49%. This disappointing result was due to partial clogging of the spray nozzle, which was visually observed to drastically alter the spray cone's shape.[†] Two additional aspects of the data point to partial clogging of the spray. First, note that this spray cooling curve has a clear transition from the single-phase to two-phase regimes around 70°C. Whereas, the pure fluid and low concentration sprays remain single-phase because the spray velocity was too great to allow for the development of superheated liquid. The appearance of the two-phase regime is indicative of lower flow rate. Also, note that the shape of this curve is qualitatively similar to the lower flow rate, 69 kPa, data presented above. Second, the volume flow rate of the spray was measured upstream with a digital turbine flow meter. In the 0.5 g/L test, the volume flow rate decreased from 52 mL/min to 18 mL/min.

The nozzle clogging was likely due to particle deposition on the brass nozzle. As provided by the manufacturer, the alumina particles were ~45 nm in diameter (Nanophase Technologies Corporation, 2003). At this scale, the particles should easily pass through the nozzle. However, nanoparticles are known to be unstable in the vapor phase (Friedlander, 2000), and therefore are likely to agglomerate in a spray cooled system. By design, the spray nozzle creates many fine droplets that easily evaporate. If the particles lose their suspension properties in the vapor phase, then agglomerates would be created at every point that experiences droplet evaporation. This mechanism could have been

[†] The possibility that poor spray atomization was due to an increase in viscosity was considered. However, since the nanoparticle's volume fraction was of order 10^{-5} , the viscosity increase was expected to be of order 10^{-4} (see Fig. 53), which should have a negligible effect on atomization.

responsible for clogging the outside of the nozzle, or the inside could have been clogged by simple particle deposition in the liquid phase.

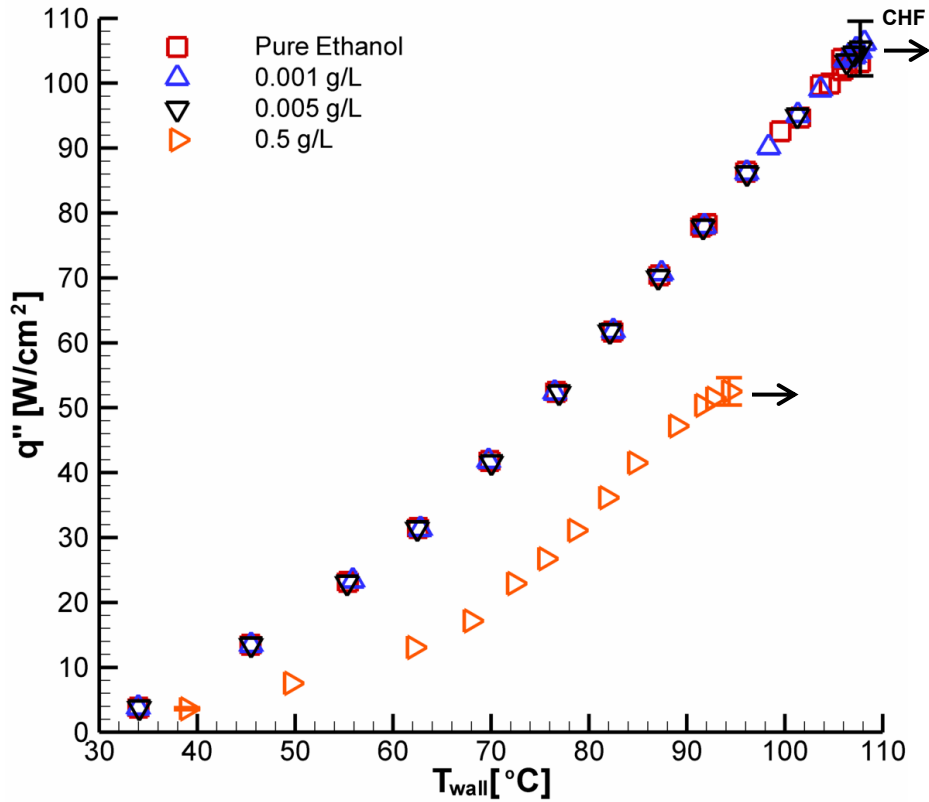


Fig. 52. Spray cooling curves for subcooled ($T_{sat} = 51.7$ °C, $T_{spray} = 30.5$ °C) ethanol sprays ($\Delta P=345$ kPa) at various alumina nanoparticle concentrations.

5.4.2. Scaling Analysis

Given the poor initial results with spray cooling nanofluids, the prospect of enhancing spray cooling with nanofluids was reconsidered. Recall that Shedd and Pautsch (2005) have shown that spray cooling is essentially a single-phase phenomenon. This was confirmed for the high pressure/flow rate ($\Delta P=345$ kPa) data presented above. Therefore, the addition of nucleation sites may be of little importance. The dominant factor known to affect spray cooling is volumetric flow flux (Estes & Mudawar, 1995), and flow rate is clearly impacted by nozzle plugging and increases in viscosity.

Along with the anomalous increase in thermal conductivity (recall Fig. 38) nanofluids exhibit a large increase in viscosity. In most cases, the viscosity increases faster than the thermal conductivity and in some extreme cases the viscosity has been found to increase by over 100%. A survey of reported viscosity increases is shown as a function of particle volume fraction in Fig. 53. Even excluding the study by Pak and Cho (1998), this viscosity increase is significant.

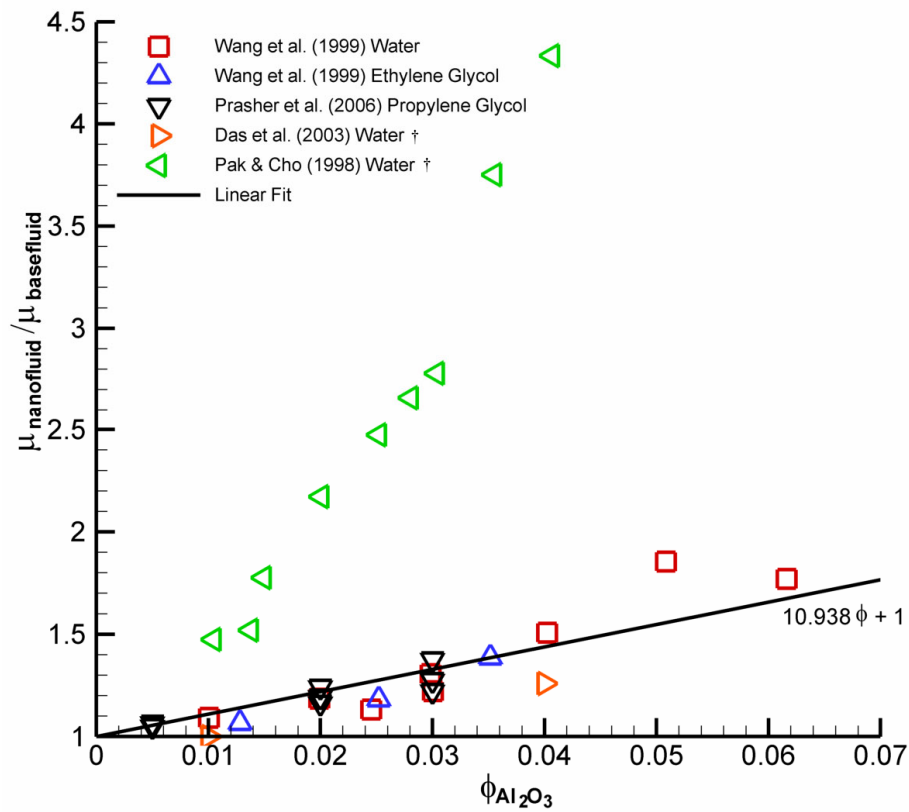


Fig. 53. Relative viscosity increase for alumina nanofluids with linear fit that excludes the Pak & Cho data. † These authors report viscosity varying as a function of shear rate. Their results at the highest shear rates were used. Note that the viscosity increases are greater at lower shear rates.

To get a sense of how this would affect spray cooling, consider the single-phase impinging jet correlation of Fabbri, Jiang, and Dhir (2003):

$$Nu = 0.055Re_{d_n}^{0.81}Pr^{0.43} \left[1 + 0.0385 \left(\frac{D_{eq}}{d_n} \right)^{0.82} \right]^{-4.48} \quad (41)$$

The heat transfer coefficient can be seen to be proportional to $k^{0.57}$ and $\mu^{-0.38}$. Then, using the linear approximations to the thermal conductivity and viscosity increases from Figs. 38 and 53, respectively, the relative heat transfer coefficient can be calculated. The degradation in heat transfer coefficient based on this scaling analysis is shown in Fig. 54. The increase in viscosity is enough to completely offset the thermal conductivity enhancement and result in a slight decrease in heat transfer coefficient as the volume fraction of nanoparticles is increased. This indicates that using higher concentrations of nanofluid in a jet or spray system would likely cause decreased thermal performance, even if nozzle clogging could be overcome. Also note that this degradation would be even worse in some instances if the viscosity increase was even larger as in Pak and Cho's (1998) study.

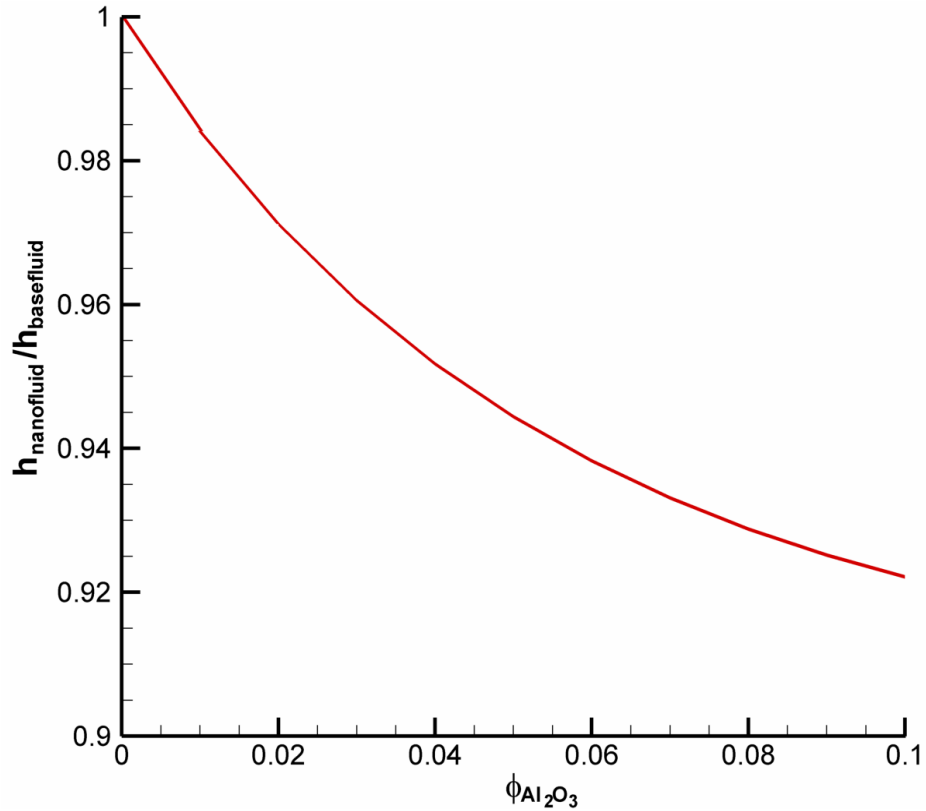


Fig. 54. Relative heat transfer coefficient for jet impingement determined through scaling analysis as a function of nanoparticle volume fraction.

5.5. Summary of Nanofluid Research

Nanofluid boiling was experimentally investigated with alumina-in-water and alumina-in-ethanol nanofluids. Four different types of surfaces were used to study the surface wetting aspect of nanofluid boiling. The following major conclusions were made:

- Ethanol based nanofluids were found to have no effect on glass or gold over the range of concentrations used.
- Water based nanofluids increased CHF modestly on copper but at higher particle concentrations than some reports in the literature.

- Dilute water based nanofluids could degrade performance. This degradation was larger with a copper oxide surface than with pure copper.
- Oxidizing a copper surface and using pure water proved more effective at enhancing CHF than using nanofluids because of the high superheat required for nanofluid CHF enhancement.
- Ethanol based nanofluids could increase CHF on a copper heater but greater concentrations were required than with water and the CHF enhancement was more modest.
- All the above results indicate nanofluid CHF enhancement is strongly linked to poor wettability. When surfaces are easily wetted by base fluid, nanofluids are less useful and sometimes more degrading.
- The advancing contact angle of alumina-in-water nanofluid was found to be indistinguishable from pure water on clean surfaces (both copper and copper oxide). However, after the surface had been coated with nanoparticles, the advancing contact angle of nanofluids was reduced. This lead to a possible boiling enhancement mechanism in which dryout during bubble growth leaves particles on the surface, which reduces the contact angle during the subsequent rewetting process. The lower contact angle (and thinner liquid wedge) then enhances evaporation.
- The contact angle reduction measured for nanofouled surfaces was smaller for highly wetting fluid/surface combinations such as copper oxide. Since contact angle is known to affect CHF, the lower contact angle reduction is likely

responsible for the poorer boiling enhancements observed with highly wetting fluid/surface combinations.

Nanofluid spray cooling was also experimentally investigated and was found to be detrimental to thermal performance. In one case, CHF was found to decrease by 49% due to a significant deterioration of spray atomization (perhaps due to a partial plugging of the nozzle). This could be due to the instability of the nanoparticles in the vapor phase. Furthermore, a scaling analysis was performed to illustrate that the expected enhancement due to an improvement in thermal conductivity is negated by the dramatic rise in viscosity.

The observed experimental results can be explained by considering the modification of a solid surface. Given the uncertainty involved with nanofluids due to agglomeration, settling, and fouling; a more appropriate method of spray cooling enhancement would be direct surface modification such as the addition of microstructures or fins.

CHAPTER 6. EXTENDED STRUCTURE SPRAY COOLING

Review of the recent literature suggests that surface modification, specifically straight channels, provides a significant enhancement in spray cooling heat transfer. However, the mechanisms behind the enhancement are not yet fully understood. This chapter presents the results of a systematic study of the spray cooling of high aspect ratio open microchannels. The channel depth was varied to explore the relative spray utilization, which was investigated in detail. Furthermore, a one-dimensional fin analysis was developed to interpret the results.

6.1. Results of Spray Cooling High Aspect Ratio Open Microchannels

Spray cooling curves for the six test surfaces at three nozzle pressures are shown in Figs. 55 – 57. A significant performance enhancement over the flat surface is observed for each of the five enhanced surfaces at all nozzle pressures. As expected, increasing the nozzle pressure (and mass flux) resulted in higher heat transfer. This is in agreement with the literature (e.g., Estes & Mudawar, 1995a; Pautsch & Shedd, 2005). Furthermore, there were also distinctly different trends in the single-phase and two-phase regimes, where there is a sharp increase in heat transfer. In particular, the finned surfaces showed a significant enhancement in the total heat flux once two-phase effects became dominant.

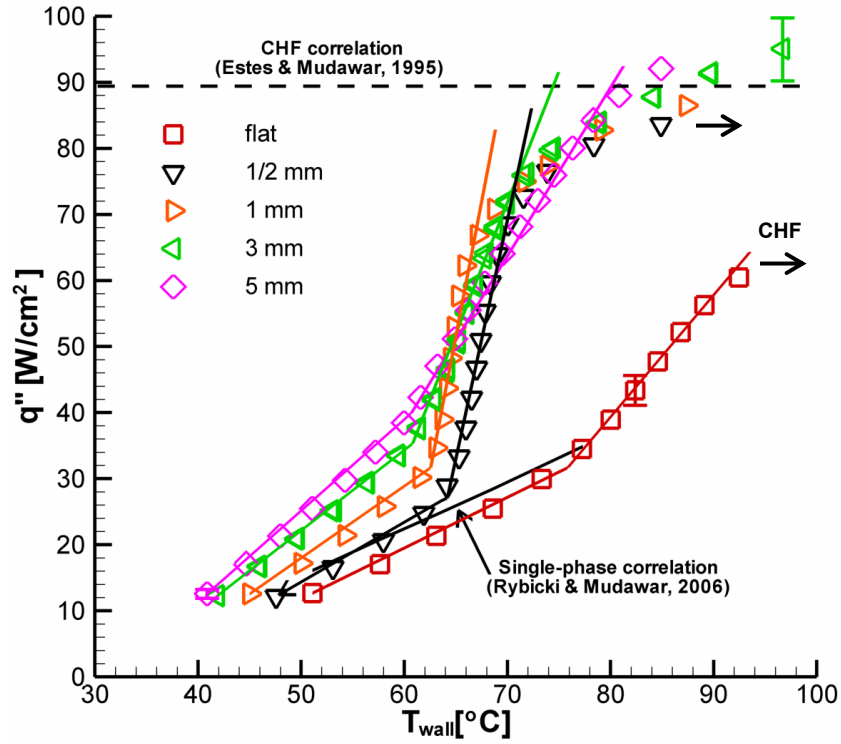


Fig. 55. Spray cooling curves for open microchannel surfaces at nozzle pressure of 138 kPa (20 psig).

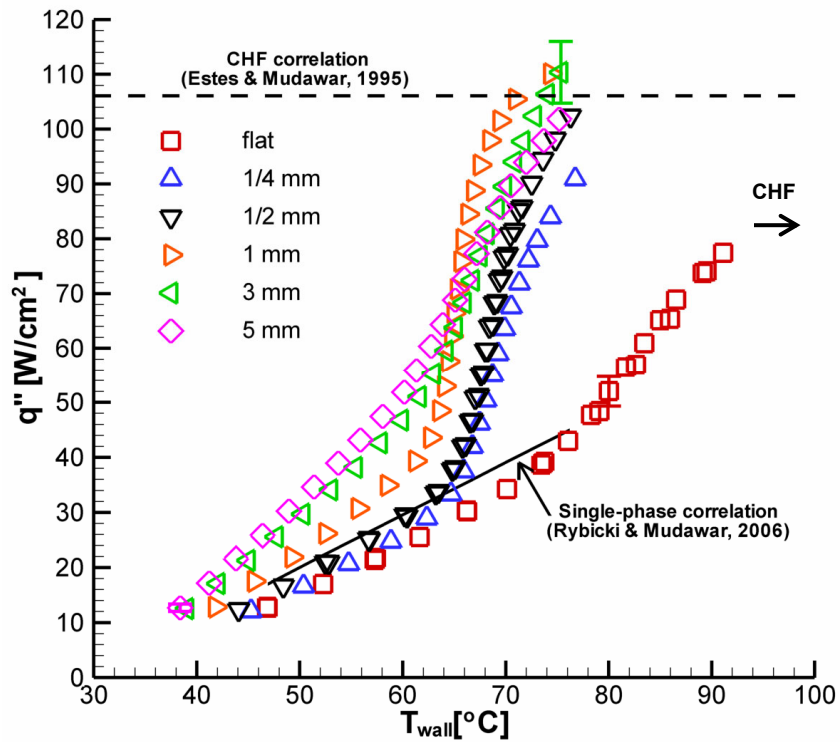


Fig. 56. Spray cooling curves for open microchannel surfaces at nozzle pressure of 276 kPa (40 psig).

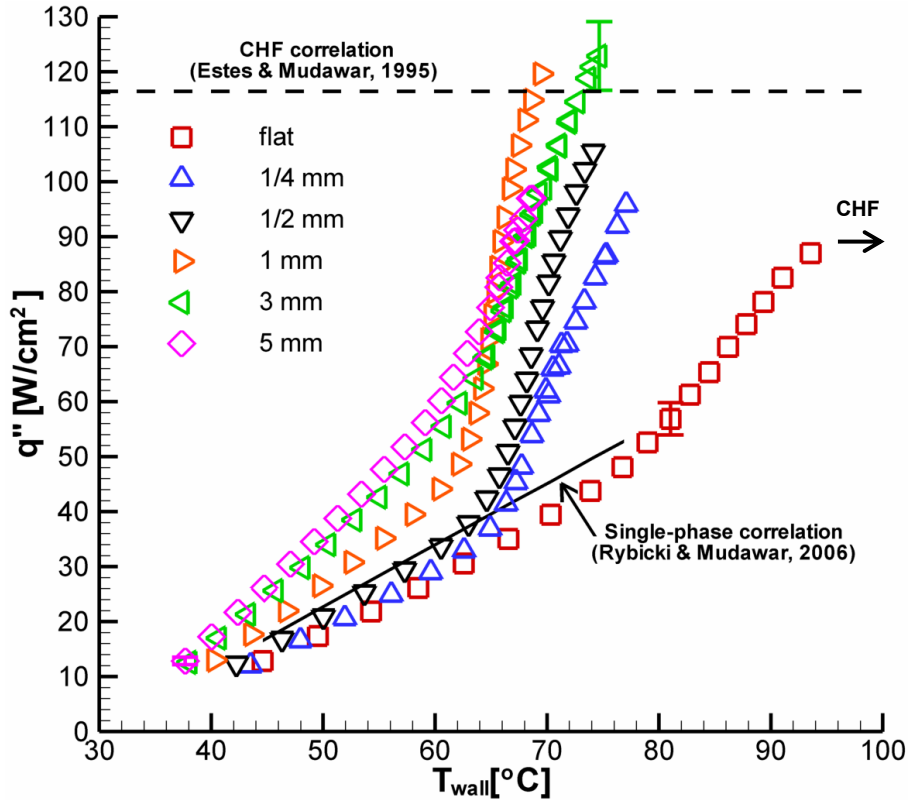


Fig. 57. Spray cooling curves for open microchannel surfaces at nozzle pressure of 413 kPa (60 psig).

6.1.1. Single-Phase Results

The single-phase regime is defined as the linear portion of the cooling curve where the wall temperature is not high enough to cause any significant amount of boiling, which would cause the heat transfer coefficient to increase dramatically as it does in nucleate pool boiling. The bare surface performance was typical and a comparison with the single-phase correlation of Rybicki and Mudawar (2006) is shown on Figs. 55 – 57. This correlation was developed from two data sets using PF-5050 and water, and the claimed error in the correlation is 13.1%. The current data is found to lie just outside of this expected error with a mean deviation of -15% with respect to the predicted value.

The slight deviation from linearity in the present data that was observed in the “single-phase” regime is due to at least some evaporation from the top of the liquid film. Note that the relatively low temperature of the incoming spray, spray chamber, and coiling coil promote evaporation from the wall even when the wall temperature is below the saturation temperature (56°C). This is due to the relatively higher vapor pressure of the warm liquid on the heater. While the evaporative effect is significant, as will be discussed below in greater detail, the heat transfer coefficient is nearly constant in this region of the spray cooling curve and drastically different than in the two-phase or boiling regime.

The effect of nozzle pressure difference on heat transfer over the range of conditions explored is illustrated on Fig. 58. As expected, a larger ΔP resulted in significant improvement in heat transfer, most likely due to the higher mass flow rate, finer droplets, and higher droplet velocity that accompany an increasing ΔP .

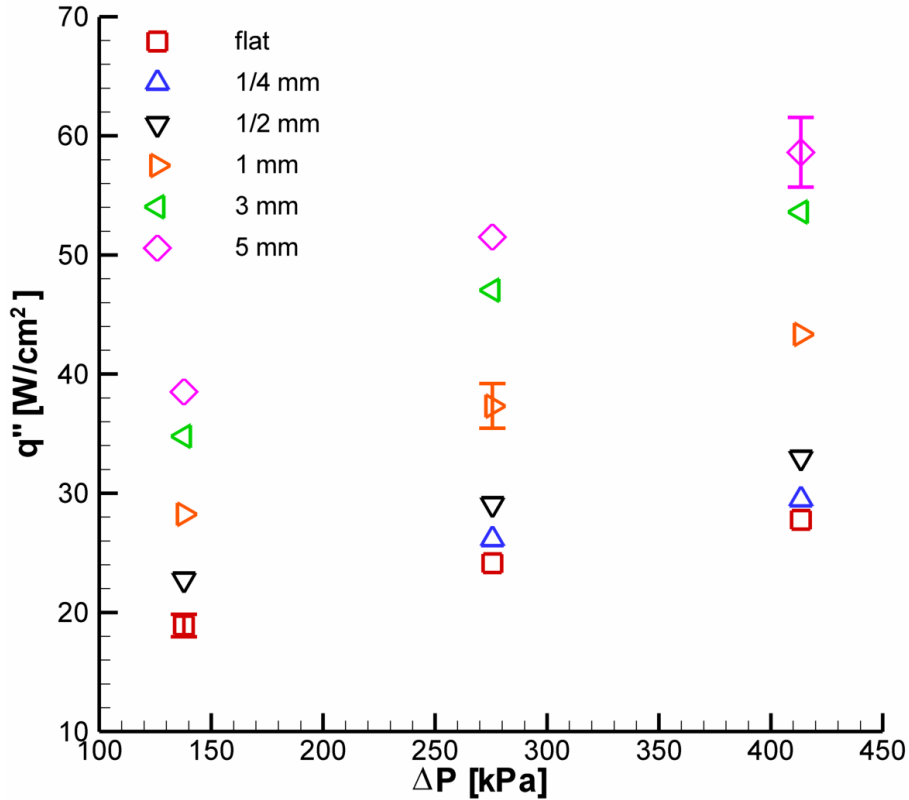


Fig. 58. Heat flux as a function of nozzle pressure difference for $T_{\text{wall}} = 60^\circ\text{C}$ (similar results are obtained at other wall temperatures). Heat fluxes are based on the 2 cm^2 projected area.

Longer fins always provided more enhancement than shorter ones as illustrated in Figs. 55 – 57. The relative performance enhancement as a function of fin length is shown on Fig. 59. While the total surface area increases linearly with fin length, the heat transfer enhancement appears to be asymptotically approaching an optimum value. The dependence of heat transfer enhancement on fin length is rather insensitive to changes in flow rate and well within the experimental uncertainty. The results observed in the single-phase regime were due to a number of competing mechanisms. Adding fin length not only increased the wetted area, but also increased the amount of fluid incident on the surface (note Table 8). These two positive effects were offset by the addition of conduction resistance within the fin, less uniform distribution of liquid due to more

channeling, and heating of the fluid as it traveled down the fins (thus lower local ΔT near the bottoms of the fins). While longer fins showed improvement, the addition of conduction resistance should eventually decrease performance by adding a temperature drop between the base of the fins and the top of the fins where the liquid is the coolest.

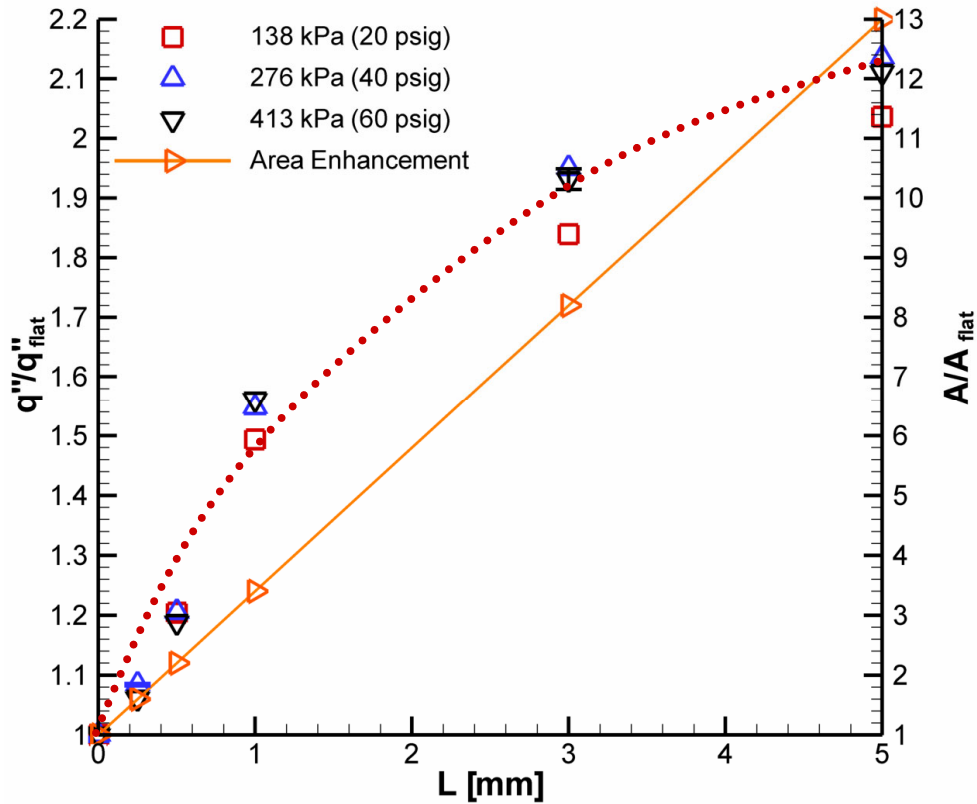


Fig. 59. Area and heat flux enhancement as a function of fin length for $T_{wall} = 60^{\circ}\text{C}$ (similar results are obtained at other wall temperatures). Heat fluxes are based on the 2 cm^2 projected area.

6.1.2. Two-Phase Results

In many spray cooling studies, heat transfer has been found to be primarily a single-phase phenomenon (Pautsch & Shedd, 2005). The supply of cold liquid is so high (in order to maximize heat transfer) that there is little time for the heater to increase the local liquid temperature. Liquid is swept away by fresh cold liquid before it can heat up enough to generate a bubble. This suppression of nucleation due to the convective effect

of liquid sweeping across a flat surface has also been observed in flow boiling by many researchers (Chen, 1966). As a result, very high wall temperatures are required to begin significant bubble nucleation. This phenomenon was also observed in this study—the flat surface remained essentially single-phase up to almost 20°C above the saturation temperature of 56°C.

The finned surfaces entered the two-phase regimes at temperatures closer to the saturation temperature (see Figs. 55 – 57 and Table 10). Four possible mechanisms responsible for this effect were considered:

- i) An increase in the number of potential nucleation sites due to increased area might result in increased ebullition, mixing, and latent heat contribution.
- ii) A longer residence time as liquid must travel down the fin and out of the channel before leaving the hot structure allows more energy to be transferred from the wall. This may create the superheated liquid needed for nucleation.
- iii) Channeling of the liquid by the fins would leave the inner channels with sufficient liquid but the outer channels partially starved. The liquid starved regions would more easily develop superheated liquid and begin boiling.
- iv) Conversely, liquid pooling may have occurred on portions of the fin that were shaded from the impinging droplets. These shaded regions would have seen no cool drops and only be cooled by preheated liquid draining from somewhere else. These regions might form thicker pools, allowing nucleation to occur more easily.

Table 10. Temperatures required for dominant two-phase effects.

Fin Length [mm]	Approx. Temp. at Onset of Boiling [°C]
0	77
0.25	66
0.5	65
1	63
3	62
5	61

One aspect of the boiling onset data is particularly revealing: the sharp transition to the two-phase regime occurred at a temperature that was independent of nozzle pressure difference. The liquid velocity in the channels (or on the flat surface) would scale with the pressure. This indicates that the onset of two-phase effects (which is almost entirely responsible for the observed enhancement) is not due to an increase in liquid velocity. This supports enhancement mechanisms that are not based on flow rate, such as mechanisms iii and iv based on dryout and pooling, respectively.

6.1.3. Critical Heat Flux Results

Although CHF was observed for the flat surface, CHF was not reached for most of the finned surfaces due to the heating block reaching temperatures greater than the safe temperature limit of the test apparatus. The correlation of Estes and Mudawar (1995) for spray cooling CHF is indicated in Figs. 55 – 57, and is shown to consistently overpredict the observed CHF magnitude. However, the uncertainty in their correlation was $\pm 30\%$.

Another interesting aspect of the $\Delta P = 1.36$ atm (20 psig) tests was the delayed transition toward CHF. The finned surfaces began to show a decrease in their heat transfer coefficients around 71°C even though CHF is not reached until over 90°C , indicating that dryout occurred gradually. This may have been due to channeling of the

spray, which allowed the outer channels with less liquid to begin drying out before the fluid rich center channels.

6.2. Spray Efficiency Improvement

Calculating the spray efficiency as defined in Eq. 42 yields further support for the notion of an increasing liquid temperature.

$$\eta = \frac{q}{\dot{m}[c_{p,l}(T_{wall} - T_{spray}) + h_{fg}]} \quad (42)$$

The latent heat term is included in the denominator of Eq. 42 despite its application in the single-phase regime because evaporation occurs when the environment surrounding the heater is at a lower temperature than the heater itself. In fact, during the experiment, condensation was observed on the 30°C copper coiling coil at all reported wall temperatures. Additionally, a spray efficiency calculation that excludes the latent heat term results in efficiencies greater than 100% for much of the data, indicating the importance of the latent heat term. The spray efficiency as defined in Eq. 42 is shown as a function of fin length in Fig. 60. Lower nozzle pressure resulted in a higher spray efficiency most likely due to a reduced impact velocity generating an increased residence time of the droplets on the surface. This increased the evaporative heat transfer despite any reduction in the convective heat transfer due to lower droplet velocity. The spray efficiency also shows the same trend at a wall temperature of 50°C as at 60°C, which further supports the notion that boiling had yet to begin, even though the wall temperature had elevated past the saturation temperature of 56°C. Furthermore, the spray efficiency, like the heat transfer enhancement, is seen to asymptotically approach an optimum for a given wall temperature and nozzle pressure difference.

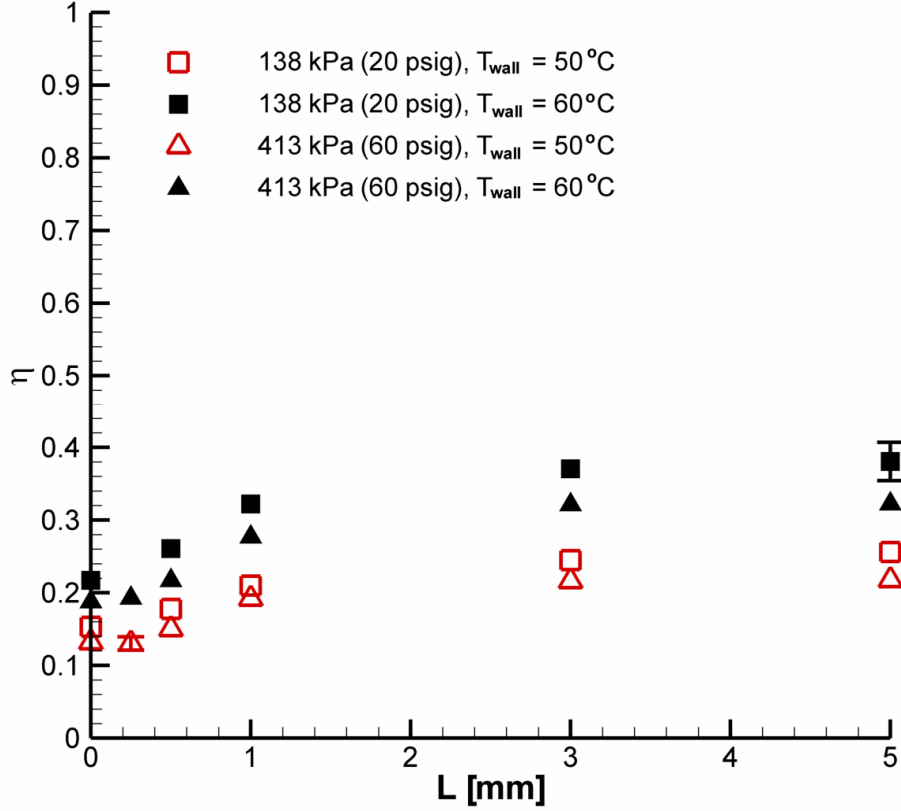


Fig. 60. Spray efficiency as a function of fin length in the “single-phase” regime.

Greater insight into the significance of the two-phase regime can also be gained by considering the spray efficiency. Typically, the spray efficiency is defined as in Eq. 43, however this makes no allowance for superheating of the liquid or vapor.

$$\eta = \frac{q}{\dot{m}[c_{p,l}(T_{sat} - T_{spray}) + h_{fg}]} \quad (43)$$

The experimental data of this study indicate significant vapor production within the confines of the microchannels, and this vapor may have been heated by dry portions of the channels as it escapes. A more appropriate definition of spray efficiency would include the sensible heat required to increase the vapor temperature from the saturation temperature to the wall temperature as follows.

$$\eta' = \frac{q}{\dot{m}[c_{p,l}(T_{sat} - T_{spray}) + c_{p,v}(T_{wall} - T_{sat}) + h_{fg}]} \quad (44)$$

The vapor specific heat was estimated using the Yoneda (1979) method for organic compounds in the ideal gas state (see Appendix D for details on this calculation). Also note that the liquid and vapor specific heats are similar ($c_{p,l} = 1102 \text{ J/kg}\cdot\text{K}$, $c_{p,v} = 912 \text{ J/kg}\cdot\text{K}$ at T_{sat}), so the state of the fluid being superheated is of little importance as long as a superheating term is included in the efficiency definition.

The spray efficiencies are shown as a function of temperature in Figs. 61 - 63. The mass flow rates used are based on the flow incident on the top surface of the finned structure (see Table 8). While the spray efficiencies of the flat surface are characteristically low, the efficiencies with microchannels appear to asymptotically approach the theoretical limit of unity. This trend is particularly evident in the 138 kPa data, while data at higher temperatures is required at higher nozzle pressure differences. In the single-phase regime, spray efficiencies are low and monotonically increase along with fin length. The onset of boiling corresponds to a large increase in the spray efficiency and since the onset occurs at different temperatures for different channel heights, the optimum fin length varies with temperature.

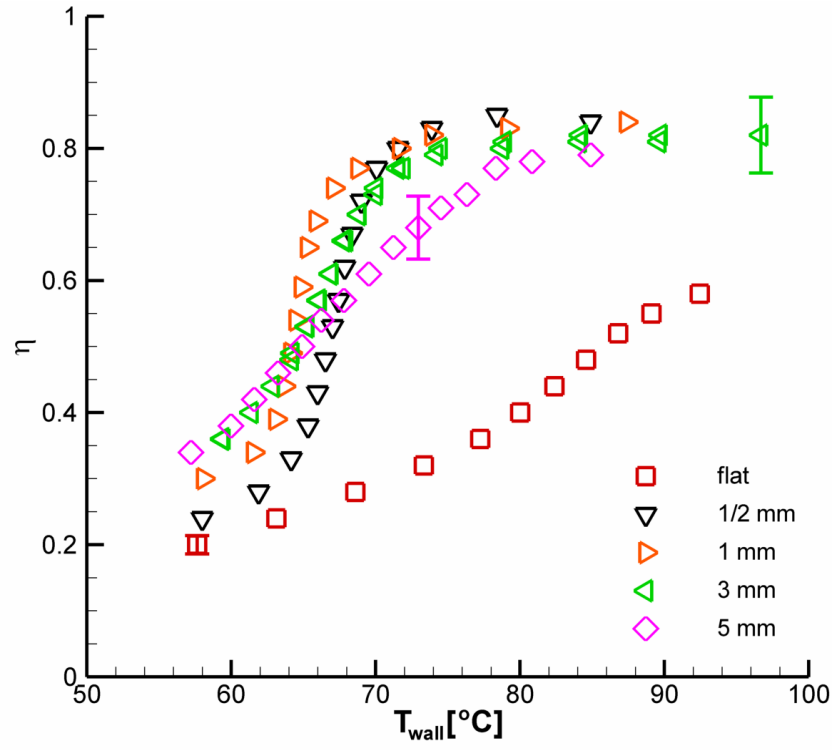


Fig. 61. Spray efficiency as a function of wall temperature for 138 kPa (20 psig) nozzle pressure difference.

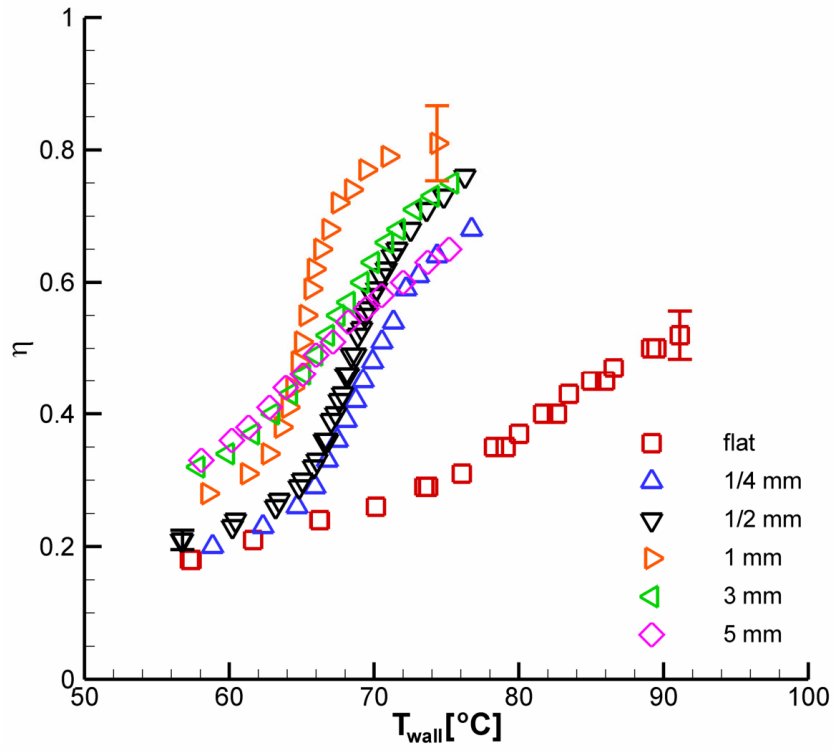


Fig. 62. Spray efficiency as a function of wall temperature for 276 kPa (40 psig) nozzle pressure difference.

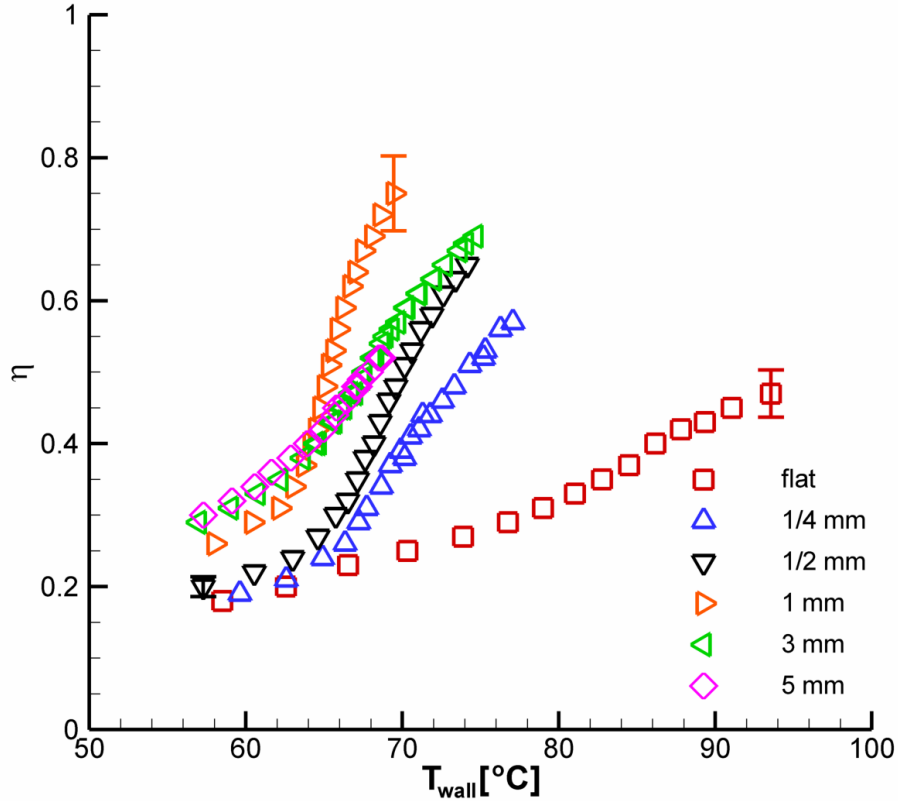


Fig. 63. Spray efficiency as a function of wall temperature for 413 kPa (60 psig) nozzle pressure difference.

These findings indicate some important results. The efficiencies of the finned surfaces for the 138 kPa (20 psig) pressure difference collapse onto a single curve as CHF is approached, and this single curve indicates almost total evaporation of the incident spray. By channeling the spray and forcing liquid to travel down the fins and through the microchannels, it has sufficient residence time to heat up to the wall temperature in the single-phase regime, or to the saturation temperature and completely evaporate in the two-phase regime. The very high spray efficiencies observed in this study are likely due to the small scale of the microchannels along with the relative sparseness of the spray. It may likely be confirmed that given a greater flow rate, the heat transfer could be improved at the expense of a decreased spray efficiency as shown

by Pautsch and Shedd (2005) with flat surfaces and Silk et al. (2004, 2005, 2006) with enhanced surfaces. However, spraying microchannels with a sparse spray may be one way of improving thermal performance without merely increasing the mass flow rate, which can be expensive in terms of pump power, cost, and weight.

6.3. One-Dimensional Model for Single-Phase Heat Transfer

A simple, one-dimensional fin model is proposed to gain better understanding of the underlying mechanisms.

6.3.1. Model Development

The heat transfer coefficient on a typical fin was determined by solving the convection tip fin equation (Incropera & DeWitt, 2002), Eq. 45, using one of two different values for the fin heat transfer.

$$q_{sides+tip} = \sqrt{hP_f k A_c} \theta_w \frac{\sinh(mL) + \frac{h}{mk} \cosh(mL)}{\cosh(mL) + \frac{h}{mk} \sinh(mL)} \quad (45)$$

- 1) In the first case, the heat transfer from the bottom of the channels was neglected. The entire heat transfer observed in the experiment was then attributed to the sides and tip of the fin according to Eq. 46, where $n=17$ is the number of fins on the heat sink. Since heat transfer from the bottom of the channels was neglected, this method yielded an upper limit for the average heat transfer coefficient for the sides and tip.

$$\frac{q_{heatsink}}{n} = q_{sides+tip} \quad (46)$$

- 2) In the second case, the heat transfer from the bottom of the channels was assumed to be unchanged from the flat surface experimental result. Since the

model assumes the flat surface was impacted by fresh cold liquid (the liquid is actually pre-heated by the upstream area), the bottom surface heat transfer is overestimated yielding a lower limit for the heat transfer coefficient on the sides/tip. The average sides/tip heat transfer is then given by Eq. 47, where the 0.41 factor on the last term is required because the bottom surface has a total area of 0.81 cm² whereas the flat surface has an area of 2 cm².

$$\frac{q_{heatsink}}{n} = q_{sides+tip} + 0.41 \frac{q_{flat}}{n} \quad (47)$$

These two cases were used to determine the heat transfer coefficient with Eq. 45, which is then used to predict the temperature profile with Eq. 48 (Incropera & DeWitt, 2002).

$$\frac{\theta}{\theta_{wall}} = \frac{\cosh[m(L-x)] + \frac{h}{mk} \sinh[m(L-x)]}{\cosh(mL) + \frac{h}{mk} \sinh(mL)} \quad (48)$$

Note that while Figs. 55 - 57 show heat fluxes based on the 2 cm² projected area, the heat transfer coefficient discussed here is based on the wetted area.

6.3.2. Results and Implications

Figure 64 shows the lower and upper limit heat transfer coefficients (normalized by the bare surface heat transfer coefficient) calculated using the above method. The heat transfer coefficients are significantly lower than the bare surface heat transfer coefficient, which is expected since the enhancement in heat transfer observed with the channeled surfaces is not as great as the area enhancement (recall Fig. 59). Furthermore, both the lower and upper limits predict similar heat transfer coefficients for the sides/tip as the fins become long, indicating the decreasing significance of the troughs.

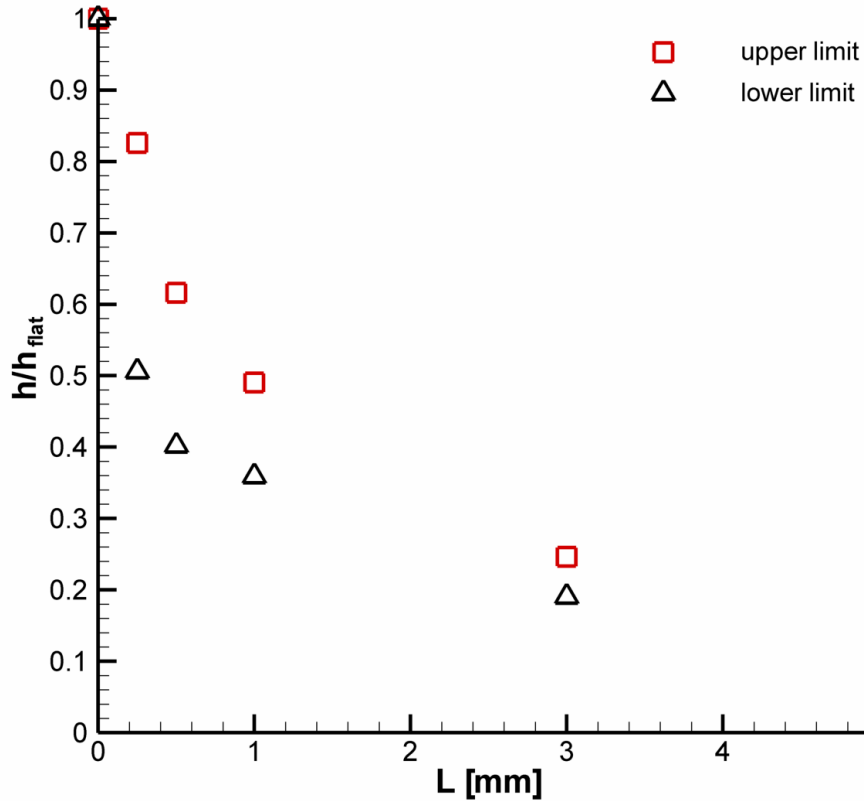


Fig. 64. One-dimensional model results as a function of fin length for $T_{wall} = 60^{\circ}\text{C}$, $\Delta P = 4.08 \text{ atm}$ (60 psig) normalized by $h_{flat} = 9784 \text{ W}/(\text{m}^2 \cdot \text{K})$.

In both limiting cases, this model predicts a temperature profile that is qualitatively similar (Fig. 65). The temperature profile predicted by the model shows a modest temperature drop along the length of the fin, suggesting that heat transfer is not limited by the fin temperature. Given the increased area of the channeled surfaces and the modest temperature drop along the fin suggested by this model, it is more likely that heat transfer is limited by an increase in liquid temperature which lowers the local ΔT (see Appendix E for an independent numerical model that illustrates the rise in liquid temperature). Heat transfer limited by liquid that has increased in temperature is consistent with the spray efficiency plots, Figs. 61- 63, which show that the extended

structures allow for utilization of most of the spray's thermodynamic potential for heat removal.

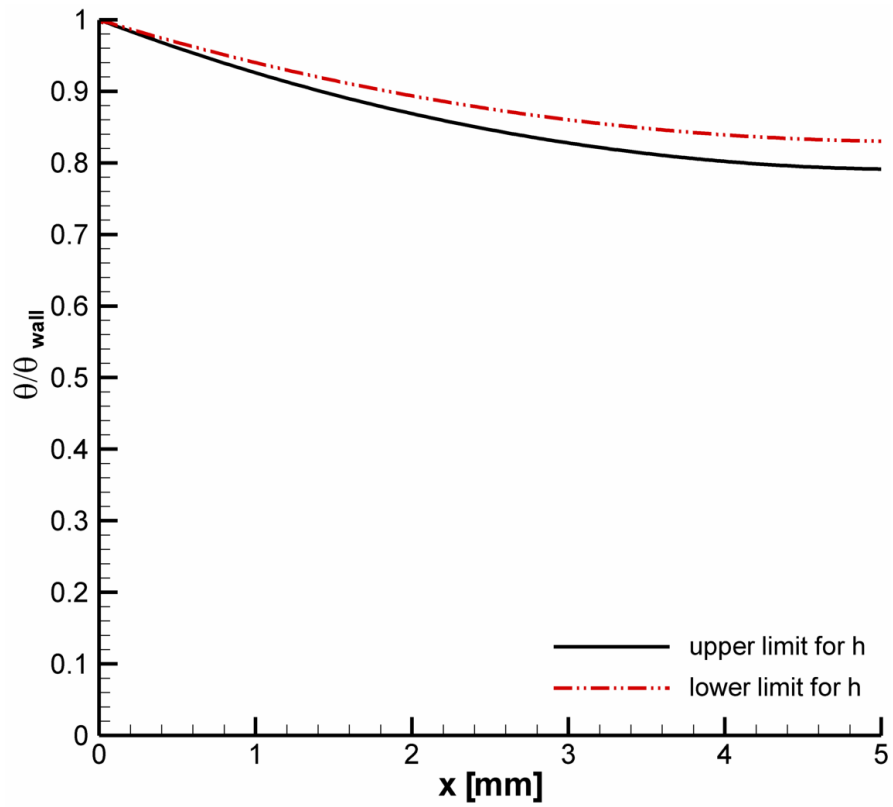


Fig. 65. Predicted temperature profile on 5 mm fins using 1-D model for $T_{wall} = 60^{\circ}\text{C}$, $\Delta P = 4.08 \text{ atm}$ (60 psig).

CHAPTER 7. CONTRIBUTIONS AND CONCLUSIONS

This dissertation was designed to shed light on important and topical heat transfer enhancement techniques. Spray cooling with nanofluids and extended surfaces have been reviewed, experimentally investigated, analyzed, and modeled. The specific conclusions, contributions, and suggestions for future work are as follows.

7.1. Conclusions

Nanofluid boiling was experimentally investigated with alumina-in-water and alumina-in-ethanol nanofluids on four different types of surfaces: glass, gold, copper, and copper oxide. The results were found to be highly dependent on the fluid/surface combination, specifically wetting characteristics. Poorly wetting systems (e.g. water on copper) could be enhanced by nanofluids, whereas better wetting systems (e.g. ethanol on glass) showed little or no improvement. Generally, critical heat flux was unchanged or even sometimes degraded at small particle loadings, contrary to some reports in the literature (e.g. You et al., 2003). Greater concentrations (≥ 0.5 g/L) lead to modest (up to ~37%) increase in the CHF, but direct comparisons with the same heater indicated that greater particle concentrations were required for highly wetting base fluids. In another comparison, dilute water based nanofluid was used on copper (less wetting) and copper oxide (more wetting) and the CHF degradation due to nanofluids was worse for the more wetting surface. Interestingly, oxidizing a copper surface and using pure water proved more effective at enhancing CHF than using any concentration of nanofluids because of the high superheat required for nanofluid CHF enhancement.

All the experimental results indicate that nanofluid CHF enhancement is strongly linked to poor wettability. When surfaces are easily wetted by base fluid, nanofluids are

less useful and sometimes more degrading. The boiling results lead to experiments in which the three-phase contact angle was measured for droplets advancing across copper and copper oxide surfaces. Nanofluids alone were found to have no effect on the advancing contact angle. However, nanofouling that resulted after the dryout of nanofluid could significantly reduce the advancing contact angle. This reduction in advancing contact angle can improve evaporation during the rewetting following bubble detachment. However, the reduction in contact angle due to nanofouling is decreased for highly wetting systems. This may explain the observation that the CHF of highly wetting systems such as ethanol on glass is more difficult to enhance.

Nanofluids spray cooling was found to be ineffectual because of poor particle stability and fluid properties. Dilute suspensions were found to have no effect on spray cooling heat transfer. However, a suspension of 0.5 g/L alumina-in-ethanol was found to degrade CHF by 49% due to a reduction in volumetric flow rate. Scaling analysis based on impinging jet flow correlations indicated that improvements in the heat transfer coefficient due to increases in the thermal conductivity with nanofluid are offset by more dramatic degradation due to increases in viscosity. More simple, robust, and cost effective spray cooling enhancement is possible by direct surface modification such as the addition of microstructures.

Spray cooling enhancement due to surface modification was studied with a series of high aspect ratio open microchannels. The microchanneled surfaces were found to enhance both the single-phase and two-phase regimes of spray cooling. Single-phase enhancement was found to be non-linear and approach an optimum just past the longest fins (5 mm) tested. Heat transfer enhancement was significantly less than the linear area

enhancement suggesting another and/or additional mechanisms. A one-dimensional model was developed, which indicated that heat transfer was not limited by the conduction resistance of the fin. Rather, it appears that heat transfer is limited by the amount of sensible heat that can be absorbed by the liquid.

With microchanneled surfaces, the greatest increase in heat transfer occurred when two-phase effects were triggered. The onset of two-phase effects was earlier (lower temperature) with finned surfaces resulting in up to 181% enhancement. In fact, the two-phase regime began earlier as the fin length increased. Interestingly, while the onset temperature was a function of fin length, it was unaffected by changes in the nozzle pressure/flow rate (for both finned and the flat surfaces). This indicates that the velocity of the liquid film inside the channel is not responsible for the onset of two-phase effects and therefore not responsible for the large heat transfer enhancement observed with microchanneled surfaces. Instead, the most likely mechanisms responsible are liquid pooling or starvation in channels that are shaded from the impinging droplets.

Finally, the spray efficiency was calculated for enhanced surfaces and was found to be much higher than for bare surfaces. In fact, spraying structured surfaces was found to result in spray efficiencies that approached the theoretical maximum because of the greater heater area and earlier onset of two-phase effects.

7.2. Contributions to the State of the Art

Spray cooling and nanofluids are current, important, and controversial topics in heat transfer. This dissertation is based on carefully designed experiments that provide novel data that answers open questions posed in the literature and allows for the development of models based on previously unforeseen mechanisms. The major

conclusions have been discussed above but the specific contributions to the state of the art are as follows:

- Nanofluids based on highly wetting base fluids have been shown to be less effective at enhancing CHF in pool boiling.
- Similarly, high energy surfaces such as metal oxides were also shown to be less susceptible to nanofluid CHF enhancement.
- The advancing contact angle of nanofluid was found to be indistinguishable from pure fluid on clean surfaces. However, the advancing contact angle was significantly reduced following nanofluid dryout due to nanofouling.
- These observations lead to the proposed boiling enhancement mechanism: nanoparticle deposition from dryout during bubble growth reduces the advancing contact angle of the rewetting liquid during bubble detachment. The thinner liquid wedge rewetting the surface has improved evaporation efficiency.
- Spray cooling of nanofluids was found to be detrimental due to the poor stability of the particles in the vapor phase as well as the fluid viscosity increasing faster than the thermal conductivity.
- High aspect ratio open microchannels were found to be a very efficient and effective means of enhancing spray cooling since the microchannels triggered the onset of two-phase effects at lower temperatures. Spray efficiencies were found to approach unity for fins of moderate (1 – 3 mm) length.
- The onset of two-phase effects was found to occur earlier as the depth of the channel increased suggesting that liquid distribution was key to the

enhancement. Further, the onset of two-phase effects was found to be independent of flow rate, which suggests that geometry and not the velocity of liquid in the channel is responsible for the heat transfer enhancement.

7.3. Suggestions for Future Work

The first major thrust of this research was to determine if boiling CHF could be enhanced by nanofluids and by what mechanism. Any effort such as this that is aimed at enhancing CHF is clearly hampered by a lack of a validated model of the basic phenomena. This study as well as many others has shown that contact angle plays an important role in determining CHF, and this fundamental topic merits further investigation.

While the fundamental mechanism underlying boiling nanofluids is now known, the study of nanofluids boiling could be continued by using different suspensions such as those based on carbon nanotubes (CNT), preferably suspensions whose thermal conductivity rises faster than the viscosity. The high aspect ratio of CNT's may provide greater thermal transport, particularly in the nucleate boiling regime. Alternatively, this work could be extended through the study of surfaces that have been pretreated with nanostructures. Micro-structuring is known to enhance boiling, and the nanofouling observed in the present work was found to be beneficial in some cases. A systematic study of boiling on nanostructures offers an exciting new area of research with significant potential for CHF enhancement.

The second major thrust of this research was aimed at understanding the mechanisms underlying spray cooling enhancement with microchannels. The discovery that the greatest enhancement was caused by early onset of two-phase effects suggests

future research topics. First, what is the fundamental cause of the onset of two-phase effects in spray cooling? What roles do nucleation suppression, secondary nuclei, and film thickness play in the onset of two-phase effects?

To better understand spray cooling of microstructured surfaces, future research could be targeted towards direct observation of the spatial temperature distribution on the microstructures. The present work has shown that the onset of two-phase effects is key to the enhancement. By looking at the heat transfer in regions of the structure that are shaded from the impinging droplets, this phenomena could be better understood. Then by changing the shape and distribution of the spray, the heat flux could be further enhanced.

APPENDIX A: SURFACE WETTABILITY AND CONTACT ANGLE DEFINITIONS

Wettability refers to the affinity between a liquid and a solid, and it is a function of the various inter- and intramolecular bond strengths. This is typically quantified by measuring the liquid/solid contact angle, θ (see Fig. 66). The two extremes of wettability are *completely wetting* surfaces with $\theta = 0^\circ$ and *completely nonwetting* when $\theta = 180^\circ$. Between these two extremes the liquid/surface combination is said to *wetting* when $0^\circ \leq \theta \leq 90^\circ$ and *nonwetting* when $90^\circ < \theta \leq 180^\circ$. For instance, liquids with strong intramolecular bonds (i.e., high surface tension) will tend to be nonwetting and form more spherical droplets on surfaces. Similarly, solid surfaces with low surface free energy (e.g., Teflon) will also tend to be difficult to wet. Conversely, surfaces with high surface energy, like glass, will tend to be wetted easily.

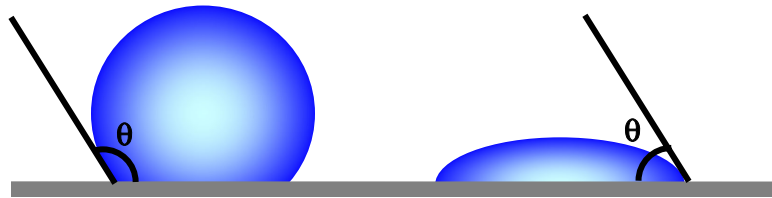


Fig. 66. Nonwetting (left) and wetting (right) liquid droplets.

For a smooth surface, the equilibrium contact angle can be determined using Young's equation:

$$\sigma_{sv} = \sigma_{sl} + \sigma_{lv} \cos \theta \quad (49)$$

Young's equation is a force balance between the various interfacial tensions, which need to be determined.

However, the physics of how liquids spread across real solid surfaces remains difficult and poorly understood (de Gennes, 1985). Surface irregularities and chemical contamination result in different contact angles even with similar experiments. At least part of the problem is due to the difference between equilibrium and dynamic contact angles.

The equilibrium contact angle is often measured using the sessile drop method in which a liquid droplet is placed on a solid surface. The angle between the base of the droplet and the solid surface is then optically measured. This is a simple and convenient method. However, one problem with this method is that if performed in an open environment, the droplet is free to evaporate. During evaporation the angle is not at equilibrium and will change as the droplet shrinks in base diameter.

Dynamic contact angles vary depending on the motion history of the liquid/solid/vapor contact line. As a liquid moves across a dry surface, the angle is termed an *advancing contact angle*. If liquid retreats from a previously wet portion of the surface, then the angle formed is termed a *receding contact angle*. The two angles are shown schematically in Fig. 67, where the advancing contact angle is generally larger than the receding. The hysteresis effect is likely due to surface inhomogeneity, surface roughness, and/or impurities on the surface (Carey, 1992).

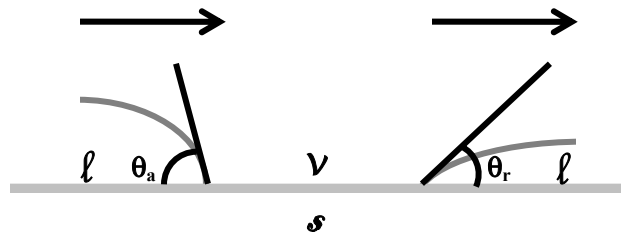


Fig. 67. Schematic of advancing and receding contact angles.

APPENDIX B: LIBRARY OF COMPUTER PROGRAMS

The data acquisition and analysis programs developed for this dissertation are listed in Table 11. Soft copies of the codes are available on CDROM from the author.

Table 11. List of data acquisition and analysis programs.

Filename	Function
angle_proc5a.m	Perform edge detection on advancing drops
angle_proc5b.m	Calculate contact angle
DAQ_menu2.m	Data acquisition for thick-film heater
DAQ_menu4.m	Data acquisition for copper block heater
ethanol_data.m	Data reduction of boiling ethanol data (main)
fin_liquid_temperature_rise.m	Finite-difference solver used in Appendix E
MonteCarlo_LSQ_tempgrad.m	Monte Carlo error analysis of temperature gradient data
MonteCarlo_sprayeff.m	Monte Carlo error analysis for spray efficiencies
postDAQ_2pt1.m	Data reduction of boiling water data (function)
postDAQ_2pt2.m	Data reduction of boiling ethanol data (function)
spray7.m	Data reduction for extended surfaces data (function)
spray7_master.m	Data reduction for extended surfaces data (main)
water_data.m	Data reduction of boiling water data (main)

APPENDIX C: MONTE CARLO UNCERTAINTY CALCULATIONS

Monte Carlo methods are used to solve physical problems through a series of statistical experiments based on applying mathematical operations to random numbers (“Monte-Carlo Method,” 1956). In this dissertation, the Monte Carlo method has been used in lieu of standard propagation of uncertainty techniques[†] (Lyons, 1996) when the quantity of interest is affected by correlated errors (e.g. multiple measurements made with the same instrument as occurs during calibration). Brown et al. (1996) reviewed this problem and noted that historically these types of problems have been dealt with by assuming either no correlation or perfect correlation. Both assumptions can be mathematically intensive (specifically when there are many parameters) and can result in erroneous error estimates. Alternatively, the Monte Carlo method can be applied to create a database of possible results where each run of the simulation is based on nominal values plus or minus random errors, including correlated and uncorrelated errors as required. The final error estimate can then be determined from this database of possible results. The Monte Carlo method used in the present work was based in part on Brown et al. (1996). Consider the following simple example as an illustration of the technique.

A 10,000 run simulation (outlined in Fig. 68) is used to estimate the error in an arbitrary data reduction equation (DRE) based on two variables:

$$y = x_1(1 + x_2) \tag{50}$$

[†] Standard propagation of uncertainty techniques are usually based on the first-order Taylor expansion. If the function is non-linear, then the errors must be small for this model to be appropriate. Furthermore, when variables are correlated the covariance term must be retained. For complex non-linear functions of many variables, this method can be unwieldy involving many terms; and attempts to verify the validity of the first-order model necessitates even greater complexity.

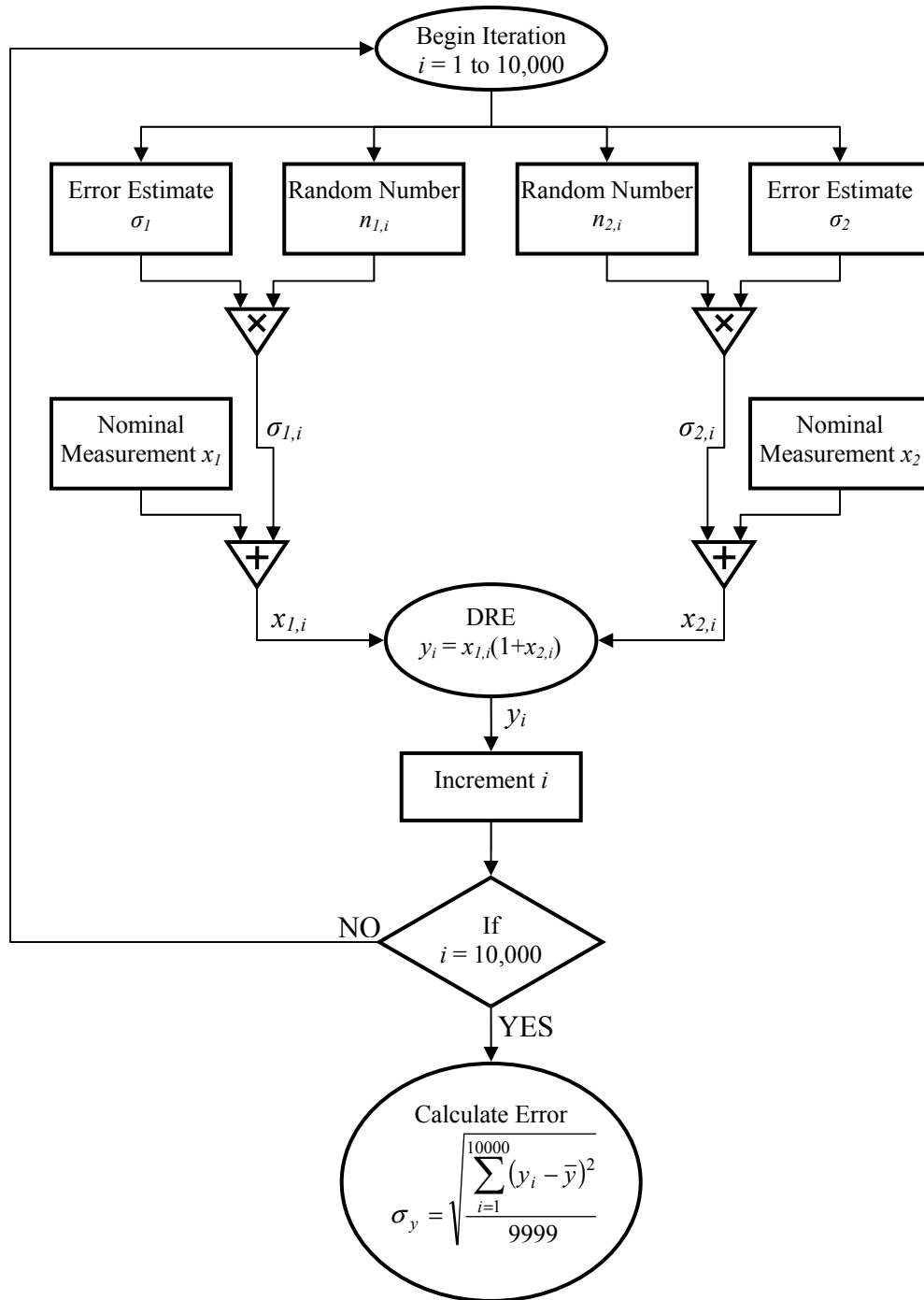


Fig. 68. Monte Carlo error estimation technique.

Assuming there are only two independent sources of error, the error in y depends on four inputs: x_1 and x_2 (the nominal measurements) and σ_1 and σ_2 (the estimated errors).

Each step in the simulation involves creating random errors to be added to the nominal measurements. Actually, a pseudo-random number generator will be used, but the term *random* is used for convenience. To generate random errors, MATLAB is first used to generate normally distributed random numbers ($n_{1,i}$ and $n_{2,i}$) with a mean of 0 and a standard deviation of 1. Then, the random numbers are multiplied by the estimated errors (σ_1 and σ_2) to obtain a random errors ($\sigma_{1,i}$ and $\sigma_{2,i}$). Then, these random error are added to the nominal measurements (x_1 and x_2) to obtain random measurements ($x_{1,i}$ and $x_{2,i}$). In this example, σ_1 and σ_2 have been assumed to be uncorrelated and were therefore based on different random numbers. If they had been correlated, then the same random error would be added to each of the nominal measurements. For each iteration of the simulation, the random measurements ($x_{1,i}$ and $x_{2,i}$) are used in the DRE to obtain a simulated resultant, y_i . Running the simulation 10,000 times is the statistical equivalent of repeating the experiment 10,000 times, each time resulting in a slightly different result due to random measurement errors. After all 10,000 simulations, the standard deviation of y is determined, σ_y .

The above example could have been treated with the standard propagation of uncertainty technique (if the errors are small) since the errors are uncorrelated and the partial derivatives can be easily determined. However, consider least-squares fitting, where the fitting coefficients are dependent on many variables and the errors can be correlated. It is for these types of problems, specifically calibration, for which this technique has been applied in this dissertation. The specific calculations are discussed in Chapter 4.

APPENDIX D: CALCULATION OF PF-5060 VAPOR SPECIFIC HEAT

The vapor specific heat of PF-5060 (C₆F₁₄) was estimated using the Yoneda (1979) method for organic compounds in the ideal gas state. This estimate is based on the principle of group contribution in which the molecule is decomposed into atom groups, called functional groups. The inclusion of each functional group results in a contribution to the specific heat. Each contribution includes a constant, linear and quadratic term. The temperature dependent specific heat is then estimated by summing all group contributions as in Eq. 51.

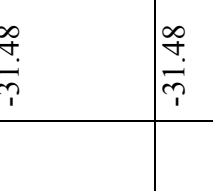
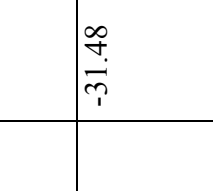
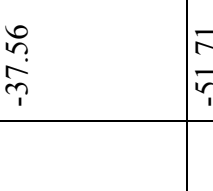
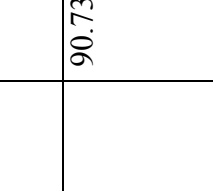
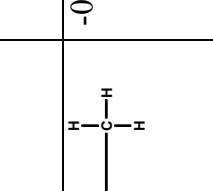
$$c_p [J / mol \cdot K] = \sum_i^I \Delta a_i + \sum_i^I \Delta b_i \frac{T}{1000} + \sum_i^I \Delta c_i \left(\frac{T}{1000} \right)^2 \quad (51)$$

The original database was created by deconstructing molecules with known properties into functional groups. Only the effects of nearest-neighbor atoms and geminal effects (the effects of atoms separated by one atom) were included since more complicated molecular interactions are usually insignificant. This method is extremely useful in estimating thermophysical properties since countless different organic compounds exist in nature as well as in the lab. Their properties are determined by constructing the molecule of interest from the original set of functional groups. The specific steps used in calculating the specific heat of PF-5060 (C₆F₁₄) are given in Table 12. Following these steps, the specific heat as a function of temperature was estimated to be:

$$c_{p,v} [J / kg \cdot K] = 229.38 + 2.4998T[K] - 0.0013041T[K]^2 \quad (52)$$

Table 12. Steps in specific heat calculation for C₆F₁₄.

Step Description	Number of Times Step is Applied	Resulting Molecule	Δa [J/(mol·K)]	Δb [J/(mol·K ²)]	Δc [J/(mol·K ³)]
Methane base group	1	<pre> H H-C-H H </pre>	16.71	65.65	-9.96
Primary methyl substitution	1	<pre> H H H-C-C-H H H </pre>	-9.92	103.87	-43.54
Secondary methyl substitution (type 1,1)	1	<pre> H H H H-C-C-C-H H H H </pre>	-3.68	98.22	-42.29
Secondary methyl substitution (type 1,2)	1	<pre> H H H H-C-C-C-H H H H </pre>	1.47	81.48	-31.48
Secondary methyl substitution (type 1,2)	1	<pre> H H H H-C-C-C-H H H H </pre>	1.47	81.48	-31.48

Secondary methyl substitution (type 1,2)	1		1.47	81.48	-31.48
Secondary methyl substitution (type 1,2)	1		1.47	81.48	-31.48
Secondary methyl substitution (type 1,2)	1		1.47	81.48	-31.48
Secondary methyl substitution (type 2,2)	3		-0.63	90.73	-37.56
Secondary methyl substitution (type 3,2)	3		-6.91	111.79	-51.71

Secondary methyl substitution (type 2,4)	3		-1.21	92.11	-38.02
Secondary methyl substitution (type 3,4)	3		-4.19	129.62	-66.36
Fluorine fundamental replacement	14		4.23	-76.62	24.58
Type number correction	42		1.59	-0.54	1.59
Multiple substitution correction	10		-2.01	-0.75	-1.76

Yoneda (1979) estimated a 4% standard deviation for the specific heat estimation of fluorine compounds. However, an independent test of uncertainty was performed. Following the same procedure as outlined above for C_6F_{14} , the specific heat of C_5F_{12} was determined and compared to NIST Standard Reference Database 69 (2005). This resulted in agreement within 2.1%.

APPENDIX E: NUMERICAL MODEL OF FIN HEAT TRANSFER

The analytical model presented in Chapter 6 indicated that even long (5 mm) fins did not exhibit large temperature drops (i.e., the fin temperature profile was almost flat). However, the heat transfer of the microchanneled surfaces was found to be much less than one would expect based on the area enhancement. Therefore, the likely limiting mechanism was the finite liquid supply. To verify this conclusion, a numerical model was developed in which all of the heat transfer from the fin was absorbed by the finite liquid supply provided by the spray. Specifically, convection heat transfer was balanced by sensible heat transfer as shown in Eq. 53.

$$hA(T - T_l) = \dot{m}c_p \Delta T_l \quad (53)$$

The following assumptions were made in the present model:

- One-dimensional (no variations along the length of the channel or through the thickness of the fin)
- Steady-state
- No phase-change of the liquid or dryout
- No liquid splashing
- Mass flow rate from the spray is distributed uniformly throughout the microchanneled surface
- Local heat transfer coefficient is constant (only the local liquid temperature is variable)
- Convection from the fin's tip (top surface only) is based on the unheated liquid temperature, T_{spray}

E.1. Model Development

A coupled (set of two) one-dimensional finite difference approach was used to model the heat transfer within the fin as well as the heat transfer from the fin to the liquid supplied by the spray. The tip region of the fin is shown schematically in Fig. 69. The fin's energy balance is a balance between conduction within the fin and convection to the local liquid. However, all of the heat lost by the fin must be absorbed by the liquid, which is flowing down the fin. To determine how much the liquid has heated up, the liquid was discretized into differential control volumes. The mass of liquid in each control volume was determined by dividing the total mass flow rate (provided by the spray) by the number of fins on the surface (i.e., the mass was assumed to be uniformly distributed).

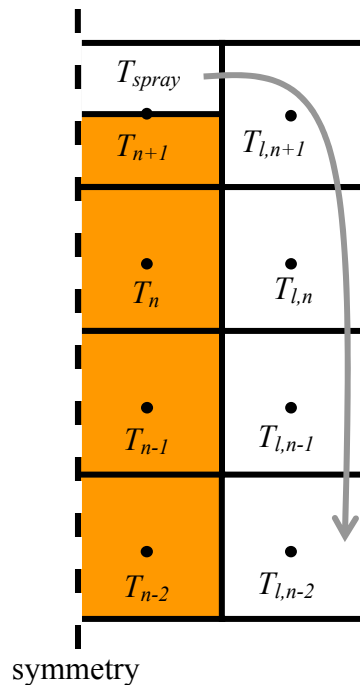


Fig. 69. Finite difference model of the fin tip region. The solid fin and liquid are shown as shaded and unshaded, respectively. Heat is conducted within the fin and convected to the local liquid, which moves down the fin.

The nodal energy balance equations were developed as follows. Consider row n : The local convection is determined by the solid to liquid temperature difference $T_n - T_{l,n}$. The temperature of the solid, T_n , is then determined by summing this local convection along with conduction into and out of the solid differential control volume, as shown in Eq. 54.

$$T_n = \frac{\frac{hP_f(\Delta x)^2 T_{l,n}}{kA_c} + T_{n+1} + T_{n-1}}{2 + \frac{hP_f(\Delta x)^2}{kA_c}} \quad (54)$$

The local liquid temperature, $T_{l,n}$, is determined by how much heat transfer has occurred upstream. Specifically, $T_{l,n}$ is determined by $T_{l,n+1}$ and the convection heat transfer occurring between rows $n+1$ and n . This is shown schematically in Fig. 70. Specifically, the temperature of the liquid at row n is given by Eq. 55.

$$T_{l,n} = \frac{T_{n+1} + T_n - T_{l,n+1} \left(\frac{2\dot{m}c_p}{hP_f\Delta x} - 1 \right)}{1 + \frac{2\dot{m}c_p}{hP_f\Delta x}} \quad (55)$$

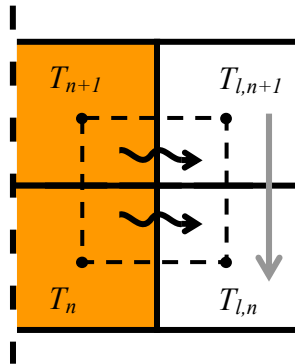


Fig. 70. Finite difference model showing liquid temperature increase due to local convection between rows $n+1$ and n . The solid fin and liquid are shown as shaded and unshaded, respectively.

Different nodal equations were required for the fin's tip since the model was developed assuming that the top surface is cooled by fresh liquid at T_{spray} . However, since the differential control volume associated with the tip node includes side area, the local liquid temperature must also be determined. The tip temperature and local liquid temperatures are given by Eqs. 56 and 57, respectively.

$$T_{tip} = \frac{T_{n-1} + \frac{h\Delta x}{k} T_{spray} + \frac{hP_f \Delta x^2}{2kA_c} T_{l,n}}{1 + \frac{h\Delta x}{k} + \frac{hP_f \Delta x^2}{2kA_c}} \quad (56)$$

$$T_{l,n} = \frac{hA_c}{\dot{m}c_p} (T_{tip} - T_{spray}) + T_{spray} \quad (57)$$

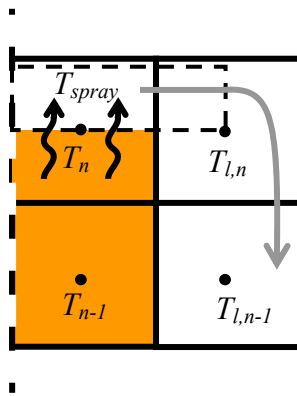


Fig. 71. Finite difference model showing liquid temperature increase due to convection at the tip. The solid fin and liquid are shown as shaded and unshaded, respectively.

As is often the case in finite difference models, the nodal equations are interdependent and must be solved iteratively. The code was developed in MATLAB and solved iteratively with a grid size of 51×2 . The convergence criteria was 10^{-5} °C per iteration.

E.2. Model Results

The first step required to use the above described model was model validation. If the liquid supply is infinite, then the present model should revert to the conventional analytical solution for a convection cooled fin, Eq. 45. Temperature profiles for various mass flow rates are shown in Fig. 72. For high mass flow rates, the liquid supply is effectively infinite and the analytical solution is approximated. As the flow rate decreases, the liquid begins to heat up as it flows down the fin. This causes the temperature profile to depart from the analytical solution (specifically, the fin profile shifts upward toward the base temperature). At very low flow rates (like those used in the experiment) the liquid approaches the same temperature as the fin, which greatly reduces the local heat transfer.

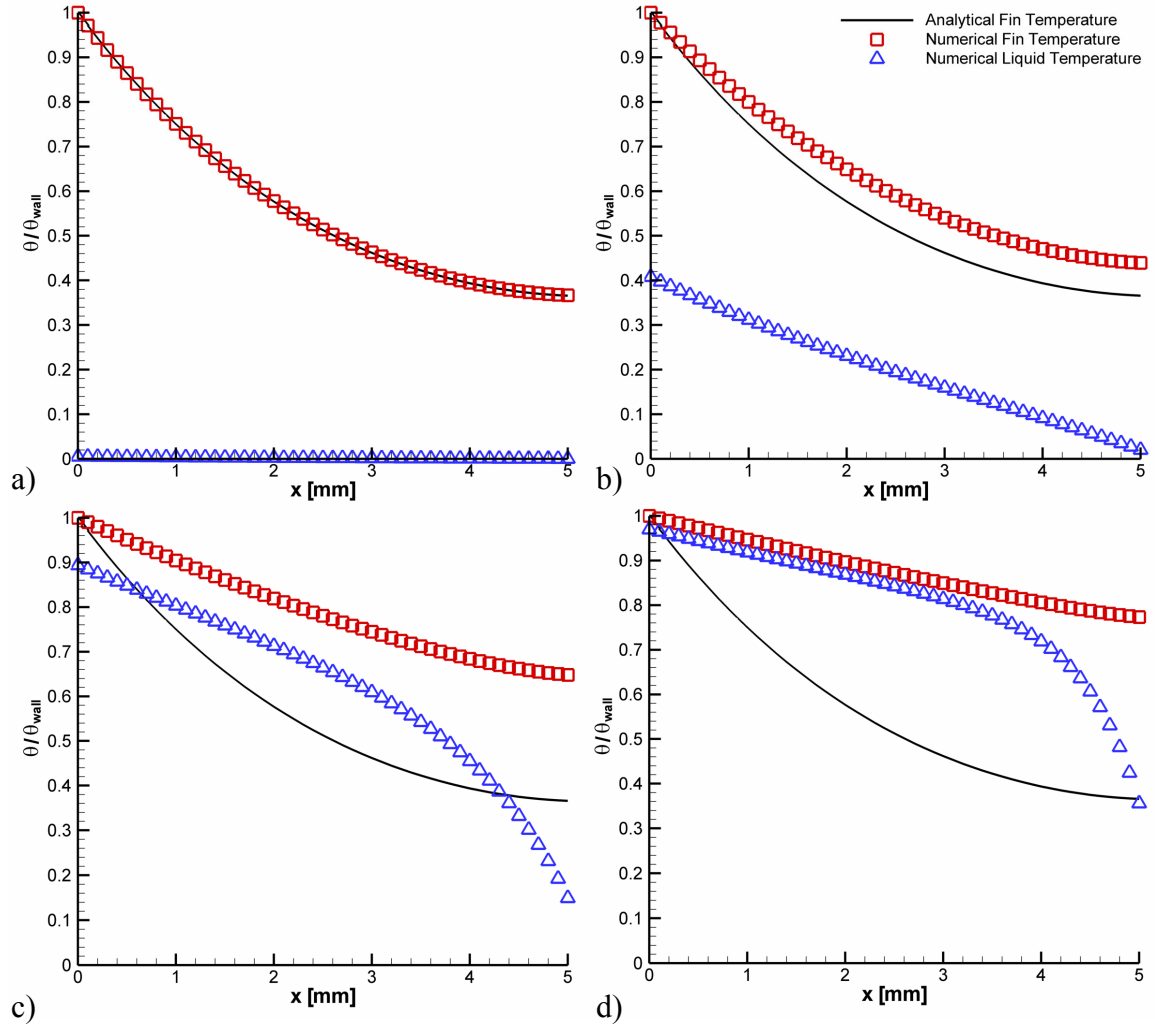


Fig. 72. Temperature profiles for various mass flow rates. Plots a) – d) show mass flow rates of $1000 \bar{m}$, $10 \bar{m}$, $2 \bar{m}$, and \bar{m} , respectively, where \bar{m} is the average per fin mass flow rate used in the experiment. $h = 10,000 \text{ W/m}^2\cdot\text{K}$.

Heat transfer from a conventional fin (with an infinite fluid supply) is highest near the base, where the temperature difference is the greatest. However, with a low mass flow rate, the local temperature difference is greatest at the tip of the fin. The local heat flux is shown as a function of position along the fin for various mass flow rates in Fig. 73. Again, the highest mass flow rate approximates the analytical solution, with heat transfer decreasing along the length of the fin. However, as the mass flow rate is decreased, the tip heat transfer increases. Then, at very low flow rates (like those used in

the experiments), the heat transfer monotonically increases along the length of the fin. Not only is the tip heat transfer relatively higher than the base heat transfer at low mass flow rates, but the tip heat transfer is absolutely higher for low mass flow rates because the fin tip is hotter (note the flattened temperature profile in Fig. 72).

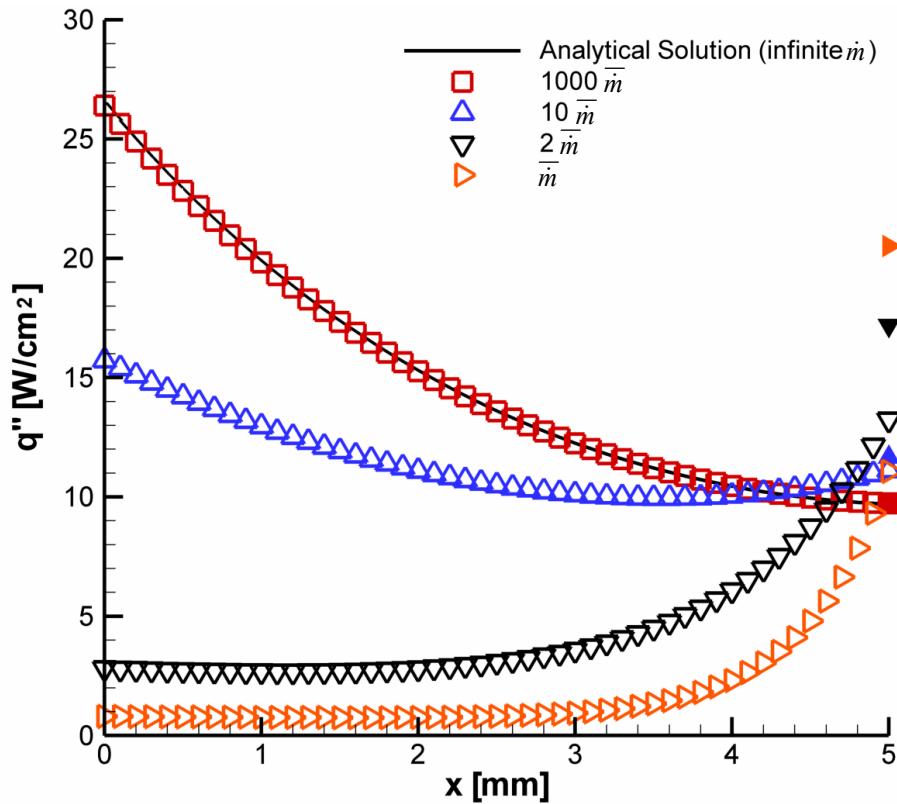


Fig. 73. Local heat flux as a function of position on fin. Solid symbols show heat flux off the top surface of the fin (rather than the top node in the model). $h = 10,000 \text{ W/m}^2\cdot\text{K}$.

With the average per fin mass flow rate used in the experiments (0.000146 kg/s), this model indicates that over 35% of the total heat transfer is occurring through the tip because of the high local liquid temperature difference. In contrast, the trough (not modeled directly) would only add about 1% more to the total heat transfer since the local liquid temperature at the base is so low. This supports the “upper limit” assumption made in Chapter 6, in which the heat transfer from the trough is neglected.

The above results were for a heat transfer coefficient of $10,000 \text{ W/m}^2\cdot\text{K}$, which is consistent with the unenhanced surface spray cooling curves presented in Chapter 6. However, for the conditions modeled, the total heat transfer from the enhanced surface was determined to be 70 W. This compares to 104 W observed in the experiment. To explore the origin of this discrepancy, the heat transfer coefficient was varied. The results of heat transfer coefficient variation are shown in Fig. 74. Increasing the heat transfer coefficient, increases the rate at which the liquid temperature increases. This has a negative feedback effect in the sense that raising the heat transfer coefficient should increase heat transfer, but it results in lower local temperature difference. The modeled heat transfer was never observed to reach the experimentally observed value. The discrepancy is therefore likely due to the assumptions inherent in the model such as uniform mass distribution and possibly the no phase-change assumption.

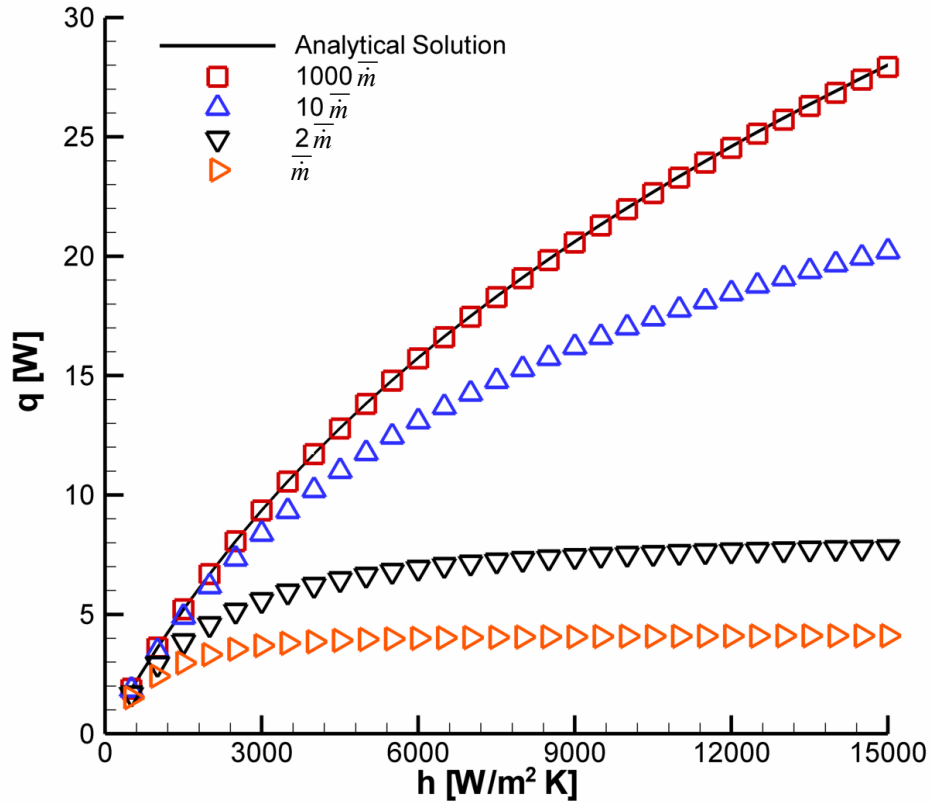


Fig. 74. Single fin heat transfer as a function of heat transfer coefficient.

E.3. Conclusions and Implications

A two-dimensional finite difference model was developed independently of the analytical model described in Chapter 6. The numerical model was based on the convection heat transfer driven by local temperature differences. The local liquid temperature was found to increase rapidly for low mass flow rates like those used in the experiments. In fact, using the average per channel mass flow rate that was used in the experiments, the liquid was found to heat up almost to the fin temperature. If one considers the variation in mass flow rate due to the full-cone spray pattern, the outer channels (with their low flow rates) could be expected to suffer very large liquid temperature rises. One could speculate that this is responsible for the early onset of two-

phase effects described in Chapter 6. Conversely, the fluid rich inner channels would experience a more modest but still very significant liquid temperature rise. The result of the liquid temperature increase is a flattening of the fin temperature profile, consistent with the analytical model presented in Chapter 6.

The liquid temperature rise has important implications to the local and total heat transfers. Since the local liquid temperature is significant hotter when it reaches the base of the fins, the troughs' contribution to heat transfer is negligible despite it having the highest local surface temperature. Conversely, the numerical model indicates that the fin tips dominant the heat transfer process because of the cold local liquid supplied by the spray. This model may explain why the pyramidal pin fins used by Silk et al. (2004) resulted in poorer performance than the cubic pin fins despite having similar surface area.

REFERENCES

- 3M, 2000, "Fluorinert Electronic Liquid FC-72 Product Literature."
- 3M, 2003, "Performance Fluid PF-5060 Product Literature."
- Ammerman, C.N., and You, S.M., 1996, "Determination of the Boiling Enhancement Mechanism Caused by Surfactant Addition to Water," *Journal of Heat Transfer*, **118**, pp. 429-435.
- ASM International, 2001, *ASM Specialty Handbook: Copper and Copper Alloys*, Ed. J.R. Davis, ASM International: Materials Park, OH, p. 453.
- Bang, I.C., and Chang, S.H., 2005, "Boiling Heat Transfer Performance and Phenomena of Al₂O₃-Water Nano-fluids from a Plain Surface in a Pool," *International Journal of Heat and Mass Transfer*, **48**, pp. 2407-2419.
- Batthey, J.F., Nelson, N.J., and Barnett, D.J., 1988, "Copper Etching Process and Product," US Patent Number 4,767,662.
- Brown, K.K., Coleman, H.W., Steele, W.G., and Taylor, R.P., 1996, "Evaluation of Correlated Bias Approximations in Experimental Uncertainty Analysis," *AIAA Journal*, **34**(5), pp. 1013-1018.
- Canny, J., 1986, "A Computational Approach to Edge Detection," *IEEE Transactions on Pattern Analysis and Machine Intelligence*, **8**(6), pp. 679-698.
- Chandra, S., di Marzo, M., Qiao, Y.M., and Tartarini, P., "Effect of Liquid-Solid Contact Angle on Droplet Evaporation," *Sparse Water Sprays in Fire Protection*, M. di Marzo, Ed., United States Department of Commerce, NIST-GCR-96-687, pp. 168-194.
- Chen, J.C., 1966, "Correlation for Boiling Heat Transfer to Saturated Fluids in Convective Flow," *Industrial & Engineering Chemistry Process Design and Development*, **5**(3), pp. 322-339.
- Chen, R.-H., Chow, L.C., and Navedo, J.E., 2002, "Effects of Spray Characteristics on Critical Heat Flux in Subcooled Water Spray Cooling," *International Journal of Heat and Mass Transfer*, pp. 4033-4043.
- Choi, S.U.S., Zhang, Z.G., Yu, W., Lockwood, F.E., and Grulke, E.A., 2001, "Anomalous Thermal Conductivity Enhancement in Nanotube Suspensions," *Applied Physics Letters*, **79**(14), pp. 2252-2254.
- Chon, C.H., Kihm, K.D., Lee, S.P., and Choi, S.U.S., 2005, "Empirical Correlation Finding the Role of Temperature and Particle Size for Nanofluid (Al₂O₃) Thermal Conductivity Enhancement," *Applied Physics Letters*, **87**, paper no. 153107.

- Chow, L.C., Sehmbe, M.S., and Pais, M.R., 1995, "Critical Heat Flux in High Heat Flux Spray Cooling," *The Symposium on Thermal Science and Engineering in Honor of Chancellor Chang-Lin Tien*, Editors: R. O. Buckius., University of California, Berkeley, Berkeley, CA. pp. 407-413.
- Das, S.K., Putra, N., and Roetzel, W., 2003, "Pool Boiling Characteristics of Nano-fluids," *International Journal of Heat and Mass Transfer*, **46**, pp. 851-862.
- Demiray, F., and Kim, J., 2004, "Microscale Heat Transfer Measurements During Pool Boiling of FC-72: Effect of Subcooling," *International Journal of Heat and Mass Transfer*, **47**, pp. 3257-3268.
- Dillion, H.E., and Penoncello, S.G., 2003, "A Fundamental Equation for the Calculation of the Thermodynamic Properties of Ethanol," *Fifteenth Symposium on Thermophysical Properties*, June 22-27, 2003, Boulder, Colorado, U.S.A. As Cited In: Klein, S.A., 2006, *Engineering Equation Solver*. Computer Software, F-Chart Software, Version 7.693.
- di Marzo, M., 1996, *Sparse Water Sprays in Fire Protection*, United States Department of Commerce, NIST-GCR-96-687.
- Ding, Y., Alias, H., Wen, D., and Williams, R.A., 2006, "Heat Transfer of Aqueous Suspensions of Carbon Nanotubes (CNT Nanofluids)," *International Journal of Heat and Mass Transfer*, **49**, pp. 240-250.
- Eastman, J.A., Choi, U.S., Li, S., Thompson, L.J., and Lee, S., 1997, "Enhanced Thermal Conductivity through the Development of Nanofluids," *Proc. of the Materials Research Society Symposium*, **457**, pp. 3-11.
- Eastman, J.A., Choi, S.U.S., Li, S., Yu, W., and Thompson, L.J., 2001, "Anomalously Increased Effective Thermal Conductivities of Ethylene Glycol-Based Nanofluids Containing Copper Nanoparticles," *Applied Physics Letters*, **78**(6), pp. 718-720.
- Estes, K.A., and Mudawar, I., 1995a, "Comparison of Two-Phase Electronic Cooling Using Free Jets and Sprays," *Journal of Electronic Packaging*, **117**, pp. 323-332.
- Estes, K. A. and Mudawar, I., 1995b, "Correlation of Sauter Mean Diameter and Critical Heat Flux for Spray Cooling of Small Surfaces," *International Journal of Heat and Mass Transfer*, **38**(16), pp. 2985-2996.
- Fabbri, M., Jiang, S., and Dhir, V.K., 2003, "Experimental Investigation of Single-Phase Micro Jets Impingement Cooling for Electronic Applications," *Proc. of the 2003 ASME Summer Heat Transfer Conference*, July 21-23, 2003, Las Vegas, Nevada, paper no. HT2003-47162.
- Friedlander, S.K., 2000, *Smoke, Dust, and Haze: Fundamentals of Aerosol Dynamics*, 2nd Ed., Oxford University Press, New York.

- Gandhi, K.S., 2007, "Thermal Properties of Nanofluids: Controversy in the Making?" *Current Science*, **92**(6), pp. 717-718.
- Halif, R., and Flusser, J., 1998, "Numerically Stable Direct Least Squares Fitting of Ellipses," *Proceedings of the Sixth International Conference on Computer Graphics and Visualization*, **1**, pp. 125 – 132.
- Hamilton, R.L., and Crosser, O.K., 1962, "Thermal Conductivity of Heterogeneous Two-Component Systems," *Industrial and Engineering Chemistry Fundamentals*, **1**(3), pp. 187-191.
- Han, Z.H., Yang, B., Kim, S.H., and Zachariah, M.R., 2007, "Application of Hybrid Sphere/Carbon Nanotube Particles in Nanofluids," *Nanotechnology*, **18**, paper no. 105701 .
- Haramura, Y., and Katto, Y., 1983, "New Hydrodynamic Model of Critical Heat Flux Applicable Widely to Both Pool and Forced Convection Boiling on Submerged Bodies in Saturated Liquids," *International Journal of Heat and Mass Transfer*, **26**, pp. 389–399.
- Henry, C.D., 2005, *Nucleate Pool Boiling Characteristics from a Horizontal Microheater Array*, Ph.D. dissertation, University of Maryland, College Park.
- Horacek, B., Kiger, K.T., and Kim, J., 2005, "Single Nozzle Spray Cooling Heat Transfer Mechanisms," *International Journal of Heat and Mass Transfer*, **48**, pp. 1425-1438.
- Horacek, B., Kim, J., and Kiger, K.T., 2004, "Spray Cooling Using Multiple Nozzles: Visualization and Wall Heat Transfer Measurements," *IEEE Transactions on Device and Materials Reliability*, **4**(4), pp. 614-625.
- Horibe, A., Fukusako, S., and Yamada, M., 1996, "Surface Tension of Low-Temperature Aqueous Solutions," *International Journal of Thermophysics*, **17**(2), pp. 483-493.
- Hsieh, S.S., Fan, T.-C., and Tsai, H.-H., 2004, "Spray Cooling Characteristics of Water and R-134a. Part I: Nucleate Boiling," *International Journal of Heat and Mass Transfer*, **47**, pp. 5703-5712.
- Incropera, F.P., and DeWitt, D.P., 2002, *Fundamentals of Heat and Mass Transfer*, 5th Ed., John Wiley & Sons, New York, p. 133.
- Kandlikar, S.G., 2001, "A Theoretical Model to Predict Pool Boiling CHF Incorporating Effects of Contact Angle and Orientation," *Journal of Heat Transfer*, **123**, pp. 1071-1079.
- Kim, H., Kim, J., and Kim, M., 2006b, "Experimental Study on the Characteristics and Mechanism of Pool Boiling CHF Enhancement Using Nano-Fluids," *Proceedings of ECI International Conference on Boiling Heat Transfer*, Spoleto, May 7-12, 2006. No pagination.

- Kim, J., 2006, "Spray Cooling Heat Transfer: The State of the Art," *Proceedings of the 6th International Conference on Boiling Heat Transfer*, May 7-12, Spoleto, Italy. No pagination.
- Kim, J.H., Kim, K.H., and You, S.M., 2004a, "Pool Boiling Heat Transfer in Saturated Nanofluids," *Proceedings of IMECE04 2004 ASME International Mechanical Engineering Congress and Exposition*, November 13-20, 2004, Anaheim, California, paper no. IMECE2004-61108.
- Kim, J.H., You, S.M., and Choi, S.U.S., 2004b, "Evaporative Spray Cooling of Plain and Microporous Coated Surfaces," *International Journal of Heat and Mass Transfer*, **47**, pp. 3307–3315.
- Kim, S.J., Bang, I.C., Buongiorno, J., and Hu, L.W., 2006a, "Effects of Nanoparticle Deposition on Surface Wettability Influencing Boiling Heat Transfer in Nanofluids", *Applied Physics Letters*, **89**, paper no. 153107.
- Kurihara, H.M., and Myers, J.E., 1960, "The Effects of Superheat and Surface Roughness on Boiling Coefficients," *AIChE Journal*, **6**(1), pp. 83-91.
- Kutateladze, S.S., 1952, *Heat Transfer in Condensation and Boiling*, 2nd Ed., Atomic Energy Commission Report, AEC-TR-3770.
- Lemmon, E. W., McLinden, M. O., and Friend, D. G., 2005, "Thermophysical Properties of Fluid Systems" in NIST Chemistry WebBook, NIST Standard Reference Database Number 69, Eds. P.J. Linstrom and W.G. Mallard, June 2005, National Institute of Standards and Technology, Gaithersburg MD, 20899 (<http://webbook.nist.gov>).
- Liaw, S.P., and Dhir, V.K., 1989, "Void Fraction Measurements During Saturated Pool Boiling of Water on Partially Wetted Vertical Surfaces," *Journal of Heat Transfer*, **111**, pp. 731-738.
- Lin, L., and Ponnappan, R., 2004, "Critical Heat Flux of Multi-Nozzle Spray Cooling," *Journal of Heat Transfer*, **126**(3), pp. 482-485.
- Liu, H., 2000, *Science and Engineering of Droplets: Fundamentals and Applications*, William Andrew Publishing, Norwich, NY.
- Lloyd, J.R., and Moran, W.R., 1974, "Natural Convection Adjacent to Horizontal Surfaces of Various Planforms," *ASME Paper 74-WA/HT-66*.
- Lowery, A.J., Jr., and Westwater, J.W., 1957, "Heat Transfer to Boiling Methanol – Effect of Added Agents," *Industrial and Engineering Chemistry*, **49**(9), pp. 1445-1448.
- Lyons, L., 1996, *A Practical Guide to Data Analysis for Physical Science Students*, Cambridge University Press, Cambridge, Great Britain.

Maxwell, J.C., 1873, *A Treatise on Electricity and Magnetism*, Clarendon Press, Oxford.

Moghaddam, S., 2006, *Microscale Study of Nucleation Process in Boiling of Low-Surface-Tension Liquids*, Ph.D. dissertation, University of Maryland, College Park.

“Monte-Carlo Method,” 1956, *The International Dictionary of Physics and Electronics*, D. Van Nostrand Company, Inc., Princeton, NJ., pp. 591-592.

Moreno, G., Jr., Oldenburg, S.J., You, S.M., and Kim, J.H., 2005, “Pool Boiling Heat Transfer of Alumina-Water, Zinc Oxide-Water and Alumina-Water+Ethylene Glycol Nanofluids,” *Proc. of HT2005 2005 ASME Summer Heat Transfer Conference*, July 17-22, 2005, San Francisco, California, USA.

Morgan, V.T., 1975, “The Overall Convective Heat Transfer from Smooth Circular Cylinders,” in T.F. Irvine and J.P. Hartnett, Eds., *Advances in Heat Transfer*, Vol. 11, Academic Press, NY. As Cited In: Incropera, F.P., and DeWitt, D.P., 2002, *Fundamentals of Heat and Mass Transfer*, 5th Ed., John Wiley & Sons, New York, p. 517.

Mudawar, I., and Anderson, T.M., 1993, “Optimization of Enhanced Surfaces for High Flux Chip Cooling by Pool Boiling,” *Journal of Electronic Packaging*, **115**, pp. 89-100.

Mudawar, I., and Valentine, W.S., 1989, “Determination of the Local Quench Curve for Spray-Cooled Metallic Surfaces,” *Journal of Heat Treating*, **7**, pp. 107-121.

Murshed, S.M.S., Leong, K.C., and Yang, C., 2006, “Thermal Conductivity of Nanoparticle Suspensions (Nanofluids),” *Proc. of the 2006 IEEE Conference on Emerging Technologies - Nanoelectronics*, January 10-13, 2006, pp. 155- 158.

Nakayama, W., Daikoku, T., Kuwahara, H., and Nakajima, T., 1980, “Dynamic Model of Enhanced Boiling Heat Transfer on Porous Surfaces,” *Journal of Heat Transfer*, **102**, pp. 445-450.

Nakayama, W., Daikoku, T., and Nakajima, T., 1982, “Effects of Pore Diameters and System Pressure on Saturated Pool Nucleate Boiling Heat Transfer from Porous Surfaces,” *Journal of Heat Transfer*, **104**, pp. 286-291.

Nakayama, W., Nakajima, T., and Hirasawa, S., 1984, “Heat Sink Studs Having Enhanced Boiling Surfaces For Cooling Microelectronic Components,” ASME Paper No. 84-WA/HT-89.

Nanophase Technologies Corporation, 2003, “NanoTek Aluminum Oxide Product Literature.”

Nasr, G.G., Yule, A.J., and Bendig, L., 2002, *Industrial Sprays and Atomization: Design, Analysis, and Applications*, Springer-Verlag, London, UK.

- Pais, M.R., Chow, L.C., and Mahefkey, E.T., 1992, "Surface Roughness and Its Effects on the Heat Transfer Mechanism in Spray Cooling," *Journal of Heat Transfer*, **114**, pp. 211-219.
- Pak, B.C., and Cho, Y.I., 1998, "Hydrodynamic and Heat Transfer Study of Dispersed Fluids with Submicron Metallic Oxide Particles," *Experimental Heat Transfer*, **11**(2), pp. 151-170.
- Pautsch, A. G., and Shedd, T. A., 2005, "Spray Impingement Cooling with Single- and Multiple-nozzle Arrays. Part I: Heat Transfer Data Using FC-72," *International Journal of Heat and Mass Transfer*, **48**, pp. 3167-3175.
- Pautsch, A.G., and Shedd, T.A., 2006, "Adiabatic and Diabatic Measurements of the Liquid Film Thickness during Spray Cooling with FC-72," *International Journal of Heat and Mass Transfer*, **49**, pp. 2610-2618.
- Potash, M., Jr. and Wayner, P. C., Jr., 1972, "Evaporation from a Two-Dimensional Extended Meniscus," *International Journal of Heat and Mass Transfer*, **15**, pp. 1851-1863.
- Putnam, S.A., Cahill, D.G., Braun, P.V., Ge, Z., and Shimmin, R.G., 2006, "Thermal Conductivity of Nanoparticle Suspensions," *Journal of Applied Physics*, **99**, paper no. 084308.
- Prasher, R., Song, D., Wang, J., and Phelan, P., 2006, "Measurements of Nanofluid Viscosity and Its Implications for Thermal Applications," *Applied Physics Letters*, **89**, paper no. 133108.
- Ramaswamy, C., Joshi, Y., Nakayama, W., and Johnson, W.B., 2003, "Effects of Varying Geometrical Parameters on Boiling from Microfabricated Enhanced Structures," *Journal of Heat Transfer*, **125**, pp. 103-109.
- Rini, D.P., Chen, R.-H., and Chow, L.C., 2002, "Bubble Behavior and Nucleate Boiling Heat Transfer in Saturated FC-72 Spray Cooling," *Journal of Heat Transfer*, **124**, pp. 63-72.
- Rybicki, J.R., and Mudawar, I., 2006, "Single-phase and Two-Phase Cooling Characteristics of Upward-facing and Downward-facing Sprays," *International Journal of Heat and Mass Transfer*, **49**, pp. 5-16.
- Sakamoto, H., Kim, J., Kiger, K., and Steinthorsson, E., 2006, "Multi-Nozzle Spray Cooling: Effects of Spray Interaction," *Proceedings of the Thirteenth International Heat Transfer Conference*, August 13-18, 2006, Sydney, Australia.

Sehmbey, M.S., Chow, L.C., Pais, M.R., and Mahefkey, T., 1994, "High Heat Flux Spray Cooling: A Review," in *Heat Transfer in High Heat Flux Systems*, HTD-Vol. 301, ASME Publishing, pp. 39-46.

Shedd, T.A., and Pautsch, A.G., 2005, "Spray Impingement Cooling with Single- and Multiple-Nozzle Arrays. Part II: Visualization and Empirical Models," *International Journal of Heat and Mass Transfer*, **48**, pp. 3176-3184.

Silk, E.A., Kim, J., and Kiger, K., 2004, "Investigation of Enhanced Surface Spray Cooling," *Proceedings of IMECE04 2004 ASME International Mechanical Engineering Congress and Exposition*, November 13-20, 2004, Anaheim, California, paper no. IMECE2004-61753.

Silk, E.A., Kim, J., and Kiger, K., 2005, "Spray Cooling Trajectory Angle Impact Upon Heat Flux Using a Straight Finned Enhanced Surface," *Proceedings of HT2005: ASME 2005 Heat Transfer Summer Conference*, July 17-22, San Francisco, ASME, New York, ASME Paper No. HT2005-72634.

Silk, E.A., Kim, J., and Kiger, K., 2006, "Spray Cooling of Enhanced Surfaces: Impact of Structured Surface Geometry and Spray Axis Inclination," *International Journal of Heat and Mass Transfer*, **49**, pp. 4910-4920.

Sodtke, C., and Stephan, P., 2005, "Spray Cooling Heat Transfer on Micro Structured Surfaces," *Proc. of 6th World Conference on Experimental Heat Transfer, Fluid Mechanics, and Thermodynamics*, April 17-21, Matsushima, Miyagi, Japan.

Stephan, K., and Abdelsalam, M., 1980, "Heat-Transfer Correlations for Natural Convection Boiling," *International Journal of Heat and Mass Transfer*, **23**, pp. 73-87.

Tachibana, F., Akiyama, M., and Kawamura, H., 1967, "Non-Hydrodynamic Aspects of Pool Boiling Burnout," *Journal of Nuclear Science and Technology*, **4**(3), pp. 121-130.

Takata, Y., Hidaka, S., Cao, J.M., Nakamura, T., Yamamoto, H., Masuda, M., and Ito, T., 2005, "Effect of Surface Wettability on Boiling and Evaporation," *Energy*, **30**, pp. 209-220.

Tilton, D.E., Tilton, C.L., Pais, M.R., and Morgan, M.J., 1992, "High-Flux Spray Cooling in a Simulated Multichip Module," in *Topics in Heat Transfer*, Vol. 2, HTD-Vol. 206-2, ASME Publishing.

Vassalo, P., Kumar, R., and D'Amico, S.D., 2004, "Pool boiling heat transfer experiments in silica-water nano-fluids," *International Journal of Heat and Mass Transfer*, **47**, pp. 407-411.

- Wang, Y., Fisher, T.S., Davidson, J.L., and Jiang, L., 2002, "Thermal Conductivity of Nanoparticle Suspensions," *Proc. of the 8th AIAA/ASME Joint Thermophysics and Heat Transfer Conference*, June 24-26, 2002, St. Louis, Missouri, paper no. AIAA 2002-3345.
- Wang, X., Xu, X., and Choi, S.U.S., 1999, "Thermal Conductivity of Nanoparticle-Fluid Mixture," *Journal of Thermophysics and Heat Transfer*, **13**(4), pp. 474-480.
- Wen, D., and Ding, Y., 2005, "Experimental Investigation into the Pool Boiling Heat Transfer of Aqueous Based γ -Alumina Nanofluids," *Journal of Nanoparticle Research*, **7**, pp. 265-274.
- Xue, H.S., Fan, J.R., Hu, Y.C., Hong, R.H., and Cen, K.F., 2006, "The Interface Effect of Carbon Nanotube Suspension on the Thermal Performance of a Two-Phase Closed Thermosyphon," *Journal of Applied Physics*, **100**, paper no. 104909.
- Yang, J., Chow, L.C., and Pais, M.R., 1996, "Nucleate Boiling Heat Transfer in Spray Cooling," *Journal of Heat Transfer*, **118**, pp. 668-671.
- Yang, Y., Zhang, Z.G., Grulke, E.A., Anderson, W.B., and Wu, G., 2005, "Heat Transfer Properties of Nanoparticle-in-Fluid Dispersions (Nanofluids) in Laminar Flow," *International Journal of Heat and Mass Transfer*, **48**, pp. 1107-1116.
- Yang, Y.M., and Maa, J.R., 1984, "Boiling of Suspension of Solid Particles in Water," *International Journal of Heat and Mass Transfer*, **27**(1), pp. 145-147.
- Yaws, C.L., 1999, *Chemical Properties Handbook*, McGraw-Hill Handbooks. As Cited In: Klein, S.A., 2006, *Engineering Equation Solver*. Computer Software, F-Chart Software, Version 7.693.
- You, S.M., 1990, "Pool Boiling Heat Transfer with Highly-Wetting Dielectric Fluids," Ph.D. thesis, University of Minnesota. As Cited In: Wu, P.S., and Simon, T.W., 1994, "Effects of Dissolved Gases on Subcooled Flow Boiling from Small Heated Regions with and without Streamwise Concave Curvature," *Proceedings of the 1994 Intersociety Conference on Thermal Phenomena*, Washington, DC, May 4-7, 1994.
- You, S.M., Bar-Cohen, A., and Simon, T.W., 1990, "Boiling Incipience and Nucleate Boiling Heat Transfer of Highly Wetting Dielectric Fluids from Electronic Materials," *IEEE Transactions on Components, Hybrids, and Manufacturing Technology*, **13**(4), pp. 1032-1039.
- You, S.M., Kim, J.H., and Kim, K.H., 2003, "Effect of Nanoparticles on Critical Heat Flux of Water in Pool Boiling Heat Transfer," *Applied Physics Letters*, **83**(16), pp. 3374-3376.